

INVESTIGATING HIGH FIELD GRAVITY USING ASTROPHYSICAL TECHNIQUES

Elliott D. Bloom
Stanford Linear Accelerator Center
Stanford University, Stanford, CA 94309

*Invited talk given at the 22nd Annual SLAC Summer Institute on Particle Physics: Particle Physics, Astrophysics and Cosmology,
8/6/1994-8/19/1994, Stanford, CA*

Work supported by US Department of Energy contract DE-AC02-76SF00515

Table of Contents

Preface

1. Introduction

2. The Physics of Compact Stellar Objects

a. Schwarzschild Geometry

b. The Equation of State of Compact Stellar Objects

c. The End State of Stars

(i) White Dwarfs

(ii) Neutron Stars

(iii) Strange Stars, Q-Stars, and Black Holes

(iv) Summary

3. Laboratories for Particle Astrophysics: X-Ray Stellar Binary Systems and Active Galactic Nuclei (AGN)

a. Description of X-Ray Binary Systems

b. Description of Active Galactic Nuclei (AGN)

c. X-Ray Binary System Orbital Parameters

d. Using Orbital Parameters to Determine Compact Object Masses

(i) Some Leading Stellar Black Hole Candidates

(ii) The Black Hole Candidate in the AGN of M87

e. Using Fast X-Ray Timing to Measure the Compact Size of Compact Stellar Objects

(i) X-Ray Timing Measurements for Cyg X-1

4. X-Ray Astrophysics

a. X-Ray Discriminants Black Holes vs. Neutron Stars

b. Future X-Ray Missions

(i) The Unconventional Stellar Aspect Experiment (USA)

(ii) The X-Ray Timing Explorer (XTE)

5. Gamma-Ray Astrophysics
 - a. Gamma-Ray Bursters
 - b. Results from High-Energy Gamma-Ray Experiments
 - (i) Space Based (mainly EGRET)
 - (ii) Ground Based
 - c. Future High-Energy Gamma-Ray Missions
6. Conclusions
7. Acknowledgments
8. Appendices
 - A. Introduction to Wavelet Methods
 - B. A List of Current Black Hole Candidates
9. References

Preface

The purpose of these lectures is to introduce particle physicists to astrophysical techniques. These techniques can help us understand certain phenomena important to particle physics that are currently impossible to address using standard particle physics experimental techniques. As the subject matter is vast, compromises are necessary in order to convey the central ideas to the reader. Many general references are included for those who want to learn more. The paragraphs below elaborate on the structure of these lectures. I hope this discussion will clarify my motivation and make the lectures easier to follow.

The lectures begin with a brief review of more theoretical ideas. First, elements of general relativity are reviewed, concentrating on those aspects that are needed to understand compact stellar objects (white dwarf stars, neutron stars, and black holes). I then review the equations of state of these objects, concentrating on the simplest standard models from astrophysics. After these mathematical preliminaries, Sec. 2(c) discusses *The End State of Stars*. Most of this section also uses the simplest standard models. However, as these lectures are for particle physicists, I also discuss some of the more recent approaches to the equation of state of very dense compact objects. These particle-physics-motivated equations of state can dramatically change how we view the formation of black holes.

Section 3 focuses on the properties of the objects that we want to characterize and measure. X-ray binary systems and Active Galactic Nuclei (AGN) are stressed because the lectures center on understanding very dense stellar objects, black hole candidates (BHCs), and their accompanying high gravitational fields. The use of x-ray timing and gamma-ray experiments is also introduced in this section.

Sections 4 and 5 review information from x-ray and gamma-ray experiments. These sections also discuss the current state of the art in x-ray and gamma-ray satellite experiments and plans for future experiments.

1. Introduction

Along with QCD and the electroweak forces, gravity is one of the fundamental forces of nature. However, even though gravity was the earliest force to be described analytically and has more recently been embodied in General Relativity (GR), a complete understanding of gravity has yet to be found. The goal of a self-consistent quantum field theory of gravity still escapes us after more than 60 years of effort. In addition, with our understanding of particle physics apparently extended to the TeV mass range and our theoretical estimates of conditions in the early universe reaching to the inflationary epoch at 10^{-30} sec and earlier, questions of the role of gravity in the unification of the forces loom large.

My view is that physics is ultimately an experimental science, and so we need data, lots of data, to make progress in our theoretical understanding. I suggest that the lack of progress in understanding the deeper aspects of gravity comes from a dearth of even remotely related data. How one might approach an experimental examination of strong field relativistic gravity and related topics is one of the main subjects of these lectures. It is not easy to decide what to do, and once decided, not easy to accomplish. The relevant experimental approaches are all very difficult; however, we have to start somewhere.

2. The Physics of Compact Stellar Objects

One place we believe that the full power of GR is needed to describe the physics, and hence can be tested, is in the immediate neighborhood of compact stellar objects. Such objects include white dwarfs, neutron stars, and black holes. This section explores the character of these objects and briefly develops current models that describe them.

2a. Schwarzschild Geometry

The physics of compact stellar objects requires two major components—gravity and an equation of state. Gravity, which we briefly describe in this section, results from the mass distribution of the compact object. This mass distribution generates a space-time geometry predicted by GR, which in turn produces the gravitational field that controls the structure of the compact object.¹ Indeed, in the case of a compact object of sufficient mass, this space-time geometry leads to a new type of object, a black hole, that is stranger than fiction. Black holes are not just a new type of stellar object. Their properties, as predicted by GR, challenge our basic understanding of quantum mechanics, particle physics, and space-time itself.²

In GR, the only spherically symmetric gravitational field solution in vacuum is static. This space-time geometry is named after Schwarzschild, who first derived it from the GR field equations. The Schwarzschild space-time geometry is represented by the metric

$$ds^2 = -\left(1 - \frac{2M}{r}\right)dt^2 + \frac{dr^2}{1 - \frac{2M}{r}} + r^2(d\theta^2 + \sin^2\theta d\phi^2) \quad (1)$$

with the choice of units such that c (speed of light) = G (gravitational constant) = 1. In the weak field limit, Schwarzschild space-time geometry becomes Newtonian gravity from a central mass, M , in flat space-time.

In the case of compact stellar objects that are not black holes, $M \rightarrow$ mass within radius r , or $m(r)$, and the factor $[1 - 2m(r)/r]^{-1}$ does not become singular at $r = 2M$, because $m(r)$ decreases sufficiently fast with decreasing r ; that is, the radius $r = 2M$ lies inside the matter distribution of the compact object. (M in this case is the total mass of the star.) A black hole solution results when this is not the case. For black holes, $r = 2M$ lies outside the matter distribution of the compact object. In general, $R^{sch} \equiv 2GM/c^2 = 2M \cong 3(M/M_\odot)$ [km], where M_\odot is the sun's mass and defines the "Schwarzschild horizon" or "Schwarzschild radius," or in current parlance, the "event horizon." In the case of black holes, $r = 2M$ seems a badly behaved region of the Schwarzschild geometry, as the metric appears to diverge to infinity. However, the space-time geometry is not singular there.

As described in Chapter 31 of Misner, Thorne, and Wheeler (MTW)¹, to determine whether or not the space-time geometry is singular at the horizon radius of a black hole, send an astronaut in from far away to chart it (as happened recently on the TV program "Star Trek Voyager"). For simplicity, let the astronaut fall freely and radially toward the horizon. The radial geodesic of the Schwarzschild metric in the astronaut's rest frame gives, in terms of his/her proper time, τ ,

$$\frac{\tau}{2M} = -\frac{2}{3}\left(\frac{r}{2M}\right)^{\frac{3}{2}} + const1. \quad (2)$$

While for an observer far away (Schwarzschild-coordinate time t) the time it takes for the astronaut to fall is

$$\frac{t}{2M} = -\frac{2}{3}\left(\frac{r}{2M}\right)^{\frac{3}{2}} - 2\left(\frac{r}{2M}\right)^{\frac{1}{2}} + \ln \left| \frac{\left(\frac{r}{2M}\right)^{\frac{1}{2}} + 1}{\left(\frac{r}{2M}\right)^{\frac{1}{2}} - 1} \right| + \text{const}2. \quad (3)$$

Figure 1 shows the trajectories derived from Eqs. (2) and (3) (for a particular initial condition). Of all the features of the astronaut’s trajectory, one stands out most clearly and disturbingly: to reach the horizon, $r = 2M$ (the dotted line in the figure) requires a finite lapse of proper time, but an infinite lapse of coordinate time. The traveler passes through the horizon to be inexorably crushed by the black hole’s “true” singularity at $r = 0$ in a bit over $\tau = 16/M$, while to the far away observer, the astronaut just redshifts from sight,³ approaching the horizon as $t \rightarrow \infty$.

Of course, proper time is the relevant quantity for the explorer’s heartbeat and health. No coordinate system has the power to prevent the inevitable in fall to $r = 0$. Only the coordinate-independent geometry of space-time could possibly do that, and Eq. (2) shows that it does not!

The Schwarzschild metric is well-suited to describe a spherically symmetric star with zero angular momentum. The metric is used in the calculations of the properties of compact stellar objects that approximate these conditions. Figure 2, from Chapter 23 of MTW, schematically displays the geometry within (dark gray) and around (white) a spherically symmetric star of radius $R = 2.66M$. The star is in hydrostatic equilibrium and has zero angular momentum. The two-dimensional geometry

$$ds^2 = [1 - 2m(r)/r]^{-1} dr^2 + r^2 d\phi^2 \quad (4)$$

of an equatorial slice through the star at fixed time ($\theta = \pi/2$, $t = t_0$) is represented as embedded in Euclidean three-space in such a way that distances between any two nearby points in the surface are shown correctly. Distances measured out of the curved surface have no physical meaning. The embedding three-space itself also has no physical meaning and is just used as a tool to show the curved two-geometry induced by the star’s mass.

Because of the relatively simple form of Eq. (1), the coordinates have a direct physical interpretation. For the Schwarzschild geometry displayed in the figure, at any radius r there is a two-dimensional spherical surface centered about the point $r = 0$, and θ , ϕ are conventional polar

coordinates on the two-sphere. The quantity r is defined by setting the proper circumference of the two-sphere to $2\pi r$. This circumference in curved two-geometry corresponds to a sphere of proper area $4\pi r^2$ in the three-geometry of real Euclidean space (not the embedding three-space of the figure). Note that due to the metric of curved space, the proper distance R , between $r = 0$ and the point labeled by r on a radial line in this space, is larger than r and $4\pi R^2 > 4\pi r^2$. This correspondence, $r \rightarrow 4\pi r^2$, allows one to visualize the entire three-geometry in and around the star at any time t .

2b. The Equation of State of Compact Stellar Objects

Besides the gravitational field, the physics of the compact stellar object must be put into the (highly nonlinear) equations that predict the space-time structure of these objects and their surroundings. Compact stellar objects evolve from stellar objects. A stellar object refers to a star at any time during its evolution. In its nuclear burning phase, the stellar object is usually a main sequence star, such as our sun. Depending on its mass and history, at the end of its evolution, the stellar object can collapse to a compact stellar object. Stars “die” when most of their nuclear fuel has been consumed.⁴ White dwarfs, neutron stars, and black holes are “born” when normal stars “die.”

The equation of state of a stellar object gives the relationship between its pressure and density,

$$P = P(\rho). \tag{5}$$

This equation incorporates the underlying microphysics as local thermodynamic relationships of an individual matter element. However, the microphysics is the determining factor. Thus, our understanding of the basic physics at the extreme conditions existing in compact objects is central to the success of the theory. In the case of black hole formation, the correct microphysics could possibly require input from particle physics beyond the Standard Model, while current theories typically include only idealistic approximations from nuclear physics and lower energy scales.

In kinetic theory, the number density in phase space for each species of particle, $\left(\frac{dn}{d^3x d^3p}\right)$, provides a complete description of the system.⁵ The main thermodynamic variables

we will be considering are density and pressure. The density is formally given as the total energy per unit volume, where the total energy of a particle species, j , with three-momentum magnitude p_j and mass m_j , is (with $c = 1$)

$$E_j = \sqrt{p_j^2 + m_j^2}. \quad (6)$$

The energy density is then

$$\varepsilon = \int E \left(\frac{dn}{d^3x d^3p} \right) d^3p. \quad (7)$$

The pressure, P , is the “flow of momentum density” and is given for an isotropic medium by

$$P = n \langle (\hat{p} \cdot \hat{n})(\hat{v} \cdot \hat{n}) \rangle = \frac{1}{3} \int p v \left(\frac{dn}{d^3x d^3p} \right) d^3p = \frac{1}{3} \int \frac{p^2}{E} \left(\frac{dn}{d^3x d^3p} \right) d^3p, \quad (8)$$

where

$$n = \int \left(\frac{dn}{d^3x d^3p} \right) d^3p \quad (9)$$

is the number density of each species of particles, \hat{p} is the three momentum, \hat{v} is the three velocity, and \hat{n} is a unit vector defining a direction. The factor of 1/3 comes from assumed isotropy. Note that for massless particles, $P = \varepsilon/3$.

Using the number density, we can define an equivalent dimensionless distribution function in phase space, F , that gives the Lorentz invariant average occupation number of a cell in phase space. As $d^3x d^3p$ is a scalar under a Lorentz transformation, F is also.

$$\left(\frac{dn}{d^3x d^3p} \right) = \frac{g}{h^3} F(\vec{x}, \vec{p}, t), \quad (10)$$

where h is Planck's constant, h^3 is the volume of a cell in phase space, and g is the statistical weight for a particle species. Here, $g = 2S+1$ for massive particles with spin S . For photons, $g = 2$, and for neutrinos, $g = 1$ (as there are only left-handed neutrinos).

For an ideal gas in equilibrium, F has the simple form

$$F(E) = \frac{1}{e^{[(E-\mu)/kT]_{\pm 1}}} \quad (11)$$

where the “+” sign corresponds to fermions (Fermi-Dirac statistics), and the “-” sign to bosons (Bose-Einstein statistics). In Eq. (11), T is the temperature, k is Boltzmann's constant, and μ is the chemical potential for the species.

For sufficiently low particle densities and high T , $F(E)$ becomes the Maxwell-Boltzmann distribution

$$F(E) \approx e^{\left[\frac{\mu-E}{kT}\right]} \ll 1. \quad (12)$$

For completely degenerate fermions ($T \rightarrow 0$, i.e., $\mu/kT \rightarrow \infty$), μ is identified with the *Fermi Energy*, E_F , and,

$$F(E) = \begin{cases} 1, & E \leq E_F \\ 0, & E > E_F \end{cases}. \quad (13)$$

As an example, we derive the equation of state of a completely degenerate, single species, ideal (noninteracting) Fermi gas.⁶ This very idealized equation of state actually has approximate validity in describing isolated white dwarf and neutron stars. These compact stellar objects ultimately cool to zero temperature. At $T \cong 0$, it is the degeneracy pressure of electrons in the case of white dwarfs, and neutrons in the case of neutron stars, that support these stars against gravitational collapse. More realistic, and consequently more complex, equations of state describing white dwarfs and neutron stars can be found in the literature.⁷

Let us start with the electron gas case that applies to white dwarfs. The gas can be treated as ideal if all electromagnetic interactions are neglected. We concentrate on the degeneracy

force, which is the dominant force between the electrons at very high density. We define the *Fermi momentum*, p_F , by

$$E_F = \sqrt{p_F^2 + m_e^2}. \quad (14)$$

Equations (9), (10), and (13) then give

$$n_e = \frac{2}{h^3} \int_0^{p_F} 4\pi p^2 dp = \frac{8\pi}{3h^3} p_F^3. \quad (15)$$

We define a dimensionless Fermi momentum

$$x_F = p_F/m_e. \quad (16)$$

Then Eq. (15) becomes

$$n_e = \frac{x_F^3}{3\pi^2 D_e^3}, \quad (17)$$

where

$$D_e = h/m_e c = 3.862 \times 10^{-13} \text{ m} \quad (18)$$

is the electron Compton wavelength in SI units.

The degeneracy pressure from the electron gas is given by Eqs. (8), (10), (13), and (16),

$$P_e = \frac{2}{3h^3} \int_0^{p_F} \frac{p^2}{\sqrt{p^2 + m_e^2}} 4\pi p^2 dp = \frac{m_e}{3\pi^2 D_e^3} \int_0^{x_F} \frac{x^4 dx}{\sqrt{1+x^2}} = \frac{m_e}{D_e^3} \varphi(x_F), \quad (19)$$

where

$$\varphi(x_F) = \frac{1}{8\pi^2} \left\{ x_F \sqrt{1+x_F^2} \left(\frac{2x_F^2}{3} - 1 \right) + \operatorname{arcsinh}(x_F) \right\}, \quad (20)$$

and $m_e c^2 / \mathcal{A}_e^3 = 1.422 \times 10^{24}$ Pa (in SI units, 1 Pa = 1 Pascal = 1 Newton/m²).

Similarly, the energy density of the electron gas is given by Eqs. (7), (10), (13), and (16),

$$\varepsilon_e = \frac{2}{h^3} \int_0^{p_F} \sqrt{p^2 + m_e^2} 4\pi p^2 dp = \frac{m_e}{\mathcal{D}^3} \chi(x_F), \quad (21)$$

where

$$\chi(x_F) = \frac{1}{8\pi^2} \left\{ x_F \sqrt{1+x_F^2} (2x_F^2 + 1) - \operatorname{arcsinh}(x_F) \right\}, \quad (22)$$

and in this case, we take $m_e c / \mathcal{A}_e^3 = 1.422 \times 10^{24}$ J/m³.

When considering the equation of state of white dwarf stars, we see that the degenerate electron gas contributes most of the pressure; however, the density is dominated by the rest-mass of the ions. This baryon density, ρ_B , is given in terms of the weighted sum over masses of the ion species i , m_i ,

$$\rho_B = \sum_i n_i m_i, \quad (23)$$

where n_i is the number of ion types i per m³. The mean baryon rest mass, m_B , is commonly used in the literature, where

$$m_B \equiv \frac{\sum_i n_i m_i}{\sum_i n_i A_i} = \frac{\rho_B}{n_B}, \quad (24)$$

and A_i is the baryon number of the i^{th} ionic species, while n_B is the number of baryons per m³. All of the quantities discussed above are usually considered in the center-of-mass frame of the star.

In order to express the baryon density in terms of x_F , we define a mean number of electrons per baryon in the plasma, Y_e ,

$$Y_e \equiv \frac{n_e}{n_B} = \frac{Z}{A}. \quad (25)$$

From Eqs. (18), (24), and (25), we find

$$\rho_B = \frac{m_B x_F^3}{Y_e 3\pi^2 D_e^3}. \quad (26)$$

For example, in the case of completely ionized pure $^{26}\text{Fe}_{56}$, which is nuclear matter at minimum energy content, $Y_e = Z/A = 0.464$, and taking $m_B = 1$ amu (atomic mass unit) = 1.661×10^{-27} kg, we find

$$\rho_B = 2.099 \times 10^9 x_F^3 \text{ kg/m}^3. \quad (27)$$

The full density includes the energy density ε from Eq. (21) as well as from Eq. (26),

$$\rho(x_F) = \rho_B(x_F) + \varepsilon(x_F). \quad (28)$$

However, $\varepsilon / \rho_B \ll 1$ is the usual case.

Equations (28) and (19) plus (20) give the *ideal degenerate* equation of state, $P = P(\rho)$ parametrically in terms of x_F . In two important limiting cases, this equation can be approximated by the *polytropic* form

$$P = K \rho_B^\Gamma, \quad (29)$$

where K and Γ are constants.

The first limit is the nonrelativistic case, $x_F \ll 1$. For nonrelativistic electrons,

$$\begin{aligned}\varphi(x_F) &\xrightarrow{x \ll 1} \frac{1}{15\pi^2} \left(x_F^5 - \frac{5}{14} x_F^7 + \frac{5}{24} x_F^9 + O(x_F^{11}) \right), \\ \chi(x_F) &\xrightarrow{x \ll 1} \frac{1}{3\pi^2} \left(x_F^3 + \frac{3}{10} x_F^5 - \frac{3}{56} x_F^7 + O(x_F^9) \right).\end{aligned}\tag{30}$$

In the **nonrelativistic case**, using the limiting forms of Eqs. (19), (21), and (28), the equation of state becomes

$$\begin{aligned}P = P_e &\cong \frac{m_e}{15\pi^2 D_e^3} x_F^5 = K \rho^\Gamma = K \left[\left(\frac{m_B}{3\pi^2 D_e^3 Y_e} + \frac{m_e}{3\pi^2 D_e^3} \right) x_F^3 \right]^\Gamma \Rightarrow \\ \Gamma &= \frac{5}{3}, \quad K = \frac{\left(\frac{3\pi^2}{m_e} \right)^{\frac{2}{3}} \cdot D_e^2 \cdot c^2}{5 \cdot \left(1 + \frac{m_B}{m_e Y_e} \right)^{\frac{5}{3}}} = 1.004 \times 10^7 Y_e^{\frac{5}{3}} \text{ [SI units]}.\end{aligned}\tag{31}$$

$P \propto \rho^{5/3}$ results in the approximation for the nonrelativistic case.

For example, in the case of completely ionized pure $^{26}\text{Fe}_{56}$ and $x_F = 0.2$, we find $K = 2.797 \times 10^6$, $P = 3.074 \times 10^{18}$ Pa, and $\rho = 1.68 \times 10^7$ kg/m³. Note that at the center of the sun, $P \cong 10^{16}$ Pa and $\rho = 1.5 \times 10^5$ kg/m³.

The second limit is the **very relativistic case**, $x_F \gg 1$, (and $x_F < 10^3$). For very relativistic electrons,

$$\begin{aligned}\varphi(x_F) &\xrightarrow{x \gg 1} \frac{1}{12\pi^2} \left(x_F^4 - x_F^2 + \frac{3}{2} \ln 2x_F + O(x_F^{-2}) \right), \\ \chi(x_F) &\xrightarrow{x \gg 1} \frac{1}{4\pi^2} \left(x_F^4 + x_F^2 - \frac{1}{2} \ln 2x_F + O(x_F^{-2}) \right).\end{aligned}\tag{32}$$

In the very relativistic case, the energy density of the electron gas dominates baryon density and the equation of state becomes, using the limiting forms of Eqs. (19), (21), and (28),

$$\begin{aligned}
P = P_e &\cong \frac{m_e}{12\pi^2 D_e^3} x_F^4 = K\rho^\Gamma = K \left[\frac{m_B}{3\pi^2 D_e^3 Y_e} x_F^3 + \frac{m_e}{4\pi^2 D_e^3} x_F^4 \right]^\Gamma \\
&\xrightarrow{x_F \gg 1, \ll 1000} K \left[\frac{m_B}{3\pi^2 D_e^3 Y_e} x_F^3 \right]^\Gamma \Rightarrow \\
\Gamma &= \frac{4}{3}, \quad K = \frac{\left(\frac{3\pi^2}{m_e} \right)^{\frac{1}{3}} \cdot D_e \cdot c^2}{4 \cdot \left(\frac{m_B}{m_e Y_e} \right)^{\frac{4}{3}}} = 1243 \times 10^{10} Y_e^{\frac{4}{3}} \text{ [Slunits]}.
\end{aligned} \tag{33}$$

$P \propto \rho^{4/3}$ results in the approximation for the very relativistic case. For example, in the case of completely ionized pure $^{26}\text{Fe}_{56}$ and $x_F = 10$, we find $K = 4.447 \times 10^9$, $P = 1.200 \times 10^{26}$ Pa, and $\rho = 2.105 \times 10^{12}$ kg/m³.

For values of x_F larger than ≈ 10 , white dwarf stars are unstable. The next regime of stability results in neutron stars. (This will be discussed in more detail in the following sections.) Equations (31) and (33) can also be used in the neutron star regime via a simple scaling in particle mass from m_e to m_n ; the statistical weight $g = 2$ is the same, and $x_F = p_F / m_n$. For pure neutrons (in general, neutron stars have an admixture of ions, electrons, and neutron “gas”), and $x_F \ll 1$, Eq. (31) scales to Eq. (34).

$$\begin{aligned}
P = P_n &\cong \frac{m_n}{15\pi^2 D_n^3} x_F^5 = K\rho^\Gamma = K \left[\left(\frac{m_n}{3\pi^2 D_n^3} \right) x_F^3 \right]^\Gamma \Rightarrow \\
\Gamma &= \frac{5}{3}, \quad K = \frac{\left(\frac{3\pi^2}{m_n} \right)^{\frac{2}{3}} \cdot D_n^2 \cdot c^2}{5} = 53810 \times 10^8 \text{ [Slunits]}.
\end{aligned} \tag{34}$$

For example, for pure neutrons and $x_F = 0.2$, we find $P = 3.513 \times 10^{31}$ Pa, and $\rho = 4.886 \times 10^{16}$ kg/m³.

For $x_F \gg 1$, Eq. (33) scales to Eq. (35), the **extreme relativistic** free fermion equation of state.

$$P = P_n \cong \frac{m_n}{12\pi^2 D_n^3} x_F^4 = K\rho^\Gamma = K\left[\left(\frac{m_n}{4\pi^2 D_n^3} x_F^4\right)\right]^\Gamma \Rightarrow$$

$$\Gamma = 1, \quad K = \frac{c^2}{3} = 8.987 \times 10^6 \text{ [SI unit]}.$$
(35)

Note that $P = \rho c^2/3$ is a relatively “soft” equation of state; that is, the power of ρ is relatively low compared to other “stiff” equations of state we have considered, e.g., Eq. (34).

2c. The End State of Stars⁸

The structure of normal, main sequence stars is supported by the thermal pressure of hot gas balancing the inward pull of gravity due to the matter of the star. The temperature needed to generate this pressure comes from the nuclear burning of H to He for most of the life of the star. As the star ages, it eventually evolves off the main sequence⁸ up the “Giant branch.” In the final phases of the Giant branch evolution, the outer layers of the star are ejected, and the nuclear burning uses fuel other than H. The more massive the star, the more rapidly it evolves, and the further it can move up the atomic table toward iron in its nuclear burning. (Iron is the most stable nucleus.) At some point, the nuclear fuel is exhausted, and the star “dies.” Dead stars are currently thought to exist in one of three compact states, depending on the mass of the progenitor star and its history. In order of increasing mass, these three states are white dwarf, neutron star, or black hole; all three have two characteristics that easily differentiate them from normal stars.

First, since they do not burn nuclear fuel, they cannot support themselves against gravitational collapse by generating thermal pressure. White dwarfs and neutron stars support themselves against gravity by the degeneracy pressure of electrons and neutrons, respectively. The equations of state discussed in Sec. 2b above demonstrate the physics of degeneracy pressure. Black holes, however, are completely collapsed stars. They result when the pressure generated in the compact object, by any means, is overcome by the inward pull of gravity. If and how black holes form is still somewhat controversial.

Second, white dwarfs, neutrons stars, and stellar mass black holes are very compact objects compared to normal stars. With typical masses greater than $1 M_{\odot}$, and radii of $10^{-2} R_{\odot}$ for white dwarfs, $10^{-5} R_{\odot}$ for neutron stars, and $3 (M/M_{\odot})$ [km] for black holes, these objects have much smaller radii, and consequently much stronger “surface” gravitational fields than normal stars. (Here, we are considering stellar mass objects. The statement is not true for the galactic black holes, with masses in the range 10^6 – $10^{10} M_{\odot}$, thought to be at the center of some galaxies.)

With the exception of primordial black holes formed in the very early universe, with masses less than 10^{12} kg, which would have evaporated (via Hawking’s radiation) by the present epoch, all three types of compact objects are essentially static over the lifetime of the universe. They are the final, and typically stable, stages of stellar evolution.

(i) White Dwarf Stars

White dwarf stars have been directly observed via their radiation in visible through UV light. Even though they no longer burn nuclear fuel, they can be seen in these wavelengths as they are very slowly cooling as they radiate away their residual heat (10^9 – 10^{10} years). Those white dwarf stars observed in well-characterized binary systems have had mass determinations. For example, Sirius B, perhaps the best known white dwarf star, is the binary companion to Sirius. The binary nature of the Sirius system was first reported by F. Bessel in 1844. Sirius B was unseen with the telescopes of that time, and its existence was based on the observations of the perturbed orbit of Sirius. Sirius B was first seen in visible light in 1863. Modern determinations of its mass from binary system orbit parameters give a mass of $1.003 M_{\odot}$. Recent satellite observations in the ultraviolet, where white dwarfs emit most of their light, have determined the surface temperature of Sirius B to be about 30,000 K. Using these spectral measurements, the equation for the luminosity from blackbody emission, $L = 4\pi R^2 \sigma T_{eff}^4$, and the accurately known distance to the star, the radius is determined to be 5.88×10^3 km ($= 0.0845 R_{\odot}$). Given its large density, $\rho = 2.34 \times 10^9$ kg/m³, and consequent surface gravity, Sirius B has been used to check the gravitational redshift predicted from GR, $\frac{\Delta\lambda}{\lambda} \cong \frac{GM}{Rc^2}$. The observed gravitational redshift is usually quoted as an equivalent Doppler shift $\Delta\lambda/\lambda = v/c$ or $v = 0.6362 (M/M_{\odot})/(R/R_{\odot})$ km/s. This predicts 91 ± 8 km/s for Sirius B, as compared to the observed value of 89 ± 16 km (Ref. 9).

White dwarf stars can be modeled using classical approximations to hydrostatic equilibrium and Newtonian gravity. This is not the case for neutron stars, which will be discussed separately.

Consider a spherically symmetric distribution of matter that represents the white dwarf star. The mass, $m(r)$, interior to radius r of the star is

$$m(r) = \int_0^r \rho(r) 4\pi r^2 dr \Rightarrow \frac{dm(r)}{dr} = 4\pi r^2 \rho(r). \quad (36)$$

In Eq. (36), we assume that the bulk of the matter in the star is nonrelativistic ions. A white dwarf star is approximately in a steady state; hence, the gravitational force balances the pressure force at every point. This results in the nonrelativistic hydrostatic equilibrium equation

$$\frac{dP(r)}{dr} = -\frac{Gm(r)\rho(r)}{r^2}. \quad (37)$$

After some algebra, Eqs. (36) and (37) can be combined to yield

$$\frac{1}{r^2} \frac{d}{dr} \left(\frac{r^2}{\rho(r)} \cdot \frac{dP(r)}{dr} \right) = -4\pi G \rho(r). \quad (38)$$

This equation takes a simple form in the case of a polytropic equation of state, Eq. (29). Writing the polytropic exponent as $\Gamma \equiv 1 + \frac{1}{n}$, where n is called the *polytropic index*, Eq. (38) can be reduced to dimensionless form with the substitutions

$$\rho = \rho_c \theta^n, \quad r = a\xi, \quad \text{with} \quad a = \sqrt{\frac{(n+1)K\rho_c^{(1/n-1)}}{4\pi G}}, \quad (39)$$

where $\rho_c = \rho(r=0)$ is the central density of the white dwarf star. (K is the *polytropic constant*.) Some straightforward algebraic manipulation results in the Lane-Emden equation,

$$\frac{1}{\xi^2} \frac{d}{d\xi} \left(\xi^2 \frac{d\theta}{d\xi} \right) = -\theta^n. \quad (40)$$

The boundary conditions for a polytropic star are formulated at $\xi = r = 0$,

$$\theta(0) = \frac{\rho(0)}{\rho_c} = 1, \quad \left. \frac{d\theta}{d\xi} \right|_{\xi=0} = 0 = \left. \frac{d\rho}{dr} \right|_{r=0}. \quad (41)$$

Since, $m(r) \cong \rho_c (4\pi r^3 / 3)$, near $r = 0$, Eq. (37) gives $\frac{dP}{dr} \cong \frac{4\pi G}{3} \rho_c r \xrightarrow{r \rightarrow 0} 0$. Then, from the polytropic equation of state, Eq. (28), we derive the latter boundary condition of Eq. (41).

Equation (40) can be solved by integrating numerically from $\xi = 0$ with the boundary conditions of Eq. (41). The solutions, $\theta(\xi)$, decrease monotonically and have a zero for $n < 5$ ($\Gamma > 6/5$) at a finite value of $\xi \equiv \xi_R$. (Note that the extreme relativistic free fermion equation of state, Eq. (35), has $\Gamma = 1$ and does not have solutions by this method.) Using Eq. (39), we find the radius of the star to be

$$R = a \xi_R, \quad (42)$$

and with the help of Eq. (40), the star's mass is

$$M = \int_0^R 4\pi r^2 \rho(r) dr = 4\pi a^3 \rho_c \int_0^{\xi_R} \xi^2 \theta^n d\xi = -4\pi a^3 \rho_c \xi_R^2 \cdot \left. \frac{d\theta}{d\xi} \right|_{\xi_R}. \quad (43)$$

ρ_c can be eliminated by solving Eqs. (42) and (43) in terms of M and R . This gives the mass-radius relation for polytropes with $\Gamma > 6/5$,

$$M = 4\pi R^{\left(\frac{3-n}{1-n}\right)} \left[\frac{(n+1)K}{4\pi G} \right]^{\left(\frac{n}{n-1}\right)} \xi_R^{\left(\frac{3-n}{1-n}\right)} \xi_R^2 \left[-\frac{d\theta}{d\xi} \right]_{\xi=R}. \quad (44)$$

The two solutions of interest for white dwarf stars are¹⁰ the nonrelativistic and very relativistic cases:

$$\begin{aligned} \Gamma = \frac{5}{3}, \Leftrightarrow n = \frac{3}{2}, \text{ yielding } \xi_R = 365375, \quad -\xi_R^2 \left[\frac{d\theta}{d\xi} \right]_{\xi=\xi_R} &= 27140\text{f} \\ \Gamma = \frac{4}{3}, \Leftrightarrow n = 3, \text{ yielding } \xi_R = 689685, \quad -\xi_R^2 \left[\frac{d\theta}{d\xi} \right]_{\xi=\xi_R} &= 20182\text{f} \end{aligned} \quad (45)$$

For the high density limit for white dwarf stars, the $\Gamma = 4/3$ solution is a reasonable approximation. Using the above numbers in Eq. (44) for the $\Gamma = 4/3$ case, with K given by Eq. (33), we find

$$M = 4\pi \left[\frac{1.243 \times 10^{10} \cdot Y_e^{\frac{4}{3}}}{\pi G} \right]^{\frac{3}{2}} (2.01824) = 1.455(2 \cdot Y_e)^2 M_\odot. \quad (46)$$

The relation $R = a\xi_R$ gives

$$R = 689685 \cdot \sqrt{\frac{(1.243 \times 10^{10} \cdot Y_e^{\frac{4}{3}}) \cdot \rho_c^{\frac{2}{3}}}{\pi G}} = 2.231 \times 10^{-4} \cdot (2 \cdot Y_e)^{\frac{2}{3}} \cdot \left(\frac{\rho_c}{10^{10} \text{ kg} \cdot \text{m}^{-3}} \right)^{\frac{1}{3}} R_\odot. \quad (47)$$

For example, in the case of completely ionized pure $^{26}\text{Fe}_{56}$ and $x_F = 10$, we have $\rho = 2.105 \times 10^{12} \text{ kg/m}^3$; this results in $M = 1.253 M_\odot$, $R = 3.568 \times 10^{-5} R_\odot$ ($= 0.389$ earth radii).

In Eq. (46), M is independent of R and hence ρ_c . This mass limit for white dwarf stars, in the relativistic limit of Eq. (33), is called the *Chandrasekhar limit*, or $M_{ch} = 1.46 M_\odot$. It is the largest possible mass of a white dwarf star. Degenerate stars of higher mass must take other forms such as neutron stars or black holes (discussed below). Figure 3 shows an intuitive way to understand how the *Chandrasekhar limit* comes about.¹¹ The figure shows $\log P_c$ vs. $\log \rho_c$ for the equation of state of white dwarf stars as the solid line. Also plotted as a dotted line is the inward pressure of gravity at the center of the star for two stellar masses, 0.8 and $1.5 M_\odot$ (the radius of the star is an implied variable). At lower masses, e.g., $< 0.8 M_\odot$, the system is

nonrelativistic and $P_c \propto \rho_c^{5/3}$. The slope of the equation of state in this case is larger than the slope of the P_c vs. ρ_c relation from gravity, and there is a solution for ρ_c, P_c . There is then a transition region that has a changing slope of P_c vs. ρ_c which still allows solutions. Finally, in the very relativistic limit, $P_c \propto \rho_c^{4/3}$ and the slope of the equation of state is parallel to that of the P_c vs. ρ_c relation from gravity. Thus, in the very relativistic case, there is no solution, and these more massive white dwarf stars are unstable. The last mass that allows a solution is M_{ch} , just less than $1.5 M_\odot$. Note that it is the transition from $E_e \cong p_e^2/2m_e$ to $E_e \cong p_e$ that loses a power of p_e and leads to this result. Very basic physics!

(ii) Neutron Stars

Stable degenerate stars with masses larger than M_{ch} are constructed by using the general relativistic Oppenheimer-Volkoff (OV) equations. The OV equations are solutions of Einstein's field equations describing the stellar structure for a nonrotating spherical star in hydrostatic equilibrium (time independent). We write them in a form that resembles Eqs. (36) and (37),

$$\frac{dm(r)}{dr} = 4\pi r^2 \rho(r), \quad (48)$$

$$\frac{dP(r)}{dr} = -\frac{Gm(r)\rho(r)}{r^2} \left(1 + \frac{P(r)}{\rho(r)c^2}\right) \left(1 + \frac{4\pi P(r)r^3}{m(r)c^2}\right) \left(1 - \frac{2Gm(r)}{rc^2}\right)^{-1}, \quad (49)$$

$$\frac{d\Phi}{dr} = -\frac{1}{\rho(r)} \frac{dP(r)}{dr} \left(1 + \frac{P(r)}{\rho(r)c^2}\right)^{-1}. \quad (50)$$

Baad and Zwicky¹² invented the idea of a “neutron star” and predicted that neutron stars are the remnants of supernovas. They did not make quantitative calculations but estimated that neutron stars would have a very small radius and high density. The first actual model calculation of neutron star properties was made by Oppenheimer and Volkoff.¹³ They solved the OV equations assuming an ideal relativistic gas of free neutrons as the equation of state, cf. Eq. (35).

Neutron stars are thought to form when the Fermi sea of electrons of the ionized matter in a white dwarf configuration fills beyond the energies available to β decay. This happens in the extreme relativistic electron limit, i.e., very high density. With the Fermi levels filled beyond the

energy of the electrons from neutron-beta decay, there is “no place for these electrons to go,” and inverse β decay is favored. This causes a “neutron drip” above a central density, ρ_c , of the star of about $4 \times 10^{14} \text{ kg/m}^3$. (Note that $\rho_{nuc} \cong 3 \times 10^{17} \text{ kg/m}^3$.) The neutron star is an exotic regime of matter that is not well understood. For white dwarf stars, observations of masses and radii are used as evidence for the confirmation of the stellar models. In the case of “neutron stars,” because of the lack of experimental knowledge about the equation of state at these extreme conditions, observations of masses and radii are used as a probe of this exotic state of matter.

Figure 4 shows the various stages of degenerate stars in neutron star models¹⁴ that were developed in the 1950s–1970s. These “nuclear” models assume extrapolations of simple low-energy nuclear physics to “nuclei” of $> 10^{57}$ nucleons, and $\rho_c \gg \rho_{nuc}$. I will argue below, when I discuss strange stars and Q-stars, that this may not be valid. The upper right hand corner shows a stability diagram of mass vs. ρ_c . The regions where $dm/d\rho_c > 0$ are generally stable. For $\rho_c < 10^{12} \text{ kg/m}^3$, stable white dwarf stars exist. For $2 \times 10^{16} < \rho_c < 5 \times 10^{18} \text{ kg/m}^3$, nuclear models indicate that neutron stars exist. Above this density range, there is great uncertainty of what states of matter might exist; however, the current consensus is that total gravitational collapse of the star occurs into a black hole above some limiting mass.

About 17 binary star systems containing at least one neutron star candidate have yielded good mass estimates of the neutron star(s). (How this measurement is made is discussed in Sec. 3b below.) All of these neutron star mass values lie in the range $1.35 \pm 0.27 M_\odot$ (Ref. 15) and are consistent with mass estimates from a number of nuclear neutron star models.

The possibility of identifying heavier compact objects as black holes relies, almost entirely, on being able to state categorically that the observed object has a mass larger than the maximum allowed mass of the heaviest stable compact stellar object. Conventional wisdom identifies the heaviest stable compact stellar objects as neutron stars described by nuclear models. In this approximation, we find a reasonably firm upper limit on the mass of a neutron star. Below, I reproduce the assumptions of Rhoades and Ruffini¹⁶ as I have quibbles about some of these that will become important when we discuss Q-stars. In our discussion of mass limits, initially we assume no rotation. As it turns out, rotation adds at most 20% to the mass limit as compared to no rotation.

Rhoades and Ruffini made the following set of assumptions in their derivation of the mass limit of neutron stars.

- A. General relativity is the correct theory of gravity, and thus the OV equations determine the equilibrium structure of the compact object.
- B. The equation of state satisfies the “microscopic stability” condition, $dP/d\rho \geq 0$. If this condition were violated, small elements of nuclear matter would spontaneously collapse.
- C. The equation of state satisfies the causality condition, $dP/d\rho \leq c^2$; that is, the speed of sound in the neutron star is bounded by the speed of light in vacuum.
- D. The equation of state below a matching density, $\rho_{mat} = 5 \times 10^{17} \text{ kg/m}^3$, is known ($\rho_{nuc} \cong 3 \times 10^{17} \text{ kg/m}^3$).
- E. The equation of state corresponds to a gravitationally bound compact object; that is, the stability of the compact object is provided by the attraction of gravity. (This is an implicit assumption of Rhoades and Ruffini.)

This set of assumptions yields an upper limit for the neutron star mass of about $3.6 M_{\odot}$ (Ref.17). Rotation brings this limit to about $4.3 M_{\odot}$.

(iii) Strange Stars, Q-Stars, and Black Holes

There is a theoretical class of compact objects that are not really covered by assumptions D and E above. For this class of objects, examples of which are “strange stars” and “Q-stars,” the equation of state is very different from those we have considered to this point because these (theoretical) systems do not need gravity to stabilize them. These are N-body systems that have a stable phase for bulk matter that dominates the gravitational attraction, even up to a limit of $1000 M_{\odot}$ in some models. These models are derived as approximate solutions to effective Lagrangian field theories. The nuclear approximation to the equation of state we have been considering above also originates in an effective field theory. In this case, one has an effective Lagrangian field theory with nucleons as the fundamental fermionic field and, in simplest approximation, pions as the force field. This approximation is the meat of theoretical nuclear physics. However, what effective field theory might best approximate reality for $M \gg M_{nucleus}$ (like 10^{57} nucleon masses) is not well understood. For $\rho_c > \rho_{nuc}$, a quark phase should certainly play a role. However, even well below ρ_{nuc} , new phases of nuclear matter, which do not manifest themselves in the nuclear physics regime, might exist that gain stability for bulk matter from the nuclear force, not gravity.¹⁸ This latter possibility has been shown to be consistent with nuclear physics data.¹⁹

I will give only a brief review of this approach in these lectures.²⁰ In these models, a low-energy effective field theory is used to describe a relativistic Fermi gas of quarks for strange matter stars or nucleons, and for Q-stars bound within a finite volume. For both models, the Lagrangian density has the form

$$\mathcal{L} = \bar{\Psi}[i\partial - m(\sigma) - g_V V]\Psi + \frac{1}{2}(\partial_\mu \sigma)^2 - U(\sigma) + \frac{1}{2}m_V^2 V_\mu V^\mu, \quad (51)$$

where Ψ is a fermion field, representing quarks for strange star matter, and nucleons for Q-star matter, and σ and V are effective scalar and vector fields, respectively. The scalar field, σ , has an effective potential $U(\sigma)$ and generates an effective fermion mass $m(\sigma)$. The vector field, V , has effective mass m_V and effective coupling g_V . In solving the above equation, we neglect the dynamics of the vector field. In many cases in the literature, the vector field contribution is neglected completely, and the operational equation becomes

$$\mathcal{L} = \bar{\Psi}[i\partial - m(\sigma)]\Psi + \frac{1}{2}(\partial_\mu \sigma)^2 - U(\sigma). \quad (52)$$

These equations are solved semiclassically. Only the Pauli exclusion principle for the fermions is treated quantum mechanically.

In the applications we are considering, this theory is used to describe a relativistic Fermi gas of quarks or nucleons bound within a finite region of space, i.e., a spherically symmetric compact stellar object. Including the vector repulsion between fermions, the Fermi sea is described by the Fermi momentum, k_F , and Fermi energy, E_F ,

$$E_F = \sqrt{k_F^2 + m^2} + \frac{\alpha_V k_F^3}{3\sqrt{3}\pi}, \quad \alpha_V = \frac{\sqrt{3}}{\pi} \left(\frac{g_V}{m_V} \right)^2, \quad (53)$$

where the parameter α_V gives the strength of the repulsive fermion (vector) interaction.

In this model, we take $U(\sigma)$ such that inside the bulk of the star, σ takes on a constant value, $\sigma = \sigma_{inside}$. The star has a very thin surface region, where σ undergoes rapid transition to a different constant vacuum value, $\sigma = \sigma_{vacuum}$.

In the approximation of *chiral symmetry* for the hadronic matter of the star, the fermions are massless inside the star, and $m(\sigma_{inside}) = 0$ ($m(\sigma_{vacuum}) = M_{nucleon}$). More generally, for this type of matter, $m(\sigma_{inside}) < M_{nucleon}$. This can result in a more energetically favorable configuration, i.e., a bound system, if the fermion energy inside the star is lower than that of free fermions by an amount greater than the gain in scalar field potential energy. (Note that we have not mentioned gravity yet.)

In the *chiral symmetry* case, including nondynamical effects of the vector field V , the equation of state is

$$\rho - 3P - 4U_0 + \alpha_V (\rho - P - 2U_0)^{\frac{3}{2}} = 0, \quad U_0 \equiv U(\sigma_{inside}). \quad (54)$$

In these models, the hadronic matter is a perfect fluid with the number of fermions $> 10^{57}$. Thus, gravity can be important and the OV equations are used in the formulation of the problem. These can be integrated using Eq. (54). The compact star boundary conditions define the stellar surface at the radius where the total hadronic pressure, $P_{\psi} - U_0$, vanishes. (Note that P in Eq. (54) includes effects from gravity as well as hadronic pressure.)

Table 1 shows typical parameters for strange stars and Q-stars. The strange star models depend on the *MIT Bag model* and are parameterized in terms of the “*Bag constant*.” Strange stars are a degenerate Fermi sea of massless quarks, including strange quarks, in a Bag. Q-stars are a quite different model, though the mathematics is similar to strange stars, being made of neutrons, protons, and electrons satisfying beta-equilibrium and local charge neutrality.

Parameters	Strange Stars ²⁰	Q-Stars ¹⁸
Fermions: Ψ	Quarks: u, d, s	Nucleons and electrons
Vacuum energy: U_0	Bag constant: $\cong (145 \text{ MeV})^4$	$(170 \text{ MeV})^4 - (10 \text{ MeV})^4$

Vector repulsion: α_v	0	$\sim 1.2 \times 10^{-4} \text{ MeV}^2$
Maximum stellar mass	$\sim 2 M_s$	$0.5 M_s - 400 M_s$
Maximum stellar radius	$\sim 10 \text{ km}$	3 km - 2300 km

Table 1. Typical parameters of strange stars and Q-stars.

Reference 18 also derives a limit, analogous to the Rhoades-Ruffini limit, yielding the equation of state with the largest possible maximum mass consistent with causality, microscopic stability, and GR. This maximum mass for Q-stars is $890 M_s$. The Q-star mass limit is far greater than the Rhoades-Ruffini limit and allows that stellar mass black holes do not exist. This very high mass limit results from the low density of a high mass Q-star compared to a conventional neutron star. The low density is theoretically possible for Q-stars since the hadronic forces largely provide for the stability of the star independent of gravity, unlike the case of conventional neutron stars where gravity is the dominant force that holds the star together. Both types of objects may exist in nature.

Figure 5 shows interior density vs. radius¹⁸ in part (a) strange stars, and part (b) Q-stars. Figure 5(a) shows curves for a range of strange star masses in units of M_s . In Fig. 5(b), the Q-star locally measured energy density curves are plotted vs. fractional radius, r/R . The curves correspond to the maximum mass Q-star resulting from the theory with various values of the dimensionless scaling parameter $\zeta = \alpha_v \cdot U_0^{\frac{1}{2}} \cdot \frac{\pi}{\sqrt{3}}$ and U_0 fixed at $(100 \text{ MeV})^4$; $\zeta = 0, 1, 4, 16$ have Q-star masses, $M/M_s|_{\text{max}} = 4.0, 5.8, 7.4, 8.4$, respectively. This value of U_0 is typically used in particle physics calculations when considering normal-sized hadrons. “Very low” density (and high mass) Q-stars can result if $U_0 \ll (100 \text{ MeV})^4$.

Figure 6 shows mass vs. radius¹⁹ in part (a)—strange stars, and part (b)—Q-stars. Figure 6(a) shows as solid curves the masses of conventional neutron stars predicted by a number of nuclear physics based theories. The dotted curve shows this relationship for one strange star theory. Figure 6(b) shows mass vs. stellar radius for *chiral* (solid lines) and *nonchiral* (dotted lines) Q-stars. The high mass Q-star curve results from $\zeta = 1.6$ and $U_0 = (85 \text{ MeV})^4$, while the low mass Q-star curve results from $\zeta = 8.9$ and $U_0 = (200 \text{ MeV})^4$. Two

conventional neutron star models, plotted as dashed lines, are shown for comparison. Figures 5(b) and 6(b) show that it is easy to obtain Q-star masses that exceed the Rhoades-Ruffini limit for neutron stars; however, strange star masses and radii are predicted to be very close to those of conventional neutron stars for $M/M_s > 0.5$.

(iv) Summary

In the above sections, we have briefly reviewed white dwarf stars, conventional neutron stars, and some unconventional stellar models, e.g., strange stars and Q-stars. White dwarf stars are well established experimentally by direct observation from ground- and space-based telescopes. There is very good agreement between extensive experimental data and theory. Neutron stars are less well understood as the experimental information about them is essentially limited to mass determinations, pulsar periods, and spectral energy and timing information, including those coming from space-based x-ray measurements of binary systems containing a neutron star candidate.

Conventional theory predicts that compact stellar objects with masses greater than the Rhoades-Ruffini limit for neutron stars must collapse into a black hole. As we shall explore later in these lectures, this mass limit is currently the primary experimental evidence for stellar black hole candidates. In addition, there exists spectral and timing information coming from space based x-ray measurements of x-ray binary systems containing a black hole candidate (BHC).

The bogus observation of a submillisecond pulsar in the late 1980s seemed to challenge the limits of rotational stability of conventional neutron stars. This stimulated theorists (for a while) to explore other theories that could accommodate such a startling observation, based on modern ideas in particle physics. Thus, an incorrect observation was one of the primary reasons for the invention of strange stars and Q-stars; it had the value of forging a new direction in theory. Unexpectedly, the theory of Q-stars had the additional important result of greatly exceeding the Rhoades-Ruffini mass limit for neutron stars before requiring collapse to a black hole. The Q-star mass limit is so large, at about $890 M_s$, that it could eliminate the practical possibility of stellar mass black holes.

Strange stars have been invented to closely mimic neutron stars except for their ability to spin faster. Thus for $M/M_s > 0.5$, strange stars and neutron stars are predicted to be very close in mass and radius. However, as Fig. 5(a) shows, below this mass range, strange stars have a much

smaller radius than neutron stars, and this might be a way of eventually experimentally distinguishing them.

Q-stars can be very different from neutron stars and black holes, and offer fertile ground for experimental observations. A Q-star having the same mass as the BHC Cygnus X-1, with $M/M_{\odot} = 16 \pm 5$, has a Q-star surface radius of about 80 km as compared to a black hole with a horizon radius of about 50 km. As we will discuss in some detail further in these lectures, for Cygnus X-1, it currently appears feasible to distinguish the Q-star and black hole hypotheses experimentally. The search for strong additional experimental evidence, beside mass limits, for (or against) stellar mass black holes is one of the more challenging areas of particle astrophysics.

3. Laboratories for Particle Astrophysics: X-Ray Stellar Binary Systems and Active Galactic Nuclei (AGN)

The first priority of physics is to obtain experimental information about objects in the universe that we wish to study. Without such experimental information, theoretical speculations can be very misleading. The seminal questions that concern particle astrophysics require relatively new and exploratory experimental techniques to study the exotic objects that theorists have posited should exist. In this section, we briefly review some of the most promising of such techniques that could yield experimental information about the nature of compact stellar objects beyond white dwarfs, and their relationship to gravity. In particular, experimental “proof” of the existence or nonexistence of black holes is central to this effort. In this case, “what is involved is not just the investigation of yet another, even if extremely remarkable, celestial body, but a test of the correctness of our understanding of the properties of space and time in extremely strong gravitational fields.”²

3a. Description of X-Ray Binary Systems

An x-ray binary system is characterized by an optically (and radio) visible star orbiting about an optically (and radio) invisible compact stellar object. However, the close environment of the compact stellar object is visible in x-rays. Figure 7 shows a schematic of such an x-ray binary system containing a BHC and an ordinary star. (Note that the figure is not to scale, with the accretion disk/black hole actually being much smaller than shown relative to the normal star.) Known BHC binary systems contain a stellar mass BHC with a mass in the range 3–30 M_{\odot} . Binary systems can also contain a white dwarf star or a neutron star.

For neutron stars and BHCs, two types of x-ray binary systems are observed, high mass x-ray binary systems, HMXB, and low mass x-ray binary systems, LMXB. HMXB contain a high mass supergiant star ($33 M_{\odot}$ for Cyg X-1) and a compact object. The compact object in a HMXB is typically a BHC, or a relatively young neutron star, which is usually a pulsar with a large magnetic field of $\sim 10^8$ T. LMXB systems contain a low mass main sequence star of about $1 M_{\odot}$, and a compact object. The compact object in an LMXB is typically a BHC or a relatively old neutron star, which has a reduced magnetic field of $\sim 10^4$ T and does not show pulsation. The phenomenology of these systems is discussed in Sec. 4a.

The critical potential surface, shown in Fig. 7, corresponds to the “Roche Lobe” of the binary system. Inside the Roche Lobe of both stars, but outside the stellar surface, the gravitational potential is dominated by a $1/r$ potential; here, the equipotentials are close to spherical. The crossover point is the L_1 Lagrange point (illustrated in the figure). At this point, the total force on matter is zero. The gravitational potential of an orbiting binary system is conducive to the formation of an accretion disk about the compact object. Figure 8(a) shows how such a mass transfer works to create a strong x-ray source. Mass from the normal star can either be transferred via stellar wind to the accretion disk, or if the normal star is large enough, it will overflow its Roche Lobe and transfer matter to the accretion disk. An accretion disk forms due to the angular momentum of the matter from the normal star in orbit about the compact object. Frictional forces in the accretion disk allow a net transfer of angular momentum outward, allowing matter to flow inward, as shown in Fig. 8(a) (Ref. 21). This matter is strongly heated in the deep gravitational potential well of the compact object and eventually hits the surface of the compact star, in the case of nonblack holes. In this process, roughly 10% of the accreted rest-mass energy may be converted into mainly X-radiation. Thus, accretion of material onto a compact object can be a considerably more efficient energy source than nuclear fusion. Enormous luminosity of these binary systems results with luminosity of 10^{31} W in 1–20 keV x-rays being fairly common. (The sun emits 3.9×10^{26} W integrated over all wavelengths.)

3b. Description of Active Galactic Nuclei (AGN)

Active Galactic Nuclei, or AGN, are thought to be the product of enormous black holes with masses in the range 10^6 – $10^{10} M_{\odot}$ at the center of some galaxies.²² Galaxies with AGN are much less common than normal galaxies. The first to be discovered are *Seyfert galaxies*, discovered optically in the 1940s (by Seyfert); they appear to be spiral galaxies, but have star-like nuclei.

Their optical emission spectra are quite different from normal galaxies. The next class of AGN to be discovered were a subclass of radio galaxies. By the mid-1950s, it was known that radio galaxies were sources of very large fluxes of high-energy particles and had very strong magnetic fields. A few of these had prominent star-like nuclei in the optical and were called *N-galaxies*. These were similar to Seyfert galaxies in their emission spectra. However, the relationship between Seyfert and N-galaxies was not clear at that time.

In the 1960s, *quasars* were discovered by Martin Schmit. In 1962, he found that the strong radio source and quasistellar object, 3C 273, has a redshift of $z = \Delta\lambda/\lambda = 0.158$, which, according to Hubble's law, places it at about 2×10^9 light years away ($H_0 = 50$ km/s/Mpc). The observed luminosity of 3C 273 implied an intrinsic luminosity in the visible and radio frequencies for the object of more than 10^3 times that of the entire Milky Way galaxy (our galaxy that has a luminosity of $2 \times 10^{10} L_\odot = 8 \times 10^{36}$ W). Besides having the appearance of a point object in the photographs, the quasar varied noticeably in brightness. Following this discovery, many more quasars were found, all of them characterized by strong radio emission, stellar appearance, and very great distances. Soon after, radio-quiet quasars were discovered. They are similar to radio-loud quasars in the optical range but are relatively weak sources of radio emission. Quasars are among the most energetic examples of AGN known. Optical observation of relatively close quasars show that the source of the very strong optical emission is the nucleus of a galaxy.

Some of the most energetic examples of AGN are the BL Lacertae, or BL-Lac, objects, and the rapidly variable (in the optical, x-ray, and gamma-ray) quasars called blazars. These are a subset of the quasars and demonstrate variability in luminosity on timescales of hours to days, depending on the wavelength. This implies that the source of this radiation must be quite compact. In the case of BL-Lac objects, the optical spectra are normally featureless and the continuum radiation is strongly polarized. They also show strong x-ray and very strong gamma-ray emission to tens of GeV. It is plausible that for BL-Lac objects, we are directly observing the primary source of energy from the AGN.

We now have a model of AGN that can qualitatively explain the observations described above. In this model, the AGN is powered by a massive black hole with masses in the range 10^6 – $10^{10} M_\odot$ at the center of a galaxy. Figure 8(b) shows the energy flow from the AGN. The black hole, by a mechanism that is not completely understood at this time, generates two opposing jets of relativistic plasma and radiation that are highly collimated via relativistic beaming. These jets

are the source of the gamma-rays, and eventually, the strong radio signals seen. The inner edge of the accretion disk is the main source of x-rays, and also provides the material flow to the jets. Figure 9(a) shows a ground-based superimposed optical-radio image of the galaxy NGC 4261, which contains an AGN. Notice the scale on the figure. The galaxy is an elliptical with two jets of material emanating from its core region. The jets in part (a) of the figure are the source of very strong radio signals. The core of the galaxy is exposed in Fig. 9(b), showing a Hubble Space Telescope²³ image of the central region of the galaxy with the radio jets superimposed (not to scale) for orientation. This image was taken before the Hubble was repaired. The disk-like structure seen in the figure is not an accretion disk as it does not show the differential rotation as a function of r necessary to transfer material in towards the center. Spectroscopic observations of this disk structure indicate that it is rotating as a solid body. The actual AGN region is contained in the bright dot in the center of the hole in the “donut” and is not resolved in this picture. Subsequent pictures with Hubble after its repair have left open the question of the nature of the central region of this AGN. There is currently no direct experimental evidence for a black hole at the center of NGC 4261. However, we might speculate, and Fig. 9(c) shows the resulting model of what the central region might look like.

The model of an AGN shown in Figs. 8(b) and 9 allows a natural explanation of many of the phenomena observed in AGN and unifies the observations of the various types of AGN. A Seyfert galaxy is an evolved quasar. A quasar is a particularly powerful AGN, the large distance to the quasar dimming the rest of the galaxy. Radio-loud AGN galaxies have the orientation of the jets to the earth, maximizing the radio transmission from the galaxy, while radio-quiet AGN galaxies are oriented too poorly to transmit to Earth. Blazars are oriented with the jets from the AGN pointing at the earth. In this way, we “see” right into the center of the AGN. Finally, the rapid variability of AGN is due to the compact black hole “engine” at their centers. This all seems to hang together; however, the model of super massive black holes as the driving engine of AGN is still controversial and has only indirect experimental evidence supporting it.

3c. X-Ray Binary System Orbital Parameters

Figure 10 shows a schematic of an x-ray binary system as viewed parallel to the orbital plane. In the figure,

- M_x = mass of x-ray source (compact object)
- M_{opt} = mass of optical companion (normal star)

- $q = M_{opt}/M_X$
- i = orbital plane inclination angle, where the z' direction is to the observer
- $a = a^x + a^{opt}$
- a^x = semimajor axis of the x-ray source
- a^{opt} = semimajor axis of the optical companion.

Figure 11 defines an x-ray binary system's orbital parameters. Referring to this figure:

- Periastron = position along the optical companion's orbit nearest to the x-ray source
- ϕ = angle of the optical companion from the periastron, measured in the orbital plane
- Line of nodes = common x and x' axis, defined by the line of intersection of the orbital plane and projected observation plane, where the projected observation plane is perpendicular to the z' direction
- i = orbital plane inclination angle
- ω = angle of periastron from the line of nodes, measured in the orbital plane
- e = eccentricity of the optical companion's orbit
- P = period of the binary system orbit.

In order to determine the values of the above defined parameters, we measure two observable quantities: the intensity of the light emitted by the optical companion as a function of time (i.e., the binary system's light curve) and the Doppler shift of the light emitted by the optical companion as a function of time. (Note that "light" is really electromagnetic radiation, as radio Doppler measurements and x-ray eclipses also yield information about binary system parameters.)

The Doppler shift is given by

$$\frac{\lambda}{\lambda_0} = \sqrt{\frac{1+\beta}{1-\beta}}, \quad \beta = \frac{v_{z'}^{opt}}{c}, \quad (55)$$

where $v_{z'}^{opt}$ is the velocity of the optical companion projected along the z' axis, called the "radial velocity." Defining

$$1 + z = \frac{\lambda}{\lambda_0}, \quad (56)$$

Eq. (55) can be solved for the radial velocity,

$$v_z^{opt} = c \left(\frac{(1+z)^2 - 1}{(1+z)^2 + 1} \right). \quad (57)$$

We can relate the physical observables to the orbital parameters of the x-ray binary system in a few ways. An FFT (Fast Fourier Transform) of the binary system “light” curve may yield the period of the binary system. The source of the information may either be eclipses of the x-ray source by the optical companion, which gives information in the x-rays from the compact object, or ellipsoidal variations in the optical light curve due to tidal deformations in the optical companion from gravitational interaction with the compact object. In order to get x-ray eclipse information, the orientation of the binary system orbital plane must be nearly parallel to the line of sight from the earth to the binary system (depending on the geometry of the binary system, and the size of the compact object and optical companion).

We can also use the Doppler shift data to determine the orbital parameters. The radial velocity of the optical companion is related to its orbital parameters by its equations of motion

$$\psi(t) \equiv \omega + \phi(t), \quad r^{opt}(t) = \frac{a^{opt}(1 - e^2)}{1 + e \cos \phi(t)}. \quad (58)$$

These equations and the orbital definitions give

$$v_z^{opt} = \sin i (\dot{\phi}^{opt} \sin \psi + r^{opt} \dot{\psi} \cos \psi). \quad (59)$$

Kepler’s second Law, with r^{opt} eliminated by substitution of Eq. (58), is

$$\dot{\phi} = \frac{2\pi(1 + e \cos \phi)^2}{P^3 \sqrt{1 - e^2}}. \quad (60)$$

Substituting Eqs. (58) and (60) into (59) gives

$$v_z^{opt} = K^{opt} [\cos(\omega + \phi(t, e, P)) + e \cos \omega], \quad K^{opt} \equiv \frac{2\pi a^{opt} \sin i}{P \sqrt{1 - e^2}}. \quad (61)$$

K^{opt} is called the semiamplitude of the optical radial velocity curve.

Figure 12 shows data from the binary system V404 Cyg. Radial velocity (km/s), obtained from the Doppler shift data through Eq. (57), is plotted as a function of orbital phase (rad), assuming a periodic variation. P for the system is obtained from this curve. From $v_{\max/\min}$, we find from Eq. (61)

$$\begin{aligned} v_{\max/\min} &= K^{opt} (\pm 1 + e \cos \omega), & \frac{v_{\max} - v_{\min}}{2} &= K^{opt}, \\ \frac{v_{\max} + v_{\min}}{2} &= K^{opt} e \cos \omega \equiv \bar{v}, & \frac{v_{\max} + v_{\min}}{v_{\max} - v_{\min}} &= e \cos \omega \end{aligned} \quad (62)$$

Integrating the data of Fig. 12 in two ways then yields another relation between orbital parameters,

$$A_{1,2} \equiv \int_{v_{1,2}}^{\bar{v}} (v_z^{opt} - \bar{v}) dt, \quad \text{where } v_1 = v_{\max}, \quad v_2 = v_{\min}. \quad (63)$$

Equation (63) is related to the orbital parameters by

$$\frac{2\sqrt{|v_{\max} v_{\min}|}}{v_{\max} - v_{\min}} \cdot \frac{A_2 + A_1}{A_2 - A_1} = e \sin \omega. \quad (64)$$

Equations (62) and (64) then solve the orbital parameters, K^{opt} , e , and ω in terms of radial velocity data.

P , K^{opt} , e , and ω can be used to determine limits on the x-ray source's mass. Combining Kepler's third law,

$$P^2 = \frac{(2\pi)^2}{G(M_x + M_{opt})} a^3, \quad (65)$$

where G is Newton's gravitational constant, with the definition of K^{opt} , Eq. (61), and moving all orbital parameters of the optical companion to one side of the equation, we find

$$\frac{(K^{opt})^3 \cdot P \cdot \sqrt[3]{1-e^2}}{2\pi G} = \frac{M_x \sin^3 i}{(1+q)^2} \equiv f(M), \quad (66)$$

where $f(M)$ is called the *optical mass function*. The value of $f(M)$ for an x-ray binary system, which depends on readily determined orbit parameters of the optical companion, gives a lower limit to the x-ray source's mass, since $\sin^3 i / (1+q)^2 < 1$; that is,

$$M_x > f(M). \quad (67)$$

3d. Using Orbital Parameters to Determine Compact Object Masses

In the following sections, we show applications of the techniques developed in Sec. 3c. These spectral/mechanical methods are currently the most reliable way to determine the mass of a compact object. Section (i) shows mass solutions for stellar mass objects, while Sec. (ii) discusses an AGN solution.

(i) Some Leading Stellar Black Hole Candidates

Figure 13 shows the orbit solutions for a number of x-ray binary systems thought to contain a black hole as the x-ray source. The primary reason that a BHC is preferred for these systems is the high mass of the x-ray source in these solutions compared to the Rhoades-Ruffini mass limit for neutron stars. Later in these lectures, we will discuss information coming from the x-ray spectra of these objects that puts them in a common category. In particular, the millisecond and submillisecond time variability of these x-ray sources can yield important information about their structure. For all but one of the cases, V404 Cyg, the optical mass function is less than the Rhoades-Ruffini mass limit. However, additional information about these systems allows a unique mass determination for the optical companion and x-ray source. The figure shows these

values of M_x and M_{opt} in the two lobes of the binary system cartoons. In general, these values are model dependent and do not have the reliability of $f(M)$ which is also shown in the figure for each system as is the orbital period.

(ii) The Black Hole Candidate in the AGN of M87

Though observations of the central region of NGC 4261, discussed in Sec. 3b, have not yet provided strong experimental evidence of a massive black hole, observation of the giant elliptical galaxy M87 has recently been more fruitful. M87 is a nearby galaxy in the Virgo cluster at a distance of about 15 Mpc. It is a large elliptical galaxy that is a strong radio source with an AGN and a mass of about $40 \times 10^{11} M_{\odot}$, or about 20 times the Milky Way. Figure 14(a) shows a recent NASA Hubble Space Telescope image²⁴ of a spiral-shaped disk of hot gas in the core of the AGN of M87. This galaxy has long been a favorite choice for seeking further evidence that radio ellipticals have central engines fed by a surrounding disk. The powerful optical synchrotron jet, nonthermal radio source, and large velocities of ionized gas in its nucleus singled out M87 as one of the earliest examples of a galaxy with an AGN. The bright streak of light moving from the center of the galaxy, at about 45° clockwise from 12 o'clock in the figure, is the optical synchrotron jet of high-energy particles thought to be powered by the central engine of the AGN. This photograph was taken after the December 1993 repair of the Hubble telescope.

Spectroscopic observations of ionized gas in circular motion close to the nucleus of M87 can provide a powerful and straightforward way to look for the Keplerian rotation curve, which could be a signature of a massive black hole. The dynamics of the millions of stars, gas, and dust in the neighborhood of the galactic nucleus is much more complex than that of a simple stellar binary system; however, a massive central black hole will affect the kinematics of this ensemble by producing a rapidly rotating accretion disk containing stars, gas, and dust, centered on the black hole. Consequently, the HST team took narrow band visual images of M87 to look for such an organized structure in the ionized gas. These images, particularly Fig. 14(b) which shows an enlargement of the central accretion disk feature, indicate that the ionized gas in the nucleus has indeed settled into a rotating disk. If this is true and there is a massive black hole in the center, the rotation velocity in the disk will rise toward the center rather than decrease to zero as in a galaxy with no central mass.

Figure 14(b) shows an enlargement of the central accretion disk feature, and the six locations (small circles in the figure) where HST spectrographic observations²⁵ were made

measuring the radial velocity of the visible matter in the neighborhood of the nucleus of M87. The angular size of the circles is 0.26 arc seconds. Two of the measurements were made at diametrically opposite locations, centered 0.25 arc seconds to either side of the nucleus, along the major axis that is perpendicular to the jet of M87; the red circle is position 5, and the blue circle is position 6. A third measurement was made at the center of the nucleus, the black circle at position 4. Figures 14(c) and 14(d) show these three spectrographic measurements containing lines from H_{β} , O_{III} in 14(c), and O_I and unresolved $H_{\alpha} + N_2$ lines in 14(d). The position of the spectroscopic lines are indicated by the colored symbols at the top of the graph.

The spectra for positions 5 and 6, centered 0.25 arc seconds to either side of the nucleus, show clear spectral features that are redshifted and blueshifted, respectively, by approximately equal amounts. The observed radial velocity difference between positions 5 and 6 is 1000 ± 100 km/s, averaged over a number of emission lines. (This corresponds to a velocity difference of about 1.5×10^3 km/s projected in the plane of the galaxy.) The spectrum from the center of the nucleus, position 4, shows highly broadened emission features corresponding to a Δv of about 1.6×10^3 km/s (projected in the plane of the galaxy) consistent with a cusp in the velocity distribution at the center. The velocities lead to the conclusion that M87 contains a disk of ionized gas at its core rotating around a central mass of $2.4 \pm 0.7 \times 10^9 M_{\odot}$.

The current Hubble resolution of about 0.26 arc seconds at a distance of 15 Mpc corresponds to about 18 pc, while a black hole of $2.4 \times 10^9 M_{\odot}$ has a diameter of 1.4×10^{10} km, or 4.5×10^{-4} pc. Thus, one can only indirectly infer that a black hole is the source of this mass accumulation in the nucleus of M87. Weighing all the evidence, the authors of Ref. 25 find the most plausible explanation to be a central black hole.

3e. Using Fast X-Ray Timing to Measure the Compact Size of Compact Stellar Objects

The paragraphs above bring the size of BHCs to our attention. So far in my discussion of the observation of BHC systems, I have not carefully discussed ways to measure the size of BHCs. In the case of M87, the optical resolution of the Hubble gives a lower limit on the size of a central BHC of about 18 pc, much larger than the theoretical size of the hypothesized black hole.

Besides being a strong optical and radio emitter, M87 also has strong x-ray emission of about 10^{36} W (2–10 keV) (Ref. 26). If the x-ray emission showed “intrinsic” variability (removing Poisson noise) on the timescale of about a day (and no faster), this would imply that the source of the radiation had a size of about 9×10^4 sec or 3×10^{10} km. (Other AGN x-ray

sources show variability on timescales as short as hours.) Such an observation would then imply that an object about the size of a $2.4 \times 10^9 M_\odot$ black hole was the source of the radiation, and so add much more credence to the black hole hypothesis. Unfortunately, no such evidence of x-ray variability currently exists for M87. However, when there is variability, the technique of using x-ray timing measurements is a powerful way to estimate the size of compact objects.

(i) X-Ray Timing Measurements for Cyg X-1

Cyg X-1 (cf. Fig. 13) is a binary star system containing an optically visible ninth magnitude supergiant B star and an unseen companion. As discussed in Sec. 3d(i), the mass estimate for the B star is $33 M_\odot$ and for the unseen companion $16 M_\odot$. It is this large mass of the unseen companion that qualifies it as a BHC. The system has an accretion disk about the unseen companion that is the source of the x-rays, and it is fed by matter infall from the B star. Before discussing the x-ray timing measurements that give evidence to the very compact size of the unseen companion in the Cyg X-1 system, we need a bit more theoretical background.

In general relativity (GR), the effective potential V for a test particle of mass m and angular momentum L in the Schwarzschild geometry of a concentrated mass M is²⁷

$$V = m\sqrt{(1 - 2M/r) \cdot [1 + L^2/(mr)^2]}, \quad (68)$$

where the effective potential is defined by

$$m^2(dr/d\tau)^2 + V^2(r) = E^2. \quad (69)$$

E is the energy of the particle, and τ is the proper time.

Figure 15 shows V/m , the effective potential profile, and E/m , various energies of the system shown as the two horizontal lines and the five dots, vs. r/M for various angular momenta, \bar{L}/M , where $\bar{L} = L/m$. The Newtonian approximation for the case $\bar{L}/M = 433$ is shown as the dashed line to be compared to the exact GR solution. In the asymptotic limit, $r/M \rightarrow \infty$, GR tends to the Newtonian approximation.

The figure shows effective potential profiles for nonzero rest-mass particles with \bar{L}/M between 4.33 and $3.464 = 2\sqrt{3} + \epsilon$, orbiting a Schwarzschild black hole of mass M . The lines correspond to particles with stable bound orbits; the dots correspond to particles with stable circular orbits. Such orbits only exist for $\bar{L}/M > 2\sqrt{3}$. For smaller \bar{L}/M , the orbit becomes unstable, and the particle will always fall into the black hole. The radius of this last stable circular orbit is $r_{ls} = 6M$, and the energy per unit mass of a particle in the last stable circular orbit is 5.72%. (Remembering that $R^{sch} \equiv 2GM/c^2 = 2M \cong 3(M/M_{\odot})$ [km], $r_{ls} = 3R^{sch} \cong 9(M/M_{\odot})$ [km].) Thus, a particle starting far from the black hole with little energy gains 5.72% of its rest mass by the time it has spiraled into the innermost stable orbit about the hole. This conversion of rest mass to other forms of energy has much greater yield than does nuclear burning, which releases a maximum of 0.9% of the rest mass ($H \rightarrow Fe$).

Now back to the Cyg X-1 system. Generally, the accretion process generates rapid and violent fluctuations in x-ray luminosity. Observations and models indicate fluctuations on a broad range of timescales. Several accretion disk models of binary systems containing a black hole, with the general properties of the Cyg X-1 system, indicate that a large fraction of the x-ray luminosity from the system originates in the region of the inner edge of the disk, which is defined by r_{ls} . In analyzing the time series of x-ray counts coming from Cyg X-1, one would then expect to observe fluctuations on a broad range of timescales, with a cut-off in x-ray power at the timescale corresponding to the innermost stable orbit of the accretion disk. Naively, this would be at $\Delta t \approx 2r_{ls}/c$. For the unseen companion in Cyg X-1, modeled as a black hole of mass $16 M_{\odot}$, this timescale corresponds to about 1 ms.

A measurement of the timescale of this cut-off has been made by the HEAO A-1 experiment.²⁸ Figure 16(a) shows the HEAO satellite, which had a complement of four major experiments designed to observe astronomical sources in the low energy x-ray to low energy gamma-ray spectral region. Figure 16(b) shows the A-1 experiment in some detail. This experiment was built by NASA and NRL, and was designed to be a survey instrument sensitive to x-rays in the 1–30 keV energy band.²⁹ It was operational during the years 1977–1979. The experiment is basically a collimated thin-window multiwire proportional chamber array, with a net aperture of about 1 m^2 . The angular acceptance (FWHM) of the collimators is given in the figure, with each proportional chamber module, 1–7, having the $x \times z$ acceptance printed on it. The long direction of collimation is parallel to the long direction of the module (along the x -axis). Much of the time, while in the survey mode, the HEAO satellite was spinning about the z -

axis (which points towards the sun). Typical photon timing information was at 5 ms and longer timescales; however, a number of special telemetry runs were made with 7.8 μ s timing resolution. Unfortunately, as is often the case in space-based experiments, all did not go well. Soon after launch, about 2/3 of the effective area was lost due to module failures (which were never completely understood). In addition, energy pulse-height information was essentially lost for all the data due to a serious malfunction in the ADC system. No way to drop the beam and go into the IR to fix these problems!

On May 7, 1978, HEAO A-1 was taking pointed data on Cyg X-1 while the source was in the “low” state (the state believed appropriate to observe the core of the x-ray source, see Sec. 4(a)). The average count rate observed by A-1 was 1020 Hz, or a mean energy flux of 1.25×10^{-11} W/m² integrated over the 1–30 keV range. This corresponds to a mean source luminosity of about 10^{30} W in this x-ray band, using the current estimate of the distance to Cyg X-1 of 2.5 kpc.

The A-1 proportional counter detector employed for the observation had a net aperture of 1650 cm² and a $1^\circ \times 4^\circ$ (FWHM) field of view. Data were received in real time during one HEAO pass over a ground receiving station for a total of nine minutes. During the pass, the satellite’s 128 kbit/sec data transmission rate was used, while data were being taken by A-1 at that same rate. (The normal A-1 data taking rate was much lower.) The data stream had a “1” or “0” set every 7.8 μ s, with a “1” indicating that at least one x-ray event had been detected in that time interval. Note that for Poisson-distributed events of average rate 1020 Hz, the probability of more than one event falling in a 7.8 μ s interval is 8×10^{-3} . No photon energy information was recorded for the events in this transmission mode.

The analysis of these data to determine the intrinsic time variability of Cyg X-1 is complicated by the purely statistical fluctuations in the x-ray luminosity. A contamination arises at the shorter timescales from fluctuations on longer timescales “leaking” into the measured power at shorter timescales; this statistical effect has to be unfolded from the data. The analysis of Ref. 28 used a specially constructed algorithm to deal with this effect.

A brief description of the analysis method is as follows:

- The determination of variability on a given timescale must be measured in the presence of other (possibly contaminating) variability timescales.
- Data (counts) from the entire nine-minute, 7.8 μ s sample were sorted according to their time of occurrence into sets with ten bins per set. This was done for a fixed bin width for all the data. This yields many ten-bin sets over the entire data sample.

- Fitting a constant mean rate, $\langle n_i \rangle$, to each independent ten-bin set, a value of χ^2 was determined for each set.
- The sorting and fitting was done six times with bin widths (time resolution, Δt), 0.3, 1, 3, 10, 30, and 100 ms. The lowest resolution used was much bigger than the intrinsic resolution of 7.8 μ s.
- $\langle n_i \rangle$ was determined separately for each time resolution, which implies nine degrees of freedom for each fit. (Ten data, and one free constant in the fit.)
- A distribution of χ^2 resulted from the many fits at each time resolution.
- Variability at each resolution was assessed by comparing the integral of the distribution of χ^2 found for all sets with that bin width, with the integral distribution theoretically expected for Poisson randomly distributed events into the same bin width (at the same mean rate, $\langle n_i \rangle$).
- Figure 17 shows the two distributions for each time resolution. A clear excess is found for all of the curves derived from the data compared to the curves for purely Poisson distributed events, except at the shortest timescale where no excess is observed. Given that at the shortest timescale $\langle n_i \rangle \cong 0.3$ events, a Poisson statistics Monte Carlo calculation was done as well as the analysis described above. The Monte Carlo points are shown as the x 's in the figure; these points are displaced down for the clarity of the figure. The shape of the Monte Carlo agrees well with that of the data, with no excess within errors indicated.
- Figure 18 shows the relative power for each timescale. The vertical error bar is the statistical error on the relative power horizontal; the horizontal error bar defines the timescale of each point. The relative power is calculated for each bin width using the formula (see appendix of Ref. 28)

$$P_{rel} = \frac{[\langle \chi^2 \rangle - \langle \chi^2 \rangle_{Poisson}]}{\langle N \rangle - 1}, \quad (70)$$

where for each time resolution, Δt ,

$$\langle N \rangle = \sum_1^{10} \langle n_i \rangle \cong 1020 \times (10\Delta t) \text{ counts}, \quad (71)$$

where 1020 counts/sec was the average total x-ray rate into the detector from Cyg X-1 during the measurement. The results are also summarized in Table 2.

Figure 18 and Table 2 show strong evidence for the predicted cut-off at a timescale of about 1 ms and indicate that the unseen object in Cyg X-1 is indeed compact with a diameter of about or less than 1 ms, or 3×10^2 km.

The analysis technique used by Ref. 28 is somewhat specialized and difficult to use. A more general technique for this type of *multiresolution analysis* is based on Wavelet methods. A brief introduction to Wavelet methods is given in Appendix A of these lectures.

Distribution	Mean χ^2	Relative Power
Calculated from Poisson distribution for a mean of three events in ten bins.	8.75	...
Data in 0.3 ms bins	8.78 ± 0.01	0.014 ± 0.005
Data in 1 ms bins	9.72 ± 0.02	0.08 ± 0.002
Data in 3 ms bins	10.60 ± 0.05	0.054 ± 0.002
Data in 10 ms bins	12.2 ± 0.1	0.032 ± 0.001
Data in 30 ms bins	16.7 ± 0.2	0.026 ± 0.001
Data in 100 ms bins	37.7 ± 0.4	0.029 ± 0.001
Expectation value for independent events	9	...

Table 2. Mean χ^2 and relative power from Cyg X-1 x-rays.

4. X-Ray Astrophysics

This section focuses on the experimental and phenomenological aspects of x-ray astrophysics. X-ray spectral and timing information can be useful in distinguishing the different types of x-ray binary systems discussed above. Such information can be used in a general way as an adjunct to the mass determination of the compact x-ray source to characterize neutron star vs. BHC systems. In addition, detailed analysis of timing information, as discussed in Sec. 3e, can yield quantitative information on the structure of these systems.

Figure 19 shows the HEAO A-1 x-ray all-sky map.²⁹ The HEAO A-1 experiment was described in Sec. 3e(i). The all-sky map shows about 1000 x-ray sources, many of which are binary systems with a compact stellar object. The size of the dot is proportional to the log of the intensity of the object. Sco X-1, a LMXB system containing an old neutron star, is by far the brightest nontransient source in the sky. According to the HEAO A-1 catalogue, its intensity in 1–30 keV photons is 37.2 counts/sec/cm².

Since x-rays from space are totally absorbed by the Earth's atmosphere, experiments that measure astronomical sources of x-rays must be done in space using satellite experiments. Figure 20 shows a cartoon of the typical x-ray timing experiment in orbit. As contrasted with x-ray imaging experiments, which have very fancy x-ray focusing optics and CCD detectors with poor timing capability, timing experiments are very simple. (This includes the new generation of timing experiments, USA and XTE discussed below, to be launched over the next couple of years.) As the figure shows schematically for the USA experiment, they consist of an array of multiwire proportional chambers (MWPC), two or more, shadowed by mechanical collimators that limit the field of view to a few degrees or less. The satellite can be pointed at a source as is the case in the figure or can be rotating in a survey mode. Past missions tended to spend considerable time in survey mode, while the current generation of experiments will be pointed.

The intrinsic timing resolution of a multiwire proportional chamber is well within a μsec . However, on-board data storage and telemetry bandwidth limitations have restricted past experiments to operate, with minor exception (e.g., HEAO A-1), with ≥ 1 msec timing resolution. Though the data collection deadtime from a single MWPC is about 20 μsec in the new generation of instruments, an array of more than one MWPC allows effective inter-event timing to 1 μsec . In addition, improvements in onboard data storage hardware and telemetry rates allow the new generation of experiments to actually take advantage of the 1 μsec timing

resolution on a routine basis. Most of the data that comes down from USA and XTE will have $<$ few μ sec timing resolution as well as some energy information for each γ event.

4a. X-Ray Discriminants of Black Holes vs. Neutron Stars

We start our discussion by considering the best studied BHC (BHC): Cyg X-1. This BHC is one member of a binary star system that is extensively discussed in the literature.³⁰ Cyg X-1 is a binary star system with Right Ascension (RA) $\alpha = 19^{\text{h}} 56^{\text{m}} 28.9^{\text{s}}$, and Declination (Dec) $\delta = 35^{\circ} 03' 55''$. The system is about 2.5 kpc (8.15 ly) distant from earth and is made of an unseen compact object, its compactness determined from x-ray timing data as discussed in Sec. 3e(i), and a visible stellar companion. The companion star, HDE 226868, is a ninth magnitude supergiant B star that showed a simultaneous radio and x-ray intensity transition identifying it as Cyg X-1's companion. The x-ray source was the compact object and its accretion disk, while the radio source was the B star. The system also shows a 5.6-day period as a spectroscopic binary and the same period in soft x-ray variability.

Using the association of the B star, the current best estimate of the mass of the compact object is $M_x = 16 \pm 5 M_{\odot}$; this solution also yields $33 \pm 9 M_{\odot}$ for the B star. This analysis was done using the optical mass function, the spectral type of the B star, O-9.7 lab, the absence of eclipses, and an estimate of the distance at 2.5 kpc from spectral reddening (interstellar dust). The analysis also shows a strong limit of $M_x > 7 M_{\odot}$. Optical photometry revealed ellipsoidal variations due to tidal deformation of the B star that confirmed the orbital period and indicated a mass ratio consistent with spectroscopic findings.

There is a concern with this analysis. In most HMXB systems, the visible star is found to be undermassive by a factor of two to three for its temperature and luminosity. Some models indicate that the primary in a black hole binary might be very undermassive. However, the best mass determination for the B star companion for Cyg X-1 indicates that it has not lost (or accreted) a large fraction of its mass during its evolution.

Even with the caveat above, Cyg X-1 is arguably the best stellar mass BHC that we know of. With a lower limit on M_x of $7 M_{\odot}$, the compact object mass is well above the Rhoades and Ruffini limit. This object has thus been carefully studied over the past 20 years in the x-ray to characterize the x-ray emission of what many believe to be a black hole binary system. These observations have led to a standard phenomenology of a BHC. Even though there may not be a mass determination for a binary system, if it shows Cyg X-1 like x-ray behavior, it is labeled a

BHC. As I will show soon, there are a number of other systems with $M_x > 3 M_\odot$ that also show x-ray behavior very similar to Cyg X-1.

On monthly to yearly timescales, the 2–30 keV x-ray emission from Cyg X-1 exhibits cycling between a “high” and “low” state, where the “high” state has about a factor of two greater overall intensity than the “low” state. The “low” state has the harder x-ray spectrum, and millisecond variability is most readily detected in this state. The “high” state sets in on a timescale of days and lasts for about a month. An intense spectral component appears in the 3–6 keV band in this state. The luminosity in the “high” state is over 6×10^{30} W.

The behavior of BHC binary systems is contrasted in parts (a) and (b) of Fig. 21 with x-ray observations from HMXB and LMXB systems, respectively, that contain a neutron star. Part (a) shows data from Cen X-3, an HMXB that shows regular pulsations. The energy spectrum shows a power law behavior with a sharp cut-off and structure in the form of cyclotron lines. The latter results from the large magnetic field of about 10^8 T that are associated with younger neutron stars.

Figures 21(c) and 21(d) summarize the features described above that define the expected x-ray observations of a BHC x-ray binary system.³¹ These two parts of the figure use data from GS/GRS1124-68 and Cyg X-1, demonstrating the high and low states, respectively. Note that BHC binary systems can be either HMXB or LMXB. The combination of msec variability and hard power law x-ray energy spectrum seem unique to BHC systems.

Figure 21(b) shows data from Aql X-1, a LMXB containing an older neutron star. This object shows type I x-ray bursts and an energy spectrum that can be described as a thermal bremsstrahlung spectrum. The type I x-ray bursts occur periodically on the surface of the neutron star. This is driven by the accretion of material to a critical value on the surface. When the critical value is exceeded, a rapid nuclear burn of this material results. This is a key indicator that a LMXB system contains a neutron star rather than a BHC, as a BHC has no surface to allow accumulation of material. Unfortunately, such x-ray bursts can appear very rarely. For example, the LMXB Cir X-1 was long thought to harbor a BHC as it showed a very soft spectrum and msec time structure in the x-rays. However, recently it also showed a classical type I x-ray burst that immediately changed its classification to a neutron star system. These systems show aperiodic variability and quasiperiodic oscillations that are thought to originate in the accretion disk dynamics; they do not show regular pulsations. They also show only small amplitude at rapid timescales. Measurements of cyclotron lines in some of these systems indicate that the

magnetic field is much lower, with $B \cong 10^4$ T, than in the case of an HMXB containing a neutron star. These features indicate that the compact object in these LMXBs is an older neutron star.

So far, we have focused our discussion on x-ray binary systems that have limited transient behavior. These systems can be observed at almost any time, though their intensity fluctuates. Some transient x-ray objects have a dramatically different character, and there are observations of a number of transient BHC systems of this type. They lie dormant, essentially unobservable for long periods, and then explode into activity with intensities that far exceed the brightest steady state x-ray sources. Figure 22 shows³² recent observations of four such LMXB sources, where the flux is plotted in crab units of intensity vs. time in days after outburst. It should be noted that one crab unit in the HEAO A-1 catalogue corresponds to about 4 counts/sec/cm² for 1–30 keV. Note that the sources initially decay with time exponentially with about the same exponent. This regularity is not well understood and is not seen by BATSE³³ for $E_\gamma > 30$ keV. (The BATSE experiment is described in Sec. 5.) Note that some of the sources show secondary maxima.

Depending on the transient source, these explosive episodes can last long enough that spectroscopic measurements (in visible wavelengths) can be made and mass solutions for the system obtained. Figure 13 shows solutions for two systems in Fig. 22, A0620-00 and V404 Cyg, both spectacular BHC systems. Some of these systems also show what appears to be a strong e^+e^- annihilation line. Figure 23 shows high-energy x-ray spectra for three transient systems. These spectra show structure that can be interpreted as an e^+e^- annihilation line that is redshifted by about $z = 0.07$. The dotted line in the figure corresponds to 511 keV, while all the observed lines have their peaks at about 480 keV. What this might mean as a signature of BHC systems has yet to be sorted out.

Figure 24 shows another interesting spectral behavior for two of these transient BHC systems, (a) GS 2023 + 33 and (b) Nova Muscae. These data show the time evolution of the x-ray spectra. In part (a) of the figure, flickering is observed in the low state of GS 2023 + 33, when the effect of absorption is small. Note that the single power law slope is insensitive to the intensity. Part (b) of the figure shows a transition between the high and low state of Nova Muscae.

Returning to our discussion of the general characteristics of BHC x-ray binary systems,³¹ Fig. 25 shows examples of ultrasoft x-ray energy spectra accompanied by a hard power law tail. These ultrasoft spectra correspond to the high state of the BHC systems. In a few cases where

these data are available, the figure shows the single-power law and low-state spectra in addition to the ultrasoft, high-state spectra. In some cases, good mass solutions have been obtained, and these are also enumerated in the figure. There are no mass solutions for the other systems, and these systems are considered as serious BHC's solely due to the characteristics of their energy and timing spectra. Figure 26 shows more of this approach for the sources GX 339-4 and GS1826-24 where no mass solutions exist. The figure compares energy and timing spectra in the low state of these systems with Cyg X-1, GS 2023 + 33, and GS 1124-68 (Nova Muscae), BHC's where good mass solutions exist. The striking similarity of these spectra is evident. The power law in the energy spectra is closely the same in all cases, and all systems show similar power spectra (PSD) from the 100 sec to the 10 msec timescale. Unfortunately, shorter timescale data do not currently exist for many of these systems (more on this later.) Appendix B gives a table of BHC's based on mass function, and x-ray timing and spectral evidence.

The single-power law energy spectrum observed in the low state of BHC systems may be a general signature, independent of the mass of the candidate black hole. Table 3 shows the single power law slope of both stellar mass and AGN BHC's. The high-state, high-energy single power law was extracted by fitting a single power law and an ultrasoft spectrum to the total spectrum.

The following remarkable regularities follow from the table and other information:

- For both AGN and stellar x-ray binary BHC's, the slope of the power law is distributed within the same range.
- The power law extends to 100 keV and beyond.
- The power law component of the spectrum shows large and irregular temporal changes; however, the power law slope for each individual source remains stable against large changes in intensity.
- Flickering in intensity occurs on timescales which are scaled to the mass of the central object.

Source Name	Low State Single Power Law Exponent	High State High-Energy Power Law Exponent
Cyg X-1	1.5-1.7	
GS 2023+33	1.4-1.7	
GS 1826-24	~ 1.7	
GX 339-4	~ 1.6	~ 2.5
GS 2000+25	~ 1.6	2.0-2.3
GS/GRS1124-6	1.6-1.7	~ 2.5
LMC X-3		~ 2.2

GS 1354-64		~ 2.3
AGNs	1.3-2.3,	average ~ 1.7

Table 3. Minus the power law slope for the low and high states of x-ray binary and AGN BHC's.

These similarities suggest that the power law component is produced by the same mechanism for both classes of BHC sources. Note that the ultrasoft component for AGN's appears in much longer wavelengths than the x-ray band (UV band). Thus, only the single-power law component will be visible in x-rays, whichever state an AGN might take. This could explain the larger range of single-power law exponents for AGN in Table 3.

4b. Future X-Ray Missions

Within the next two years, two new x-ray timing missions will be launched. These are the X-Ray Timing Explorer, XTE, to be launched in the Fall of 1995, and the Unconventional Stellar Aspect experiment, USA, to be launched about one year later. These experiments both bring about two to three orders of magnitude improvement in timing resolution, to the μ sec level. The experimental features of USA and XTE are somewhat complementary, as are their planned observation programs:

- Both have a large detector area, with the counting rate on the Crab pulsar being about 10 kHz for both experiments. USA emphasizes low energy x-rays with $1 < E_\gamma < 30$ keV, while XTE starts somewhat higher at about 2 keV and has acceptance to 200 keV.
- Both have a field of view of about 1° (FWHM) collimated, energy resolution $\Delta E/E \sim 15\%$, and time resolution of 1 μ sec.
- USA has an average data rate, which can be transmitted to the ground, of 40 kbits/sec for 60% of the mission time or 128 kbits/sec for a maximum of five hours per day. XTE rates are a time-averaged rate of 21 kbits/sec or 256 kbits/sec for a maximum of about 30 minutes per day. These data transmission rates are unprecedented for x-ray timing missions.
- USA has a mission lifetime of ≥ 3 years, concentrating observations on the 30–40 brightest x-ray sources. XTE has a mission lifetime of ≥ 2 years in a standard NASA guest observer mode.

Future observations with USA and XTE should greatly expand our knowledge of BHC and neutron x-ray binary systems:

- USA will have weeks of μsec timing data at a rate of 128 kbit/sec on CYG-X-1 and other BHC systems, as compared to minutes from HEAO A-1. XTE should also greatly expand the μsec level timing data on these systems.
- Both experiments will have $\leq 4 \mu\text{sec}$ time resolution in this mode, corresponding to $\leq 1 \text{ km}$ spatial resolution ($\Delta x \sim c\Delta t$). They will also typically have energy information on each photon, allowing a time-energy correlation to be made.
- A surface outside the horizon radius of a BHC may indicate a new state of matter. USA and XTE have the timing resolution to see the power increase expected at these frequencies ($\Delta t \sim 2R_{\text{surface}}/c$), if such a surface exists. For true black holes, no power increase is expected for frequencies higher than those produced in the accretion disk, and disk frequencies should be cut off by the diameter of its inner edge ($\sim 6 R^{\text{sch}}$).

More detailed information on each experiment is given in the following sections.

(i) The Unconventional Stellar Aspect Experiment—USA

Figure 27 shows an artist's conception of the USA detector mounted on the rear of the ARGOS satellite. USA is one of four scientific experiments on the satellite and has been in preparation for about five years. The other three are ultraviolet experiments. ARGOS is scheduled to be launched by the Air Force in the Fall of 1996. A full view of USA is depicted in the figure. The inset shows John Hanson, Aero-Astro/SLAC graduate student, sitting in his creation—the support structure and yoke for USA. Figure 28 gives an overview of the ARGOS satellite.

USA is a collaboration of the Naval Research Laboratory and Stanford University (Physics Department and SLAC) scientists, with representation also from NASA-Ames, Saddleback College, Sonoma State University, the University of Calgary, the University of Oregon, and the University of Washington. It is designed to make long, pointed observations of selected sources, with emphasis on lower x-ray energies than XTE. USA's 1–30 keV energy range extends that of XTE toward low energies where, for many sources, the counting rates are considerably larger. The scientific goals of USA include many of the same as for XTE, but USA will be used in an observation mode that dedicates large amounts of observing time (i.e., many weeks of observing time over a three-year period) to each of 30–40 astronomical objects of particular scientific interest to the collaboration. These measurements should engender a much greater depth of understanding of these BHC and neutron star accretion systems compared to

current measurements. USA's observing mode is scientifically complementary to the planned functioning of XTE as a general purpose x-ray timing observatory, to be used by guest investigators in a great variety of observing programs, each of short duration. For more details about USA, see the World Wide Web at URL:

http://www.slac.stanford.edu/group_k

or contact the USA Principal Investigator Kent Wood, or SLAC Co-Investigator Elliott Bloom at these respective Internet addresses: wood@ssd0.nrl.navy.mil, and elliott@slac.stanford.edu.

The USA x-ray detector system consists of two multiwire proportional chambers, side by side, shadowed by copper hexel collimators that define a 1.2° cone on the sky (FWHM). The chambers are filled with P10 gas at 1.1 ATM, with enough gas stored for a three-to-six year lifetime. A unique feature of this chamber is a $2.5 \mu\text{m}$ mylar window. Such very thin windows have been flown successfully by the NRL x-ray group in a number of past missions. This window, together with the $2.5 \mu\text{m}$ aluminized mylar heat shield, is thin enough to allow measurement of x-rays down to 1 keV. The energy acceptance of the detector is 1–30 keV. The effective aperture of both chambers through the collimators is 2000 cm^2 at 3 keV. The system has an energy resolution of $\Delta E/E = 17\%$, which is about 1 keV at 5.9 keV. In order to reject charge particle backgrounds, the chamber has a built-in anticoincidence system. This five-sided cosmic-ray veto gives a residual rate of $4 \times 10^{-3} \text{ counts/cm}^2/\text{sec}$ at 1–10 keV.

The USA experiment is unique among all x-ray experiments, including XTE, in that it is integrated with a GPS receiver on board the ARGOS spacecraft. This will allow absolute timing to the microsecond level over long periods of time. The GPS timing signal combined with the μsec capability of the USA experiment will result in unprecedented microsecond timing information for an x-ray experiment.

(ii) The X-Ray Timing Explorer—XTE³³

Figure 29 shows a schematic of the XTE. This satellite contains three experiments that are dedicated to x-ray timing and has been in preparation by NASA for about 15 years. The three instruments on the observatory are the proportional counter array, PCA, the high-energy x-ray timing experiment, HEXTE, and the all-sky monitor, ASM. XTE is due to be launched into low earth orbit in late 1995. The instruments on XTE are a collaboration of the NASA Goddard

Space Flight Center, Massachusetts Institute of Technology, and the University of California at San Diego. It will make pointed observations with both the PCA and HEXTE, and scanning observations with the smaller ASM. The pointed observations will be selected by NASA peer review from proposals submitted in response to a NASA Research Announcement.

XTE will have the following scheduling features for scientific reasons. Sources more than 30° off the ecliptic can be observed at any time. Time-constrained observations will be supported, e.g., in order to observe objects at specific epochs, to allow participation in collaborative multiwavelength observations, and for repeated observations. There will be provisions to monitor given sets of objects, such as AGN, or x-ray binaries, with short observations. Transients will be observable with the pointed detectors within seven hours of detection by the ASM or notification from another observatory.

The studies to be carried out by XTE include the nature of black holes (including those that may be in AGN), neutron stars, and white dwarfs—their interactions with their environs, the systems in which they are formed, and their ultimate fates. The objectives will include, where appropriate, the interior composition and properties, and relationships between magnetic and rotation axes. Of special interest are radiation generation mechanisms, disk and wind instabilities, x-ray transients, the end points of binary system evolution, and the formation of the x-ray background due to cosmologically distributed AGN. For more details about XTE, see the World Wide Web at this URL:

<http://heasarc.gsfc.nasa.gov/0/docs/xte/xte.html>

or contact the Principal Investigator Jean Swank at this Internet address:

swank@lheavx.gsfc.nasa.gov.

The PCA and HEXTE are designed to take pointed observations. The PCA measures x-rays in the 2–60 keV region and has an exceptionally large effective collecting area of 6250 cm^2 . The energy resolution is 18% at 6 keV. It consists of five separate gas-filled multiwire proportional chambers, each with a collimator and a sun shade. The detectors are sealed with Xenon gas which gives them acceptance to 60 keV. The background is kept very low by means of anticoincidence chambers on four sides of the detection chamber. The HEXTE system is

sensitive to 20–200 keV x-rays. There are two “rocking” clusters, each with 4 NaI/CsI “phoswich” detectors. A single phoswich detector consists of a 3 mm thick NaI primary detector coupled to a 38 mm thick CsI anticoincidence crystal that also serves as a light guide to the photomultiplier tube. These lie inside a five-sided plastic scintillator anticoincidence shield. Each detector has 200 cm² net effective area. Each cluster contains four detectors; the total net area of the entire system is 1600 cm². The field of view is 1° FWHM and is coaligned with the PCA.

The third XTE instrument is the ASM. This device scans 80% of the sky every ~100 minutes to monitor the intensity of the brightest ~ 75 x-ray sources and to provide an alert if a source changes state or brightens suddenly. This allows the spacecraft to be maneuvered so the PCA/HEXTE systems can study the event. The ASM consists of three scanning shadow cameras on one rotating boom with a total effective area of 90 cm². Each device is a “Dicke camera” consisting of a one-dimensional mask and a one-dimensional position-sensitive proportional counter. The gross field of view of a single camera is 6° × 90° FWHM, and the angular resolution in the imaging direction is 0.2°. The intensities and other basic results derived from the ASM data will immediately be made available in the XTE science operations center and to the community in general via computer links. With its combination of instruments and broad user community, XTE should bring rapid progress to many subfields of x-ray timing astronomy and astrophysics (and particle astrophysics).

In summary, Fig. 30 shows the effective x-ray acceptance vs. energy of past, current, and future x-ray satellite detectors for 1–200 keV. The acceptance of USA is shown as dots, while the XTE PCA is the top solid line in the figure. The XTE HEXTE effective acceptance, taking into account routine off-target background scans, is shown as the top dashed line starting at about 20 keV. XTE will make a dramatic increase in effective area compared to past experiments over much of the energy range shown. USA will have an increased effective area below 2 keV, compared to past timing experiments, due to its ultrathin mylar window.

5. Gamma-Ray Astrophysics

With the launch of the Compton Gamma-Ray Observatory (CGRO) by NASA in early 1991, a dramatic influx of new gamma-ray data in the 0.5 MeV–30 GeV energy range became available to investigators. The CGRO³⁴ consists of four experiments. The Burst and Transient Source Experiment (BATSE) studies short-lived phenomena, such as gamma-ray bursts. The Oriented Scintillation Spectrometer Experiment (OSSE) measures the low-energy gamma-ray spectrum of

celestial objects, in particular, higher energy x-ray and lower energy gamma-ray lines from atoms and nuclei. The Imaging Compton Telescope (COMPTEL) measures gamma-rays in the MeV to tens of MeV range, with an emphasis on higher energy nuclear lines. Finally, the Energetic Gamma-Ray Experiment Telescope (EGRET) is the highest energy gamma-ray instrument measuring γ 's in the 50 MeV–30 GeV range. In this section, we will concentrate on the results of BATSE and EGRET. Both of these instruments have made contributions that are of considerable interest to particle physics.

5a. Gamma-Ray Bursters

Gamma-ray bursts are intense transient bursts of γ 's with spectral contribution from the x-ray region to about 20 GeV (the highest energy burst photon yet observed by the EGRET experiment).³⁵ These bursts have a complicated temporal structure and have been observed to have durations from less than 0.1 sec to more than 500 sec. They were first discovered by the American, classified, VELA satellites that were placed in orbit to detect clandestine nuclear explosions above the surface of the earth. The startling discovery of naturally occurring gamma-ray bursts over the celestial sphere took a number of years to be made public due to classification issues.

Figure 31, adapted from G. Fishman,³⁶ indicates that the development of theories of gamma-ray bursts is based upon relatively little data which, in turn, have been controversial. BATSE has broadened the observational base considerably over the past four years with much reliable data. This data flow should continue for the life of the CGRO satellite. Indeed, pre-BATSE, over 100 theoretical papers were published speculating on the nature of these phenomena. Since BATSE has begun, more than 50 additional theoretical papers have addressed this issue.³⁷ In the past, the theories, in the large, were concerned with neutron star models of gamma-ray bursts. However, the uniformity of these bursts on the sky, which we shall discuss in some detail, has made it very difficult for the neutron star source models. This is because neutron stars are thought to be a product of the death of stars that are congregated in the plane of the galaxy. Thus, one would expect to see the influence of the galactic plane in the distribution of bursters on the sky. None is observed by BATSE, which has placed new emphasis on cosmological models of gamma-ray bursts.

- The pre-BATSE theoretical near consensus that bursts were galactic, originating from a neutron star population having a strong magnetic field, was based on the following observational information:
- Millisecond fluctuations in the burst intensity indicated a compact object consistent with a neutron star.
- Observation of spectral lines in the 20 keV–66 keV range by the GINGA satellite³⁸ are interpreted as cyclotron lines corresponding to a 10^8 T magnetic field, which is consistent with a neutron star. (To this date, OSSE has not confirmed these observations.)
- There are no quiescent counterpart sources to bursts that have been observed. This is compatible with the burst source being an isolated compact object.
- In some bursts, soft x-ray tails can be fit by a blackbody spectra with $T \approx 3$ keV. This implies through model calculations a source radius, $R = 0.7 (d/1 \text{ kpc}) \text{ km}$. Such a source structure is consistent with the polar region of a neutron star for bursters with $d < 10 \text{ kpc}$, i.e., galactic sources.

These pre-BATSE (and OSSE) experimental results led to many, many models for bursters based on a galactic population of isolated neutron stars. One unavoidable prediction from these models was that detectors of increased sensitivity should see an anisotropy in the burster distribution on the sky towards the galactic plane. BATSE, which has now collected well over 1500 bursts, has not observed this predicted anisotropy to levels that make galactic models of bursters highly unlikely.

BATSE³⁹ consists of eight identically configured detector modules and a Central Electronics Unit (CEU). Each detector module contains two NaI(Tl) scintillation detectors: a Large Area Detector (LAD) optimized for sensitivity and directional response, and a Spectroscopy Detector (SD) optimized for energy coverage and energy resolution. The eight planes of the LADs are parallel to the eight faces of a regular octahedron, with the orthogonal primary axes of the octahedron aligned with the coordinate axes of the CGRO spacecraft. The detectors are mounted to the eight corners of the spacecraft.

The LAD detector is a disk of NaI scintillation crystal 20 inches in diameter and 0.5-inch thick, mounted on a 0.75-inch layer of quartz. The large diameter-to-thickness ratio of the scintillation crystal produces a detector response similar to that of a cosine function at low

energies where the crystal is opaque to incident radiation. At energies above 300 keV, the angular response is flatter than a cosine. A light collector housing on each detector brings the scintillation light into three five-inch-diameter photomultiplier tubes. The signals from the three tubes are summed at the detector. A 0.25-inch plastic scintillation detector in front of the LAD is used as an anticoincidence shield to reduce the background due to charged particles. A thin lead and tin shield inside the light collector housing reduces the amount of background and scattered radiation entering the back side.

The spectroscopy detector is an uncollimated NaI(Tl) scintillation detector five inches in diameter and three inches thick. A single five-inch photomultiplier tube is directly coupled to the scintillation detector window. The housing of the PMT has a passive lead/tin shield similar to that of the LADs. The crystal housing has a three-inch-diameter, 50 mm thick beryllium window on its front face in order to provide high efficiency down to 10 keV. The axis of symmetry of an SD is offset by 19° from the LAD axis for mechanical reasons.

Scintillation pulses from the detectors are processed by a gated baseline restoration circuit in order to minimize spectral distortion at high counting rates. Pulses are processed in parallel by a high-speed, four-channel discriminator circuit and by a slower, pulse-height analyzer system. The nominal equivalent energies of the upper three discriminators for the LADs are 60, 110, and 325 keV. The lower-level discriminators are programmable and currently set near 20 keV. Two of the fast discriminators for the SD's are set at energies above the energies analyzed by the pulse height system. The gain of each detector system is determined by the high voltage applied to the PMT's. The SD's are operated at three different gains in order to span from 10 keV to greater than 100 MeV.

Each of the eight BATSE detector modules sends data to the Central Electronics Unit (CEU). The CEU contains hardware and software that accumulates the data into several large RAM memory buffers. Extensive use of commandable parameters, plus the capability to reprogram the flight software, ensures that BATSE has the flexibility to respond to unforeseen conditions or newly discovered gamma-ray phenomena. Signals from the pulse-height converters are used to construct 128-channel spectra from the LAD's and 256-channel spectra from the SD's. Each of the spectra are subdivided into ranges with different dispersions to increase the dynamic range and to efficiently use the available telemetry space. These energy channels are also mapped into 16 coarse energy channels using programmable look-up tables, one for the LAD's and one for the SD's. This permits the trade of time resolution for energy

resolution in several of the data types. Discriminator events are accumulated in the hardware every 64 ms. The CEU hardware constructs various data types from the discriminator counts, and the 16-channel, 128-channel, and 256-channel count spectra.

BATSE detects gamma-ray bursts on-board by examining the count rates of each of the eight LAD's for statistically significant increases above background on each of the three timescales: 64 ms, 256 ms, and 1024 ms. The discriminator rates in channels 2 and 3 (approximately 55–325 keV) are used. The background rate is determined for each detector over a commandable time interval currently set at 17.4 seconds. The statistical significance required for a burst trigger is set separately for each of the three timescales, with a quantization of 0.0625 sigma. These thresholds are currently set at 5.5 sigma. At least two detectors must exceed threshold for a burst trigger to occur. An additional requirement for burst triggering is that the detector with the greatest increase in count rate must have an increase in the charged particle rate that is less than a specified fraction of the increase in the neutral rate. This is done in order to avoid triggering on charged-particle event encounters, such as those produced by spacecraft containing nuclear reactor power sources.

When a gamma-ray burst is detected, the CEU enters a fast data acquisition mode and rapidly stores a variety of data types into memory. Over the period of a CGRO orbit, the normally scheduled output of pulsar and high resolution spectra is suspended, and the collected burst data is read out in the variable portion of the data packets. The normal output schedule then resumes, in proper synchronization with the CGRO orbit. While the burst memories are being telemetered, the trigger thresholds are temporarily revised to values corresponding to the maximum rates detected during the burst. Thus, a stronger burst will terminate the readout of a weaker burst and overwrite the burst memories. The data available from an overwritten burst is timing dependent but includes, at a minimum, the 64-ms-resolution discriminator data (DISCSC).

The error in angular location⁴⁰ of burst events is the radius of a circle having the same area as the 68% confidence ellipse defined by the formal covariance matrix from a minimum χ^2 fit on the assumption of normal errors. The error is based solely on the Poisson uncertainty in the BATSE measurement of burst flux by each LAD. There is, in addition, an RMS systematic error of approximately four degrees. Adding four degrees in quadrature to the error from the fit yields an estimate of the 68% confidence interval for the burst location error. One does not expect a normal distribution of errors, particularly when a burst is weak (and the error in the

basic measurement is large). The 95% confidence interval may be three to four times the size of the 68% confidence interval.

Figure 32 shows the duration distribution for 222 BATSE bursts⁴¹ as measured by T_{90} , where T_{90} is the time interval during which the integrated counts go from 5% to 95% of the total integrated counts in the burst. The solid histogram is the raw data, while the dashed histogram, essentially the same as the solid histogram, is the raw data convolved with measurement errors. The data seem to show a bimodal distribution with one “peak” at about 0.3 sec and the other at about 35 secs.

Figure 33 shows some “typical” burst profiles of counts per second vs. time during the burst; these are called *light curves*. Two distinct types of bursts appear in the figure. Parts (a)–(d) show four typical *multipeaked complex* light curves, while (e)–(h) show four typical *smooth* light curves. For all parts of the figure, the energy range of photons in the light curve is 50–300 keV.

Figure 34 shows the distribution of the energy of the peak emission per unit logarithmic energy interval for a number of bursts. As the figure shows, there are some bursts that have peak emission in the 1 MeV range. Energy spectra of a burst can also be characterized by an effective power law index, α , i.e., E^α . Figure 35 shows a distribution of the effective power law index for a sample of 222 BATSE bursts measured over the energy range 50–300 keV. The solid line represents the distribution for the peak rate spectrum, and the dotted line represents the distribution for the total fluence spectrum. The effective power law peaks at $\alpha \approx -1.7$, but has a broad distribution which extends to values greater than zero for this energy range.

Of course, the most exciting result to date from the BATSE experiment is the observation of an isotropic distribution of bursts on the celestial sphere.⁴² Figure 36 shows the BATSE burst distribution in galactic coordinates for the first 743 events. As previously discussed in detail, the direction to each burst is determined using the relative count rate on the eight LAD’s, one at each corner of the CGRO spacecraft. The error on the location, σ_θ , is about 13° statistical and 4° systematic. Table 4 lists the values of the statistics for the ensemble of 743 bursts.

Six statistics are used to measure the anisotropy. Two galactic statistics test most sensitively for galactic patterns, and thus, are best for testing the question of galactic vs. cosmological origin. The statistic $\langle \cos\theta \rangle$, where θ is the angle between the burst and the galactic center, tests for a concentration towards the galactic center, while the statistic $\langle \sin^2 b \rangle$

$1/3$ >, where b is the galactic latitude, tests for a concentration in the galactic plane. Two coordinate-system independent statistics⁴³ test for significant dipole and quadrupole moments in a model-independent way. The Rayleigh-Watson statistic, W , tests the size of the dipole moment, while the Bingham statistic, B , measures the deviation of the quadrupole moments from the values expected for isotropy. Finally, two equatorial-based statistics test for the artificial anisotropy caused by the proximity of the Earth to the spacecraft. The statistic $\langle \sin^2 \delta - 1/3 \rangle$, where δ is the declination to the burst, is sensitive to the quadrupole moment caused by the reduced exposure of the equatorial region, and the statistic $\langle \sin \delta \rangle$ is sensitive to the dipole moment towards the North Pole caused by turning the instrument off in the South Atlantic Anomaly.

The direction of a burst is measured by the relative counting rate from each of the eight LAD's during the burst. The error listed in the fourth and fifth columns of Table 4 are the 1σ finite sample fluctuation. This comparison between the next-to-last and the last columns indicates the evidence for isotropy. No evidence for anisotropy is seen in the table. The distribution of bursts is consistent with an isotropic distribution on the sky. The errors are small enough that galactic halo models are also limited. For the extended (neutron star) halo model, the data requires most burst sources to be at least 100 kpc from the galactic center, regardless of the freedom to adjust the form of the radial distribution. In addition, there are essentially no repeater bursts; that is, each source has been seen only once. If these bursts are cosmological in origin, there must be an enormous power in the burst, much greater than typical bursts associated with neutron stars. Such power could arise from the merging of two neutron stars into a black hole. It seems like we have a real mystery on our hands.

5b. Results from High-Energy Gamma-Ray Experiments

High-energy gamma-ray astronomy is a relatively young science with the first experiments being done from space in about 1962, and the first ground-based ultra high-energy experiments (> 0.5 TeV) starting up in the mid-1970s. Table 5 shows a list of orbiting high-energy gamma-ray telescope missions to date and the increasing sensitivity as time has progressed.

Instrument	Year of Launch	Photons Detected
EXP XI	1962	31
OSO-3	1968	621
SAS-2	1972	8,000

COS-B	1975	200,000
EGRET	1991	40,000,000

Table 5. Orbiting high-energy gamma-ray telescope missions.

High-energy gamma rays from space are excellent probes of the most energetic phenomena that occur in nature. They are emitted over a wide range of angular scales from a diverse population of astrophysical sources: stellar mass objects, in particular, neutron stars and BHC; AGN; interstellar gas in the galaxy that interacts with high-energy cosmic rays; the diffuse extragalactic background (the source of which is currently unknown); supernovae that may be sites of cosmic-ray acceleration; and gamma-ray bursts. Many of these sources exhibit transient phenomena.

(i) Spaced Based (Mainly EGRET)

Interest in these areas has received a large boost from the EGRET data. After preparations that lasted more than 25 years, the EGRET gamma-ray telescope was launched on CGRO in early 1991. Figure 37 shows a schematic of the EGRET instrument.⁴⁴ The instrument is essentially an array of spark chambers, read out by magnetic cores, with thin photon converter plates between each layer of the chamber. The chamber system is backed by a NaI(tl) photon calorimeter of about eight radiation lengths. In addition, there is an anticoincidence “dome” and a time-of-flight coincidence system to remove backgrounds. The instrument is about 2 m high and 1.8 m across.

The EGRET instrument⁴⁵ is sensitive to photons in the energy range of 30 MeV–30 GeV. The spatial resolution is energy dependent, with high-energy photons having an error circle as little as half a degree. Source localization of bright sources is possible to within 5–10 arc-minutes. The energy resolution of the instrument is typically of the order of 20%. The effective area is strongly energy dependent but reaches a maximum of 1400 cm² at 500 MeV (250 cm² at 50 MeV, 1200 cm² at 1 GeV, and 700 cm² at 10 GeV). EGRET sees a large field of view in each pointing. Here, the data are generally cut off at 30–40° from the center of the field of view ($\sim 0.2 \times \pi$ sr). The absolute timing accuracy of arrival times of photons is 0.1 ms. The instrumental background is believed to be small compared to the galactic and extragalactic diffuse emission (corresponding to a flux of about 2×10^{-5} photons/cm²/sec.).

EGRET data has produced a large number of interesting results. A sample of these includes:

- The EGRET all-sky map.³⁴ Figure 38 shows this map for $E_\gamma > 100$ MeV in galactic coordinates. Some sources are marked on the figure.
- Pulsed gamma-ray emission above 100 MeV detected from five pulsars⁴⁶ (there are recently results from a sixth pulsar). Figure 39 shows light curves from four pulsars in the radio, optical, x-ray, and gamma-ray. Each pulsar shows a different pattern of emission in the various wavelengths. Geminga is of particular interest in that it has no emission in the radio and optical bands, and is most strongly seen in the x-ray and gamma-ray bands.
- More than 30 sources detected in the galactic plane, including high-energy gamma emission from the galactic center region.⁴⁷
- Diffuse emission detected from the Large Magellanic Cloud.⁴⁸ This observation, along with the nondetection of the Small Magellanic Cloud, directly shows that cosmic rays are not universal but are galactic in origin.
- Gamma-ray emission from more than 40 AGN.⁴⁹ These have variability observed on timescales of days to months. Ground-based observations from 0.5 TeV on up of Mkn 421 (AGN) by the Whipple Observatory have been coordinated with observations by EGRET. Recently, a flare of Mkn 421 was simultaneously observed by ASCA (x-ray), CGRO, and Whipple.
- More than 25 high-galactic-latitude unidentified sources.⁴⁷
- Detection of a solar flare of several hours' duration and emission to at least 2 GeV.⁵⁰
- Several high-energy gamma-ray bursts detected, and emission to at least 18 GeV.³⁵

I find one of the results listed above particularly exciting and bizarre, the extraordinary emissions of AGN, 3C279.⁵¹ Figure 38 shows this AGN in the upper central part of the EGRET all-sky map. EGRET measured the luminosity in γ -rays with $E_\gamma > 100$ MeV to be 5×10^{40} W. This equals the total energy output of 10^{14} Suns (the Milky Way has 10^{11} stars), which also equals the conversion to > 100 MeV gamma energy of nine solar masses per year (assuming beaming of the source into 0.5 steradians). Assuming about a 10% conversion efficiency of mass to energy (probably high), the AGN is consuming ~ 100 solar masses per year and will run out of stars in $\sim 10^9$ years.

EGRET saw a factor of five change in this γ -ray luminosity over two days. This implies the size of the emitting region is less than or equal to about two light days across. This is a volume of about 10^{-6} pc³. The average density of stars in our Milky Way is ~ 10 /pc³. Thus, from

a region in which one expects about ten stars, 10^{14} more power than a typical star, or 1000 times more power than an entire galaxy is emerging in > 100 MeV γ -rays! Could the source of this energy be a supermassive black hole? A 10^9 solar mass black hole is about 20 light hours across. Unfortunately, there is no mass determination for the AGN of the quasar 3C278.

(ii) Ground-Based Gamma-Ray Astronomy

For high γ -ray energy, currently $E_\gamma > 0.5$ TeV, one can observe celestial sources in γ -rays on the surface of the earth using either atmospheric Cherenkov light telescopes or air shower counter arrays. Observed gamma energies extend to 10 TeV for the Cherenkov telescopes, with upper limits for energies as high as a few hundred TeV for the air shower arrays (in principle, larger arrays can go much higher). For an excellent review of this field, see Ref. 52. Signals in high-energy gamma-rays have been seen in earth-based instruments for four sources. These sources are two pulsars and two “nearby” AGN’s, including the Crab pulsar, PSR B1706-44, and the recent Whipple Observatory observation⁵³ of the AGN Mkn 421 at a redshift of $z = 0.03$. It is notable that two of the firmly established TeV sources are pulsars and the third is an AGN, all of which have been detected by EGRET.

Figure 40 shows observations of the unpulsed photon spectrum from the Crab Nebula.⁵⁴ The COMPTEL data are from a Ph. D. thesis.⁵⁵ The EGRET data⁵⁶ and model fits are yet to be published. The superimposed model⁵⁷ provides a reasonable interpretation to all the data. This model assumes a population of relativistic electrons with energies to 3×10^{15} eV. The σ parameter in the figure is the ratio of the magnetic field energy density to the electron energy density. The synchrotron photons emitted by the electrons spiraling in the magnetic field of the nebula have a cut-off near 60 MeV. Photons of higher energy result when these synchrotron radiation photons inverse-Compton scatter off the electrons.

The combination of data from ground-based and space-based high-energy gamma-ray observations offer a unique window on the era of galaxy formation, which began about 10^9 years after the Big Bang. Observations of 20 GeV to TeV-range γ 's from AGN sources at widely different redshifts are needed for such a study. The basic mechanism at work is the $\gamma\gamma$ interaction at high enough CM energy to make e^+e^- pairs; this removes the photon from the “beam.” The photons emitted by AGN are thought to have high enough energy that interaction with the Extragalactic Background Light, EBL, will make pairs.⁵⁸ As recently pointed out,⁵⁹ the dominant

factor influencing the EBL is the epoch of galaxy formation. In modern theories, the galaxy formation epoch depends on the nature of dark matter.

- Cold Dark Matter, CDM (e.g., WIMPs, MACHOs, super symmetric particles) has low velocity and tends to reinforce structure formation via gravity.
- Hot Dark Matter, HDM (e.g., neutrinos with mass, light axions) has a large velocity and tends to wash out structure formation (i.e., delay it).

For interactions of high-energy photons, energy E_γ with the EBL, the $\gamma\gamma \rightarrow e^+e^-$ cross section is maximal for EBL photons with energy, $\epsilon_{EBL} \sim (1 \text{ TeV}/E_\gamma)/3 \text{ eV}$. The EBL energy spectrum is maximal in the range 0.1–10 eV (Ref. 59), which implies that maximal scattering occurs for E_γ in the range $0.030 \text{ TeV} < E_\gamma < 3 \text{ TeV}$. This range of parameters has good sensitivity to galaxy formation for $z < 1$, where z is the redshift of the AGN observed in high-energy γ 's (z determined by other means).

Figure 41 shows Mkn 421 data from EGRET and Whipple, compared with the various EBL models from Ref. 59. Mkn 421 has a $z = 0.031$; the figure also shows a hypothetical source at $z = 0.5$, and how it would be cut off by Model 2 of the EBL (see figure). The Whipple results for Mkn 421 are not well-fit by any of the models. This suggests to the authors of Ref. 59 that an intrinsic cut-off exists at the source at about 3 TeV. If such a cut off exists, it would limit the utility of $z \ll 1$ sources in characterizing the EBL. Higher z sources show a cut-off by the EBL at much lower energy in these theories.

EGRET has observed about ten AGN's with $z < 1$ in GeV γ 's, including Mkn 421. So far, Whipple has only published results on Mkn 421 in the TeV region. Filling in the region between 0.02 TeV–0.5 TeV will dramatically increase the sensitivity for probing the epoch of galaxy formation. Ground-based instruments are hoping to drop their thresholds to the 0.1 TeV region. A much more sensitive space-based instrument than EGRET is needed to probe this interesting energy regime, which is the topic of the next section.

5c. A Future High-Energy Gamma-Ray Mission

Recent results from EGRET have generated strong interest in space based high-energy ($E_\gamma > 10 \text{ MeV}$) gamma-ray astronomy. This science has whetted our curiosity of what might be observed with an instrument having considerably more capability than EGRET, if such a device were practical in our fiscally difficult times.

Advances in silicon technology over the past decade, and the resulting rapid drop in costs, encourage the development of a dramatically new type of high-energy gamma-ray space telescope based on silicon strip technology. The GLAST team⁶⁰ (GLAST stands for Gamma-ray Large Area Space Telescope) has been working for the past three years on the design of such an instrument and on the development of the silicon strip hardware and readout electronics needed to realize our design.⁶¹ Figure 42 shows an artist's concept of our current instrument design, including the spacecraft. As in previous high-energy instruments, GLAST is a pair spectrometer backed by a total absorption electromagnetic shower counter. Measurement of the energy and direction of the induced electromagnetic shower provides information about the energy and direction of the incident gamma-ray. However, due to the flexibility and relatively low cost of the silicon strip technology, the telescope has about a factor of ten increase in effective area over EGRET, and about a factor of five increase in field of view. The size of GLAST is roughly $2 \times 2 \times 0.5$ m. At the same time, the GLAST design is calculated to have much better point source sensitivity and to have an energy range of $10 \text{ MeV} < E_\gamma < 300 \text{ GeV}$. Due to the economies of silicon technology, along with weight and size savings compared to gas-based detector technology, we estimate that this instrument can be built and flown as a Delta II mission. Thus, GLAST would easily fit into the NASA intermediate mission category ($< \$500$ million).

The GLAST design, a practice in modern particle physics detector technology, consists of three elements: (1) a segmented charged particle anticoincidence shield (which could be made from silicon strip detectors or scintillators); (2) a gamma-ray tracker/converter, consisting of ten thin sheets of high-Z converter material (currently 0.05 radiation lengths) interspersed with ten layers of silicon strip detectors for particle tracking, with an additional two layers of silicon strip detectors backing the converter layers to allow good tracking of the photons converted in the last converter layers; and (3) a segmented ten-radiation-length CsI calorimeter to provide good energy resolution at high energies. The GLAST detector is modular (a single GLAST tower is shown by the arrow in Fig. 42), consisting of a 7×7 array of towers, with each tower containing elements of the anticoincidence shield, the tracker/converter stack, and the calorimeter. The single tower shows, along with the tracker/converter, the CsI calorimeter. The design details of the calorimeter, as well as other aspects of the detector, are still in development. The GLAST design has many technical benefits, including no consumables, all relatively low voltages, modularity, essentially deadtimeless operation, modern low cost, and robust and long-lived

technology. It also has its design challenges, including a large channel count of more than 10^6 channels, and on-board computing requirements for the real-time trigger.

Figure 43(a) shows an EGRET all-sky map on which is superimposed the Monte Carlo calculation of the GLAST field of view and the actual EGRET field of view. A dramatic improvement is evident from EGRET to GLAST (Monte Carlo). Figure 43(b) shows the single photon projected angle vs. energy for GLAST (Monte Carlo), EGRET. Figure 43(c) shows the effective area of GLAST (Monte Carlo), EGRET. The flat high-energy acceptance of GLAST, to 300 GeV, is achieved by eliminating the veto of good γ events from their charged particle “backsplash.” This effect is what limits the high-energy acceptance of EGRET due to its monolithic veto “dome.”

As mentioned previously, the Whipple Observatory has cooperated with the CGRO team and others in coordinating space-based and ground-based observations of high-energy gamma rays. The GLAST collaboration hopes to expand this activity to a worldwide scale when GLAST is in orbit. The major mode of GLAST observations will be in the zenith (always pointing out from the earth along the zenith) scanning mode (some pointed observations may also be made). In this mode, GLAST will scan most of the sky many times per day. If a transient of interest should be observed, earth-based observation stations will be contacted very quickly. Figure 44 demonstrates how this might work.⁶² Figure 44(a) shows the GLAST uncorrected point spread function obtained with a $1/E^2$ input photon spectrum for $E_\gamma > 100$ MeV. We assume such an energy dependence for Mkn 421 within the GLAST energy range. As Fig. 44(a) shows, 68% of the photons are contained within about 2.5° (half angle). Figure 44(b) shows a simulated flare of Mkn 421 consistent with past flares. As the figure shows, a 3σ effect for the source flare is seen within one day by GLAST. Figure 44(c) shows the simulated flare spectrum as observed in GLAST. This spectrum includes events from about day 1.5 to day 5. There is useful information in this spectrum to about 10 GeV. If quickly brought on line, the ground-based instruments should be able to obtain useful information from about 100 GeV upwards to a few TeV. Note that an extended observation (e.g., one year in antinadir pointing mode) by GLAST of this source, assuming the source is not flaring during this time, should yield ~ 5 events for $E_\gamma > 100$ GeV, assuming the same $1/E^2$ spectrum as in Fig. 44(c).

6. Conclusions

Figure 45 whimsically illustrates the object of our quest.⁶³ “What is involved is not just the investigation of yet another, even if extremely remarkable, celestial body, but a test of the correctness of our understanding of the properties of space and time in extremely strong gravitational fields.”²

7. Acknowledgments

I would like to thank my graduate students, Andrew Lee and Han Wen, for the massive amount of help they have given me in preparing these lectures. Their work started at the *Summer Study on Particle and Nuclear Astrophysics and Cosmology in the Next Millennium*, June 29-July 14, 1994, Snowmass, Colorado (1995), as scientific secretaries for the G2 working group. They have organized a considerable amount of material that I have used in these lectures. In addition, they have carefully read much of this manuscript and have made valuable comments. I would also like to thank Ms. Linda Lee Evans for a careful reading of this manuscript and many valuable suggestions for improving the presentation. The SLAC graphics art department was really terrific; these lectures would have been impossible without their help. Finally, I thank the SSI Editor, Ms. Lilian DePorcel, for her patience and final editing.

8. Appendices

Appendix A. Introduction to Wavelet Methods⁶⁴

One of the features of the luminosity time series from most x-ray sources, including both the BHC's and neutron star accretion sources such as the low-mass x-ray binaries (LMXBs), is the presence of fluctuations on timescales that span a large range. Indeed, fluctuations are seen from the shortest timescales permitted by the observational time resolution, up to the longest time intervals over which the data are obtained (up to tens of hours of continuous exposure, or the much longer intervals corresponding to the history of x-ray astronomy as an observational science). Hence, we really have limits only on the total extent of the range of timescales. The techniques of *multiresolution analysis*, and especially the special case of *wavelets*, are perfect tools for studying such data, as well as for representing solutions to the physical equations describing the dynamical evolution of the accretion process. This is because a wavelet basis forms a hierarchy of scales, with each scale level differing from its neighbors by factors of two. In particular, given a specific choice for the *mother wavelet* $\psi(t)$, the basis comprises this set of functions

$$\psi_{s,l}(t) = 2^{-\frac{s}{2}} \psi\left(\frac{t}{2^s} - l\right), \quad s = 0, 1, \dots, N-1; \quad l = 0, 2^{s+1}, \dots, (2^N - 2^{s+1}) \quad (\text{A-1})$$

where s is the *scale index*, l is the *location index*, and 2^N is the number of data points analyzed by the wavelet transformations. Note that the width of the function $\psi_{s,l}(t)$ is proportional to 2^s ; in data analysis applications, the scale index s varies over a range of values so that the shortest scale is on the order of the interval between samples, and the longest scale is on the order of the total interval over which the data is sampled. The mother wavelet also satisfies,

$$\int \psi(t) dt = 0, \quad \text{and} \quad \int \psi^2(t) dt = 1. \quad (\text{A-2})$$

Figure A-1 shows an example of a wavelet basis illustrating the s, l indexing, and the *Haar wavelet*. In this case, the *mother wavelet* is given by

$$\psi_{Haar}(t) = \begin{cases} 0, & t < 0 \\ 1, & 0 \leq t < \frac{1}{2} \\ -1, & \frac{1}{2} \leq t < 1 \\ 0, & t > 1 \end{cases} \quad (\text{A-3})$$

The representation of data, or of a function, as a linear superposition of the functions in the wavelet basis, takes the form

$$X(t) = \sum_{s,l} C_{s,l} \psi_{s,l}(t), \quad (\text{A-4})$$

where the

$$C_{s,l} = \langle X(t), \psi_{s,l}(t) \rangle = \int X(t) \psi_{s,l}(t) dt = \sum_{2^M} X_n \psi_{s,l}(n), \quad (\text{A-5})$$

are the wavelet coefficients of $X(t)$ with respect to the wavelets $\psi_{s,l}(t)$. Wavelet coefficients answer the question, “How much does $X(t)$ wiggle at location l and at scale s ?”

There are several key points. First, the wavelets are localized functions. They are nonzero only over a finite subrange of the total time interval over which the observations extend. This allows easy representation of localized features—jumps, discontinuities, or bumps in the data. This should be compared against using Fourier components, where local features require the superposition and delicate cancellation of the completely global basis functions.

Second, the scales of the wavelets extend over the complete range—from the smallest scale (the sampling interval) to the largest (the sample range), and they do so in a convenient time-scale hierarchy in which the levels differ by a factor of two. Wavelets are thus perfect for representing data (or functions) that are *self-similar* (sometimes called *scaling* or *fractal*). This multiscale feature can be achieved in Fourier representations by using a logarithmic frequency scale—but the weighting that wavelets naturally apply to the levels in their dyadic hierarchy often turns out to be more suitable to the signal-to-noise present in the time series data.

Finally, there is a simple relationship between the size of the wavelet coefficients and the smoothness of the function they represent through Eq. (A-4). Basically, if you diminish the absolute value of some of the wavelet coefficients, you are guaranteed that the resulting function $X(t)$ will be smoother than it was. (The relationship between smoothness and the size of the expansion coefficients does not hold in Fourier analysis.) The practical result of this is a cornucopia of denoising and smoothing algorithms based on truncation or “shrinkage” of the wavelet coefficients.⁶⁵ A *denoising* procedure is a way of correcting data for the presence of noise of a known or assumed character. Wavelet denoising methods are particularly good at removing noise without smoothing out edges, bumps, or other localized features in the data.

A simple tool that has proven useful in analyzing stochastic data from x-ray sources⁶⁶ is the wavelet analog of the power spectrum, sometimes called the *scalegram*. If the $C_{s,l}$ are the wavelet coefficients of some discrete data X_n , defined as in Eq. (A-5), then the scalegram of these data is defined to be

$$V^X(s) = \frac{1}{N_s} \sum_l C_{s,l}^2, \quad (\text{A-6})$$

where $N_s = 2^{N-s-l}$ are the number of wavelet coefficients at scale s , and where the l -sum is over the allowed values at scale s .

The scalegram can be easily corrected for the Poisson noise present in x-ray data, as in any photon-counting data. A simple computation shows that the scalegram of time series data subject to an additive normally distributed observational noise of variance σ_R (usually zero in x-ray astronomy), plus Poisson noise (due to the statistics of counting a finite number of photons), satisfies

$$\langle V^{X^{obs}}(s) \rangle = V^{X^{true}}(s) + \sum_{2^N} X_n^{true} H_j(n) + \sigma_R, \quad (\text{A-7})$$

where $H_j(n)$ depends on the wavelet used and is just $1/2^N$ (independent of both n and j) for the Haar wavelet. Also, for most cases, X_n^{true} can be replaced by X_n^{obs} in the second term on the right of Eq. (A-7). Thus, the scalegram of x-ray data can be corrected for counting statistics simply by subtracting the mean count rate (Haar wavelet). Further, the scalegram can be evaluated for time

series data that are arbitrarily spaced in time, including point process data (e.g., for such data as the arrival times of individual photons).

Putting all of these features together, the scalegram and related tools seem to be very well-suited for studying fluctuations of x-ray sources on the shortest possible timescales. This is the kind of information that is needed for the identification and characterization of black hole accretion. A discussion of the use of wavelets to analyze HEAO data on Cygnus X-1 for this very signature can be found in the Snowmass '94, G2 working group proceedings.³³

Appendix B. A Table of Black Hole Candidates⁶⁷

Table B-1 contains a list of BHC that are contained in x-ray binary systems. In cases where a mass determination (Mass Function) for the system has been obtained, it is included in the table. The BHC without mass solutions are based on x-ray spectrum signatures that are discussed in Sec. 4a.

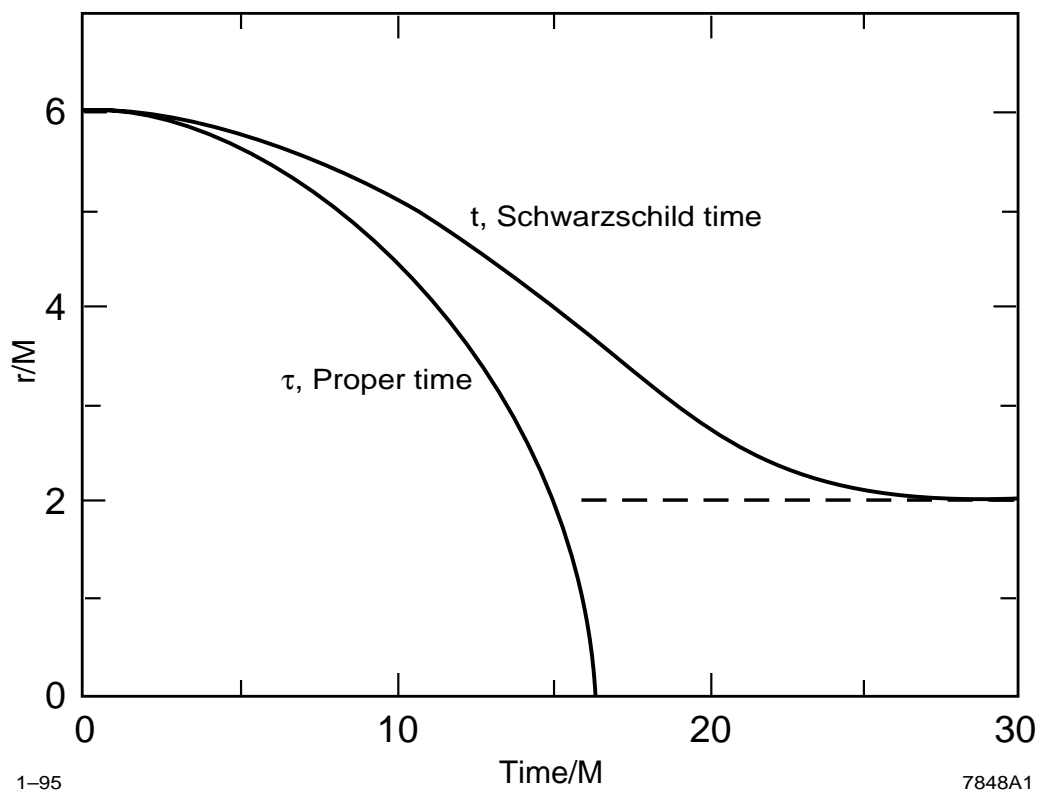
9. References

¹ C. E. Misner, K. S. Thorne, and J. A. Wheeler, *Gravitation* (Freeman, San Francisco, 1973). I refer to this book as MTW.

² I. Novikov, invited plenary talk, to appear in the proceedings of the *Summer Study on Particle and Nuclear Astrophysics and Cosmology in the Next Millennium*, June 29-July 14, 1994—Snowmass, Colorado (1995).

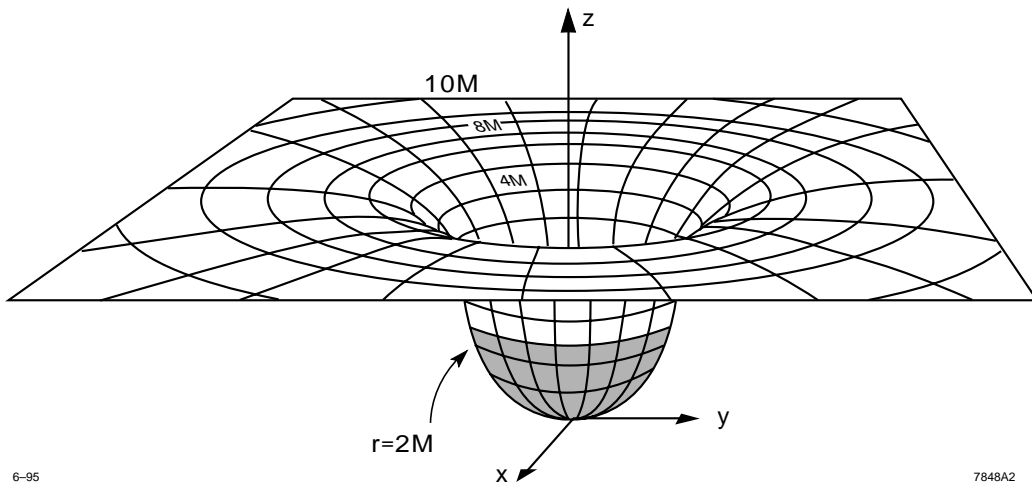
- ³ The gravitational field causes a time dilation and resulting redshift of light. For the Schwarzschild metric, the relationship of ν_{em} (frequency of the emitter) to ν_{rec} (receiver) for a light source at r_{em} that is static relative to a receiver at $r \rightarrow \infty$ is $\nu_{\text{em}}/\nu_{\text{rec}} = (1 - 2M/r_{\text{em}})^{-1/2}$. The redshift is infinite at $r_{\text{em}} = 2M$.
- ⁴ S. L. Shapiro and S. A. Teukolsky, *Black Holes, White Dwarfs, and Neutron Stars--The Physics of Compact Objects* (John Wiley & Sons, New York, 1983). This book is currently a primary source for a student of compact object physics.
- ⁵ Ibid. Chapter 2.2.
- ⁶ Ibid. Chapter 2.3.
- ⁷ Ibid. Chapters 2, 8, and references within.
- ⁸ A good review of the evolution of stars to their final state can be found in *High-Energy Astrophysics, Volume 2*, by M. S. Longair (Cambridge University Press, 1994). For more on stars and their evolution, also see *Universe*, 3rd ed., by W. J. Kaufmann, III, (W. H. Freeman and Co., New York, 1991) Chapters 19-24.
- ⁹ Greenstein *et al.*, *Ap.J.* **149**, p. 283 (1971).
- ¹⁰ For an extensive list of polytrope solutions, see S. Chandrasekhar, *An Introduction to the Study of Stellar Structure*, (University of Chicago Press, Chicago, 1939).
- ¹¹ K. Thorne, *Black Holes and Time Warps: Einstein's Outrageous Legacy* (Picador, England, 1994).
- ¹² W. Baad and F. Zwicky, *Phys. Rev.* **45**, p. 138 (1934).
- ¹³ J. R. Oppenheimer and G. M. Volkoff, *Phys. Rev.* **55**, p. 374 (1939).
- ¹⁴ S. L. Shapiro and S. A. Teukolsky, *Black Holes, White Dwarfs, and Neutron Stars--The Physics of Compact Objects* (John Wiley & Sons, New York, 1983) p. 150.
- ¹⁵ J. Taylor, The Scott Lectures, Cavendish Laboratory (University of Cambridge, 1992); also, see M. S. Longair, *High-Energy Astrophysics*, Vol. 2, (Cambridge University Press, 1994) Figure 15.19, p. 114.
- ¹⁶ C. E. Rhoades and R. Ruffini, *Phys. Rev. Lett.* **32**, p. 324 (1974).
- ¹⁷ G. F. Chapline and M. Nauenberg, *Nature* **264**, p. 267 (1976).
- ¹⁸ For an excellent discussion of this point, see S. Bahcall, B. W. Lynn, and S. B. Selepky, *New Models for Neutron Stars*, SU-ITP-866 (1989).
- ¹⁹ S. Bahcall, B. W. Lynn, and S. B. Selepky, *Nucl. Phys. B* **331**, p. 67 (1990).
- ²⁰ For a review of strange stars, see J. Madsen and P. Hansel, eds., *Strange Quark Matter in Physics and Astrophysics: Proceedings of the International Workshop on Strange Quark Matter in Physics and Astrophysics*, University of Aarhus, Denmark, 20-24 May 1991. Published in *Nucl. Phys. B (Proc. Suppl.)* **24B**, (1991). For much more information about Q-stars, see S. Bahcall, B. W. Lynn, and S. B. Selepky, *Nucl. Phys. B* **325**, p. 606 (1989).
- ²¹ Figures 8(a) and 8(b) were taken from the NASA publication, *X-Ray Timing Explorer--Taking the Pulse of the Universe*, XTE Working Group (1992).
- ²² W. J. Kaufmann, III, *Universe*, 3rd ed., (W. H. Freeman and Co., New York, 1991) Chapter 27.
- ²³ Credit for Fig. 9(a) belongs to National Radio Astronomy Observatory, California Institute of Technology. Credit for Fig. 9(b) belongs to Walter Jaffe/Leiden Observatory, Holland Ford/JHU/STScI, and NASA (1992). I would also like to thank Ann Kinney of the STScI for bringing this figure and considerable accompanying descriptive material to my attention.
- ²⁴ H. Ford *et al.*, *App. J. Lett.* **435**, p. L27 (November 1994).
- ²⁵ R. J. Harms *et al.*, *App J. Lett.* **435**, p. L35 (November 1994).
- ²⁶ M. V. Zombeck, *Handbook of Space Astronomy & Astrophysics*, 2nd ed. (Cambridge University Press, 1990), p. 193.
- ²⁷ S. L. Shapiro and S. A. Teukolsky, *Black Holes, White Dwarfs, and Neutron Stars--The Physics of Compact Objects* (John Wiley & Sons, New York, 1983), p. 339-350.
- ²⁸ J. F. Meekins, K. S. Wood, *et al.*, *Millisecond Variability of Cygnus X-1*, *Ap. J.*, **278**, p. 288 (1984).
- ²⁹ K. S. Wood *et al.*, *The HEAO A-1 X-Ray Source Catalog*, *ApJ Sup* **56**, p. 507 (1984).
- ³⁰ A recent excellent review of the Cyg X-1 binary system can be found in A. P. Crowley, *Ann. Rev. Astron. & Astrophys.*, **30**, p. 287 (1992).
- ³¹ This section is based on two recent reviews of results from x-ray astronomy. Y. Tanaka, *Black Hole X-Ray Binaries*, published in the proceedings of *The Ginga Memorial Symposium: From Ginga to ASTRO-D and Further to DUET (ISAS Symposium on Astrophysics, 1992)*, edited by F. Makino and F. Nagase (1992). The second review is a chapter of a book soon to be published. Y. Tanaka and W. H. G. Lewin, *Black-Hole Binaries*, in *X-Ray Binaries*, edited by W. H. G. Lewin, J. van Paradijs, and E. P. J. van den Heuvel (Cambridge University Press, Cambridge, England, 1995).
- ³² The material on transient x-ray binary sources comes from an invited plenary talk by Craig Wheeler to appear in the proceedings of the *Summer Study on Particle and Nuclear Astrophysics and Cosmology in the Next Millennium*, June 29-July 14, 1994---Snowmass, Colorado (1995).
- ³³ G2 working group report, *Black Hole Astrophysics*, by P. Bender, E. Bloom *et al.*, edited by Jeffrey Scargle, to be published in the proceedings of the *Summer Study on Particle and Nuclear Astrophysics and Cosmology in the Next Millennium*, June 29-July 14, 1994---Snowmass, Colorado (1995). Also see SLAC-PUB-95-6915 (1995).
- ³⁴ For an enlightening review of the CGRO, see N. Gehrels *et al.*, "The Compton Gamma-Ray Observatory," *Scientific American Magazine*, p. 68 (December 1993).

- ³⁵ K. Hurley *et al.*, *Nature* **372**, p. 652 (1994).
- ³⁶ G. J. Fishman, "Gamma-ray bursts: Observational overview," The Second Compton Symposium, *AIP Conference Proceedings* **304**, p. 22 (1994).
- ³⁷ R. J. Nemiroff, "A century of gamma-ray burst models," *AIP Proceedings* **307**, p. 730 (1994).
- ³⁸ T. Murakami *et al.*, *Nature* **335**, p. 234 (1988).
- ³⁹ *Compton Observatory BATSE Second Burst Catalog* (compact disc--CD). Produced by the Compton Observatory Science Support Center at NASA/Goddard Space Flight Center in cooperation with the BATSE Instrument Team, directory **doc/into.txt** (January 1, 1995).
- ⁴⁰ *IBID*, directory **catalog/basic.txt**.
- ⁴¹ C. Meegan *et al.*, *AIP Conference Proceedings* **307**, p. 3 (1994).
- ⁴² M. S. Briggs *et al.*, *AIP Conference Proceedings* **307**, p. 44 (1994).
- ⁴³ M. S. Briggs, *ApJ*, **407**, p. 126 (1993).
- ⁴⁴ G. Kanbach *et al.*, *Space Science Reviews* **46**, p. 69 (1988) for the detailed description of the instrument; and D.J. Thompson, *et al.*, *ApJ.Supp.* **86**, p. 629 (1993) for the instrument calibration.
- ⁴⁵ This brief description of the instrument capabilities was largely taken from *Compton Observatory EGRET All-Sky Survey*, **Vol 1** (compact disc--CD). Produced by the Compton Observatory Science Support Center at NASA/Goddard Space Flight Center, directory **doc/dos/cdrom.tex** (June 1, 1994).
- ⁴⁶ D. J. Thompson *et al.*, *ApJ* **436**, p. 229 (1994).
- ⁴⁷ C. E. Fichtel *et al.*, *ApJS* **94**, p. 551 (1994).
- ⁴⁸ P. Sreekumar *et al.*, *ApJ* **400**, p. L67 (1992).
- ⁴⁹ C. von Montigny *et al.*, *ApJ* **440**, p. 525 (1995).
- ⁵⁰ E. J. Schneid *et al.*, "High-energy solar phenomena--A new era of spacecraft measurements," *AIP Conference Proceedings* **294**, edited by J. M. Ryan and W. T. Bestrand, p. 94 (1994).
- ⁵¹ This particular argument comes from Gary Godfrey, a SLAC colleague.
- ⁵² J. W. Cronin *et al.*, *Annu. Rev. Nucl. Part. Sci.* **43**, p. 883 (1993).
- ⁵³ A. D. Kerrick *et al.*, *ApJ*, **438**, p. L59 (1995).
- ⁵⁴ L. C. Lamb *et al.*, *Ground Based Astronomy*, R2 working group report, *Summer Study on Particle and Nuclear Astrophysics and Cosmology in the Next Millennium*, June 29-July 14, 1994--Snowmass, Colorado, EFI Preprint 96-14, Enrico Fermi Institute, University of Chicago, to appear in the proceedings of the workshop (1995).
- ⁵⁵ R. Much, Ph. D. Thesis, Max Planck Institut für Extraterrestrische Physik.
- ⁵⁶ O. C. De Jager *et al.*, in preparation (1995).
- ⁵⁷ O. C. De Jager and A. K. Harding, *ApJ* **396**, p. 161 (1992).
- ⁵⁸ F. W. Stecker *et al.*, *ApJ* **390**, p. L49 (1992).
- ⁵⁹ D. MacMinn and J. Primack, submitted to *ApJ Lett* (1994).
- ⁶⁰ The GLAST Team currently includes members from the following institutions, in alphabetical order: Enrico Fermi Institute, University of Chicago; Kanagawa University, Japan; Lockheed Research Laboratory, Palo Alto, CA; University of Maryland; Max Planck Institut für Extraterrestrische Physik, Garching, Germany; NASA Ames Research Center, Mountain View, CA; Naval Research Center, Washington DC; University of California at Santa Cruz; Sonoma State University; Stanford University, HEPL, Physics Department, and SLAC; University of Tokyo, Japan; Istituto Nazionale di Fisica Nucleare, Trieste, Italy; University of Washington.
- ⁶¹ For a recent review of the GLAST project, see Elliott D. Bloom, *GLAST*, invited talk presented at the International Heidelberg Workshop on TeV Gamma-Ray Astrophysics, Heidelberg, Germany, October 3-7, 1994. To be published in *Space Science Reviews*. Also see SLAC-PUB-95-6738 (1995).
- ⁶² Bill Atwood (private communication, 1994).
- ⁶³ I. Novikov, *Black Holes and the Universe*, (Cambridge University Press, 1990). (Paperbound. ISBN:0-521-36683-6.)
- ⁶⁴ J. Scargle, much of Sec. 3.2 of Ref. 33 and private communication (1994).
- ⁶⁵ David Donoho and Ian Johnstone of Stanford University have written a number of papers on *wavelet denoising* that are available over the Internet via FTP at *playfair.stanford.edu*; theoretical papers are in the directory **/pub/reports**, abstracts in **/pub/reports/Abstracts**, and a MatLab software package developed with Jeff Scargle in the directory **/pub/software/wavelets**. MatLab is a trademark of The MathWorks, Inc.
- ⁶⁶ J. D. Scargle *et al.*, *ApJ Lett.* **411**, p. L91 (1993).
- ⁶⁷ Y. Tanaka and W. H. G. Lewin, "Black-hole binaries," in *X-Ray Binaries*, edited by W. H. G. Lewin, J. van Paradijs, and E. P. J. van den Heuvel (Cambridge University Press, Cambridge, England, 1995).



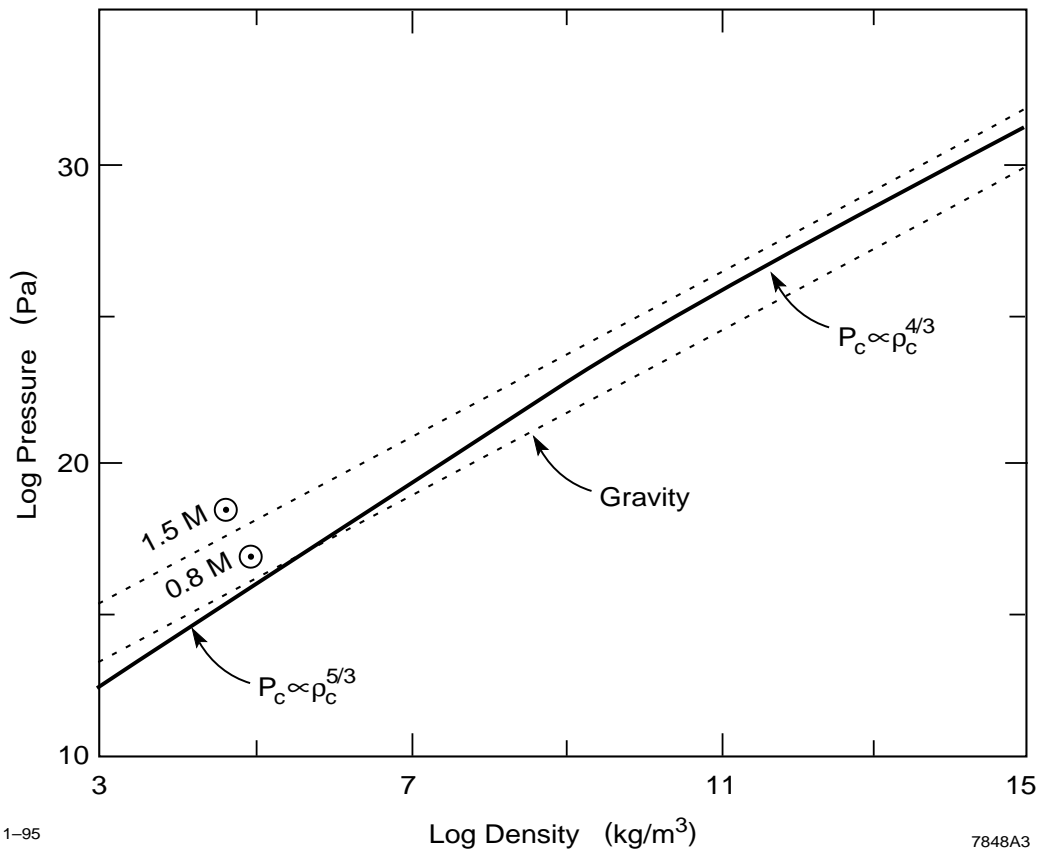
1-95

7848A1



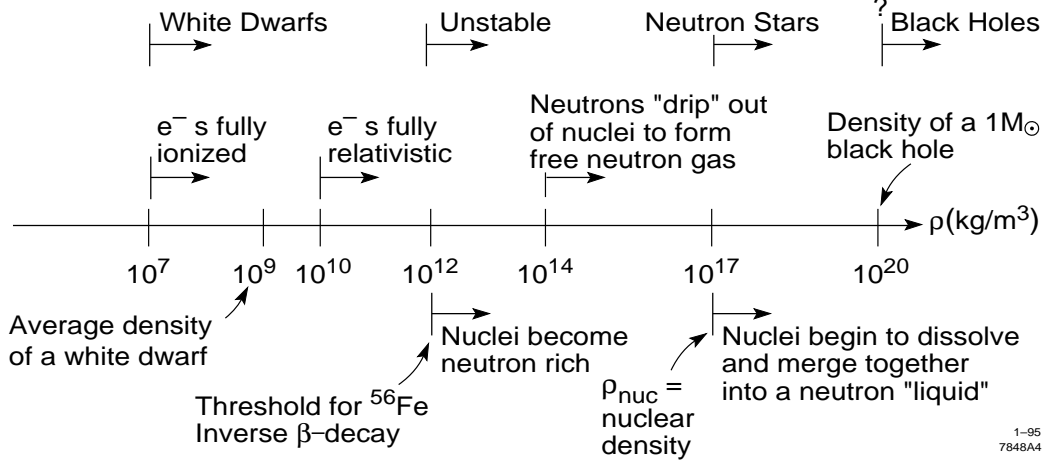
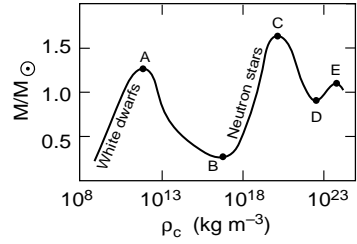
6-95

7848A2

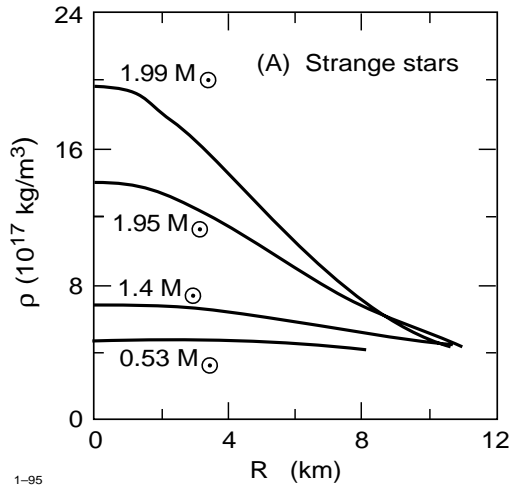


1-95

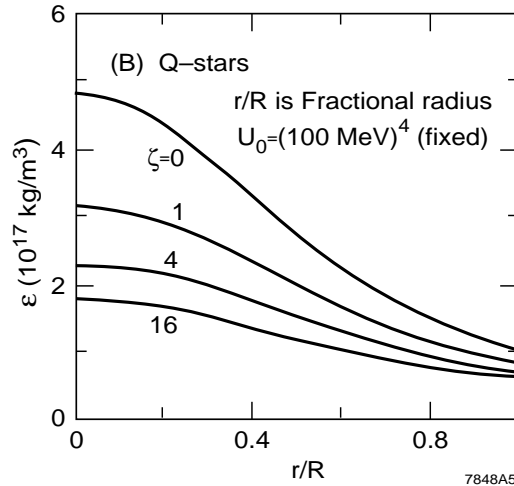
7848A3



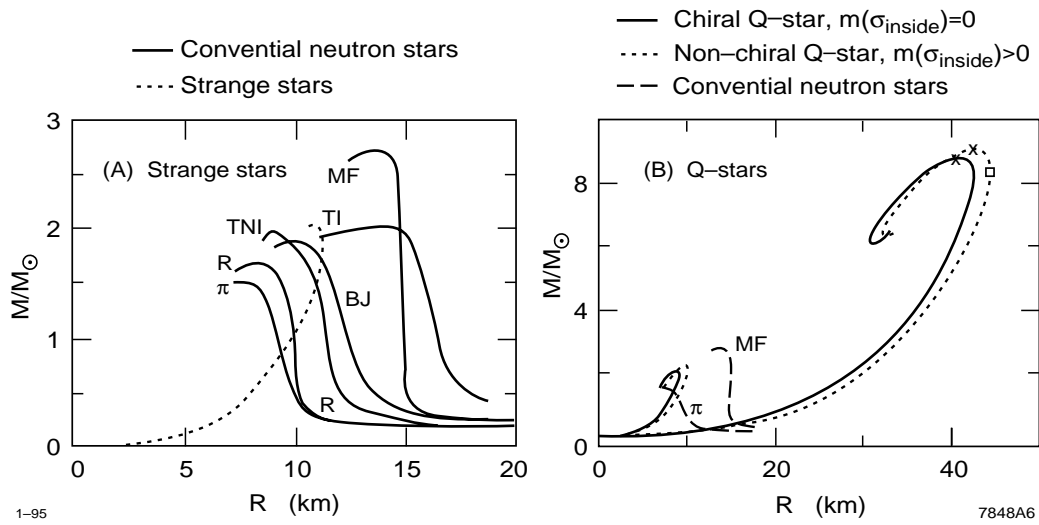
1-95
7848A4

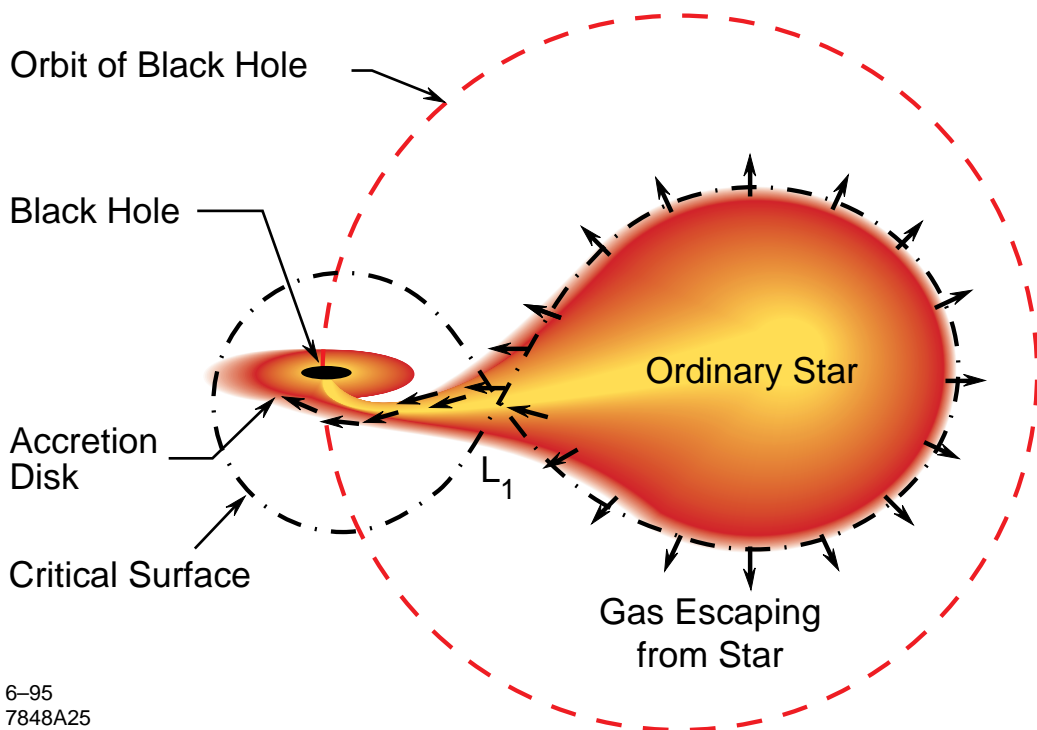


1-95

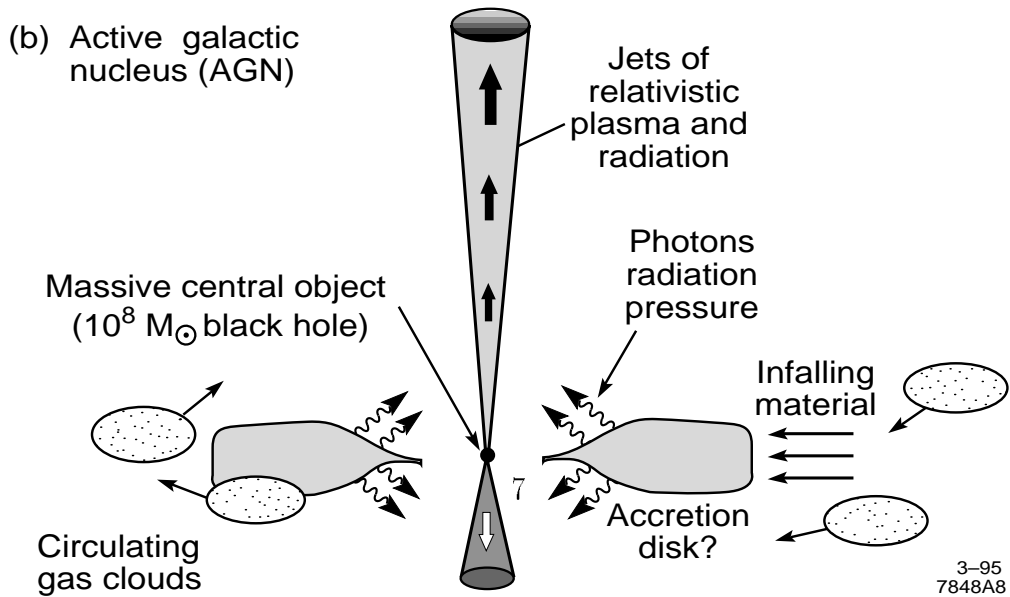
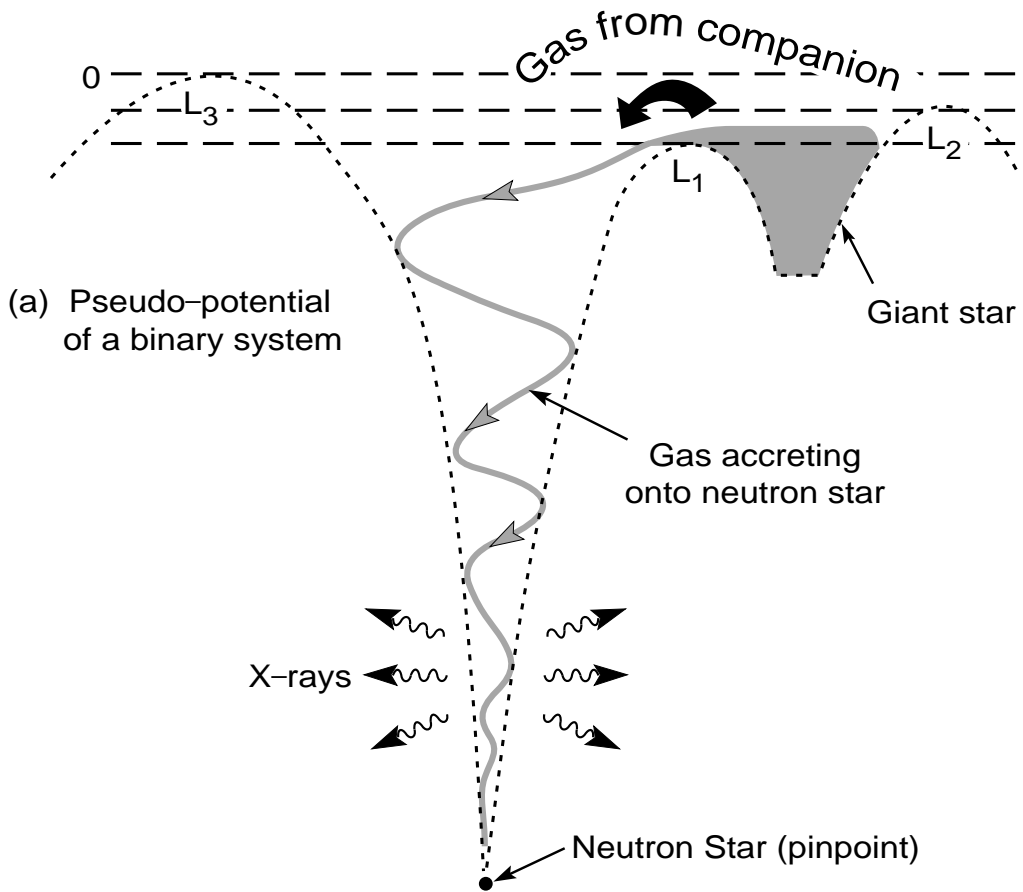


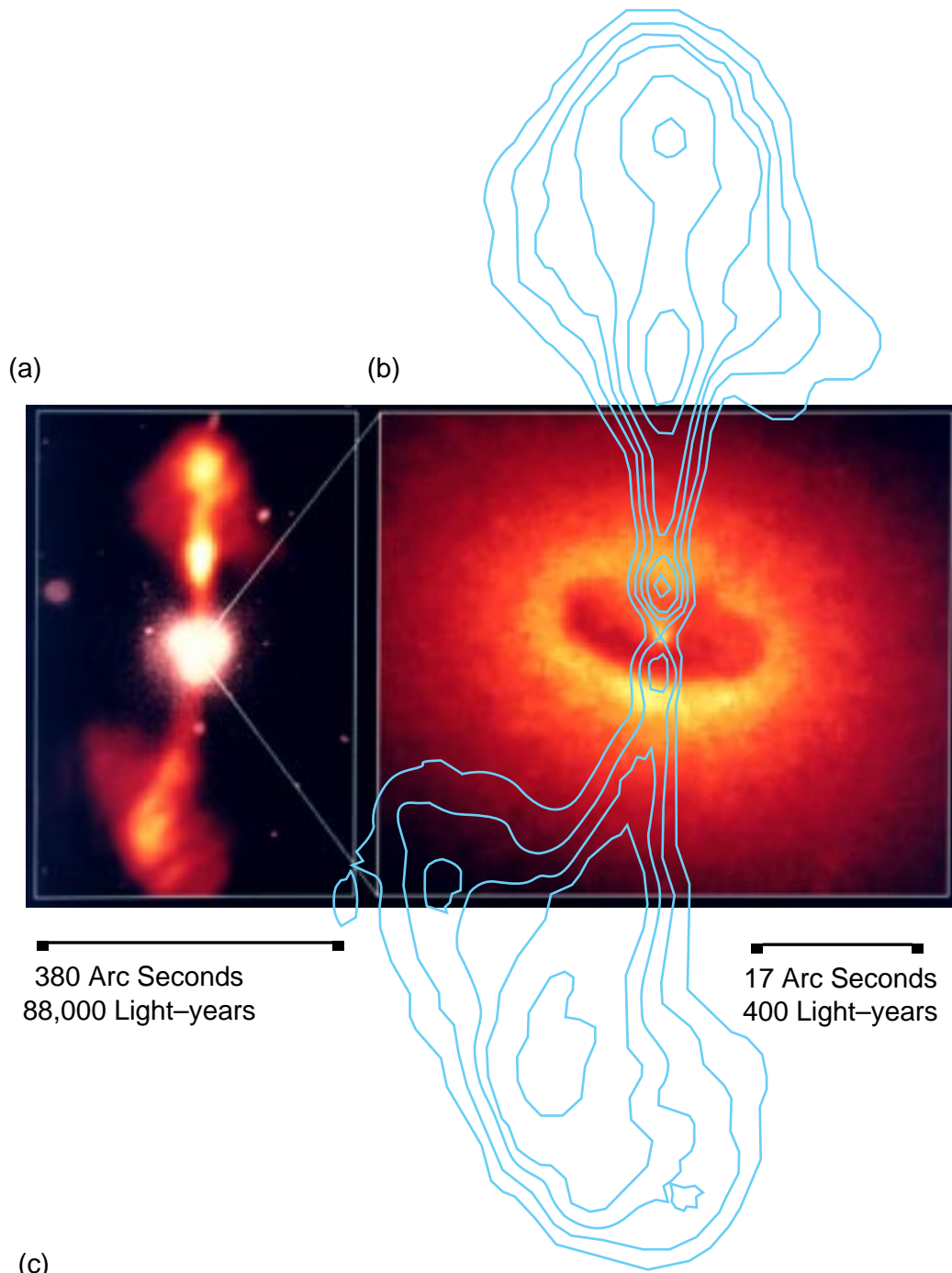
7848A5



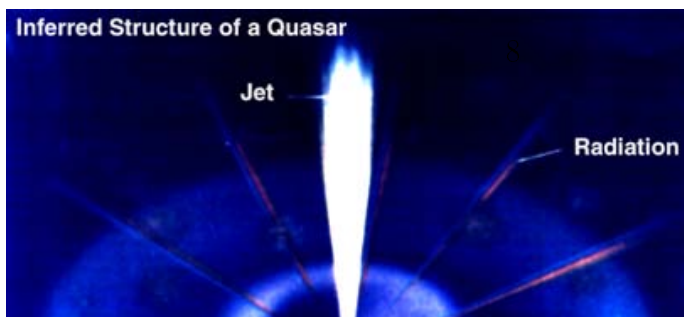


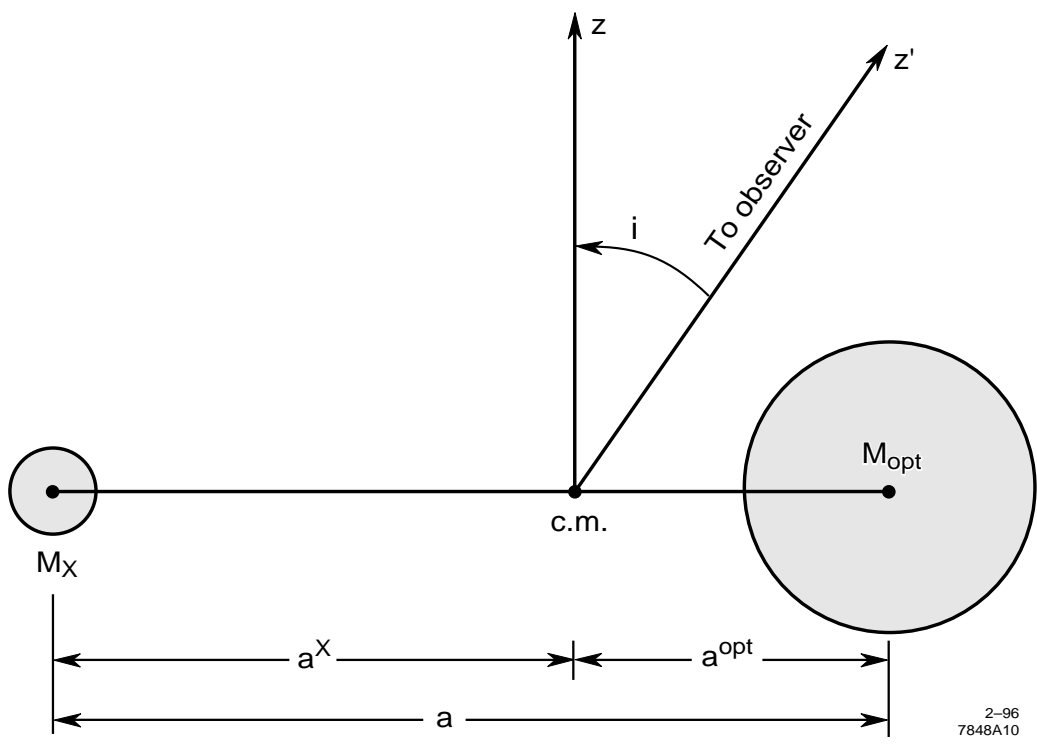
6-95
7848A25



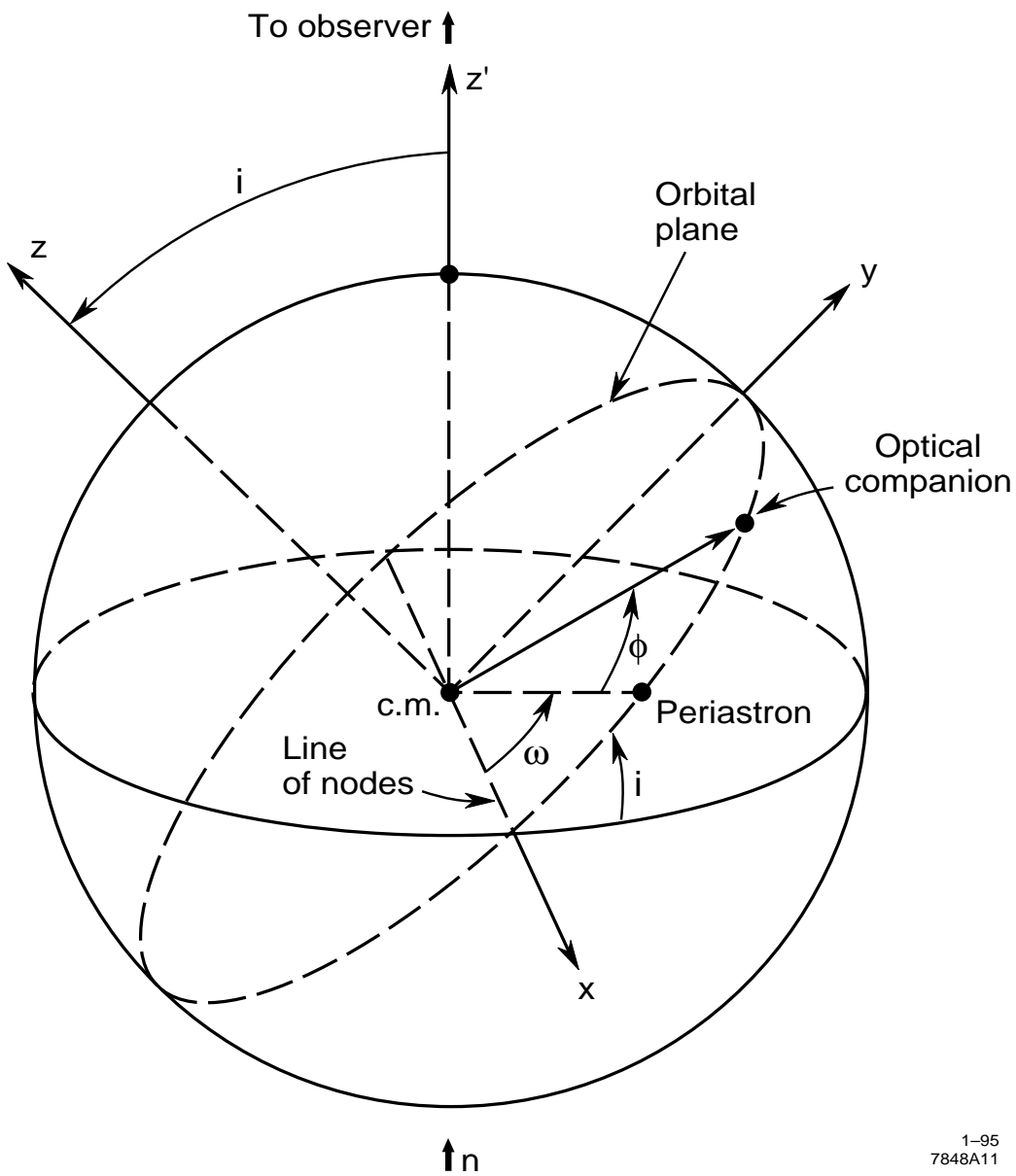


(c)

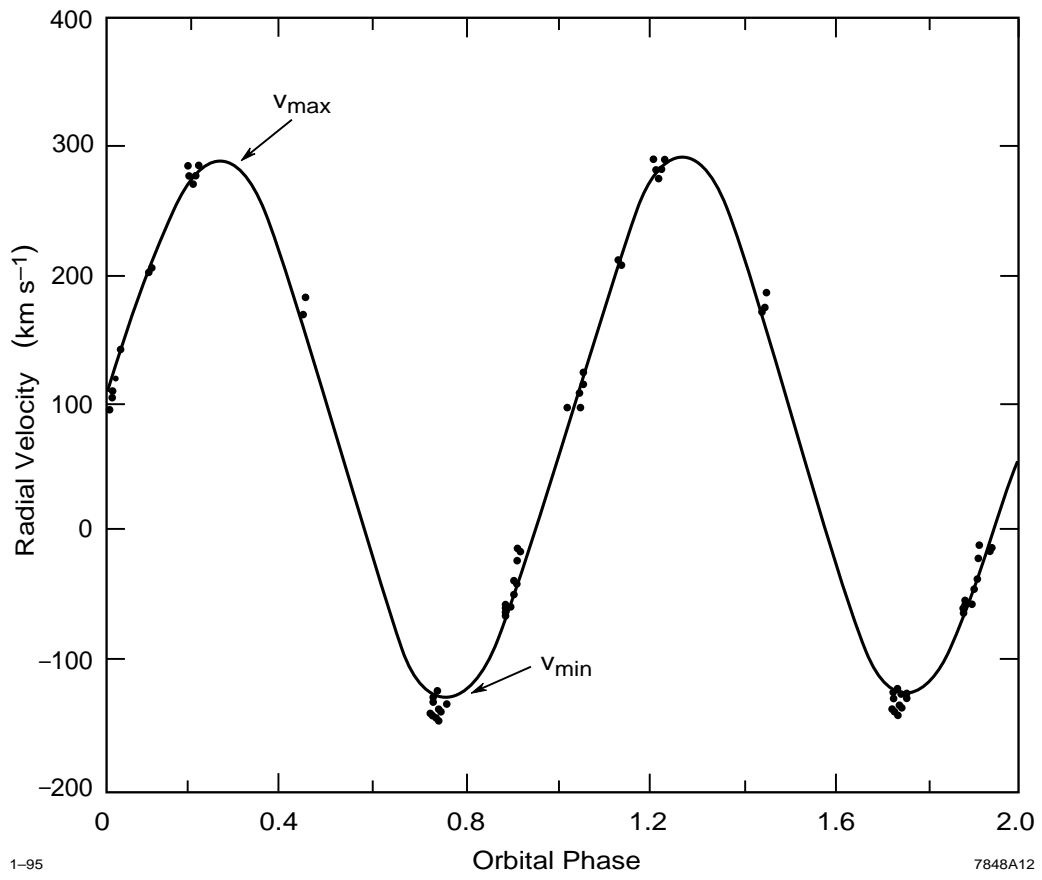




2-96
7848A10

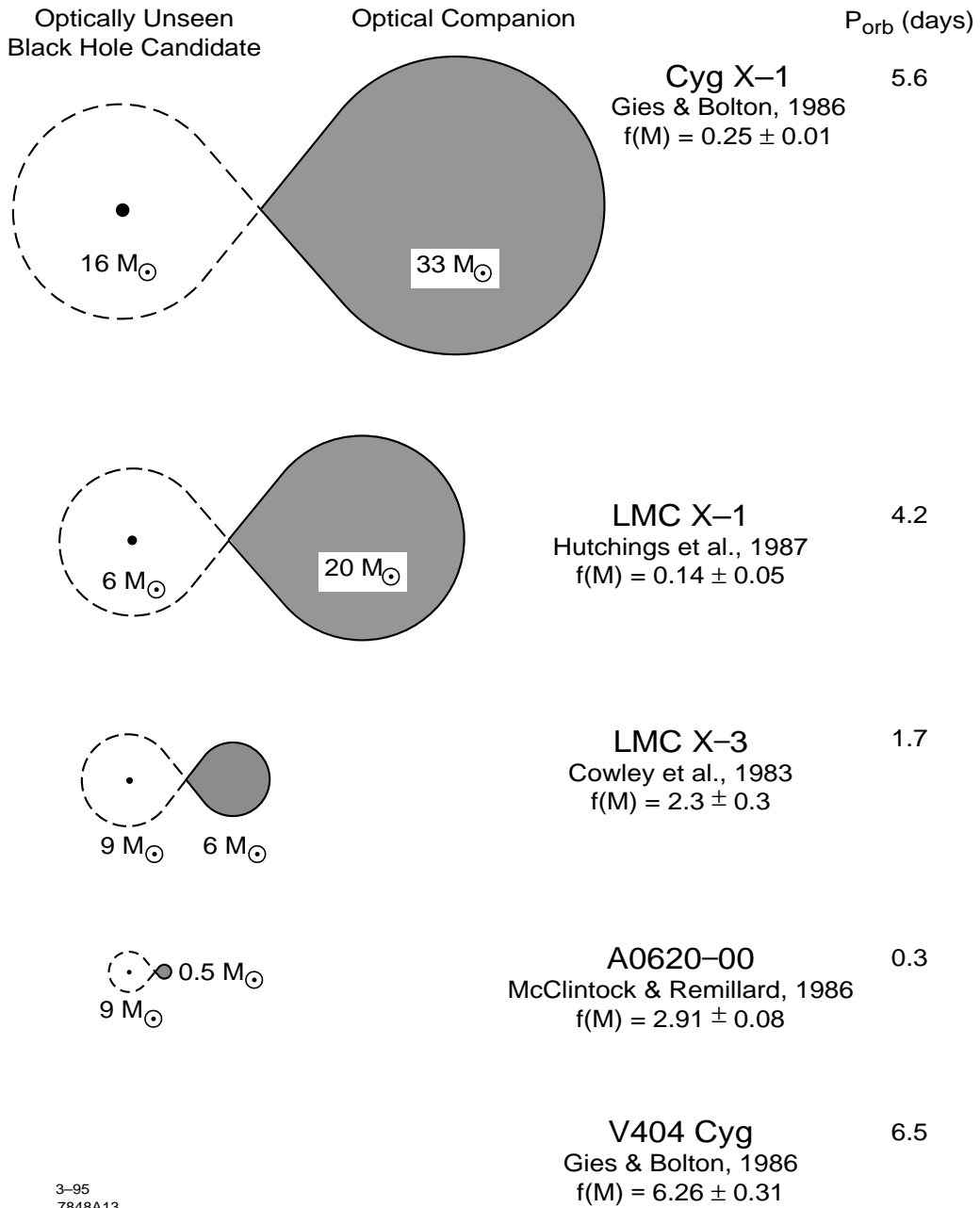


1-95
7848A11

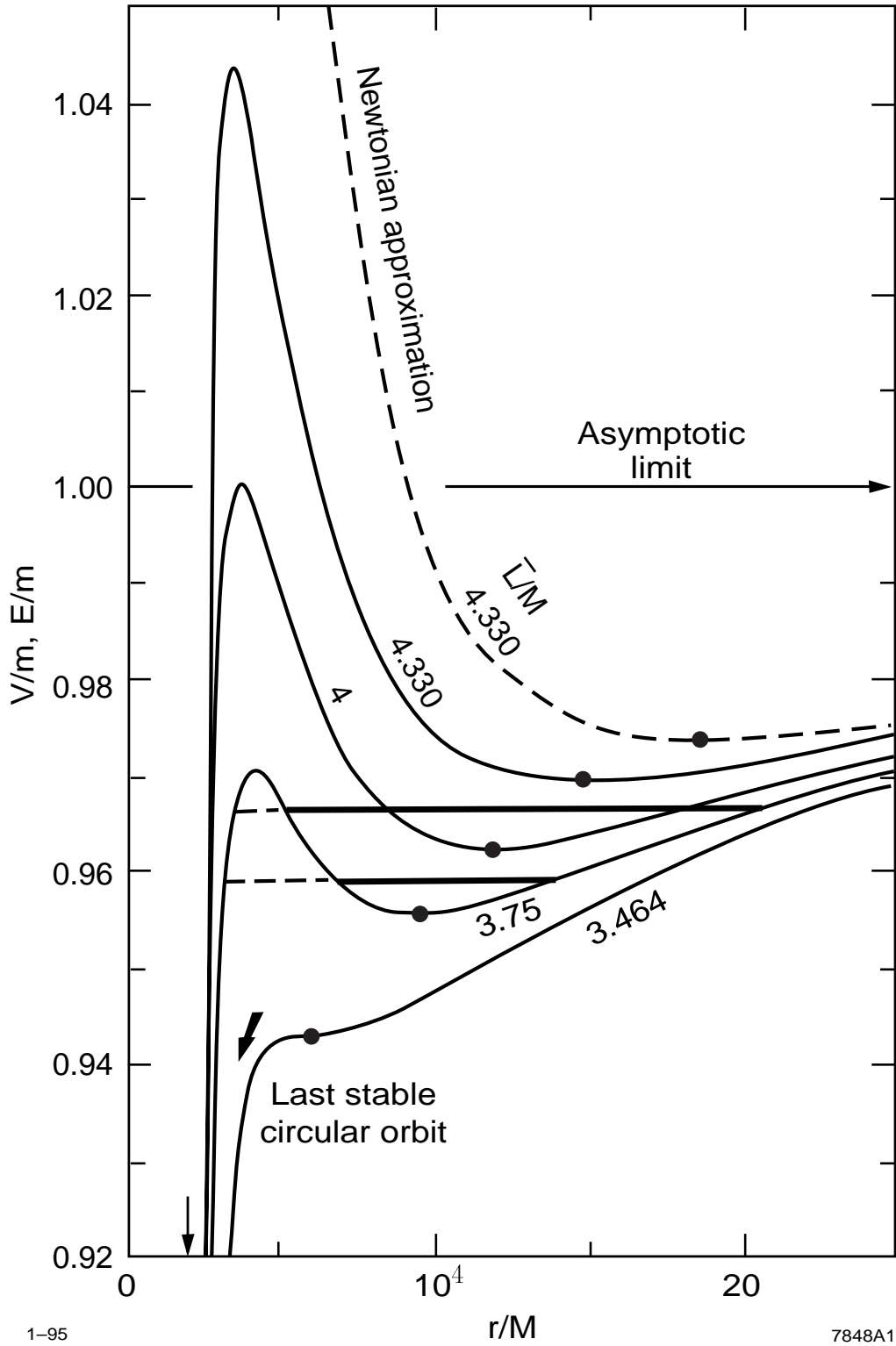


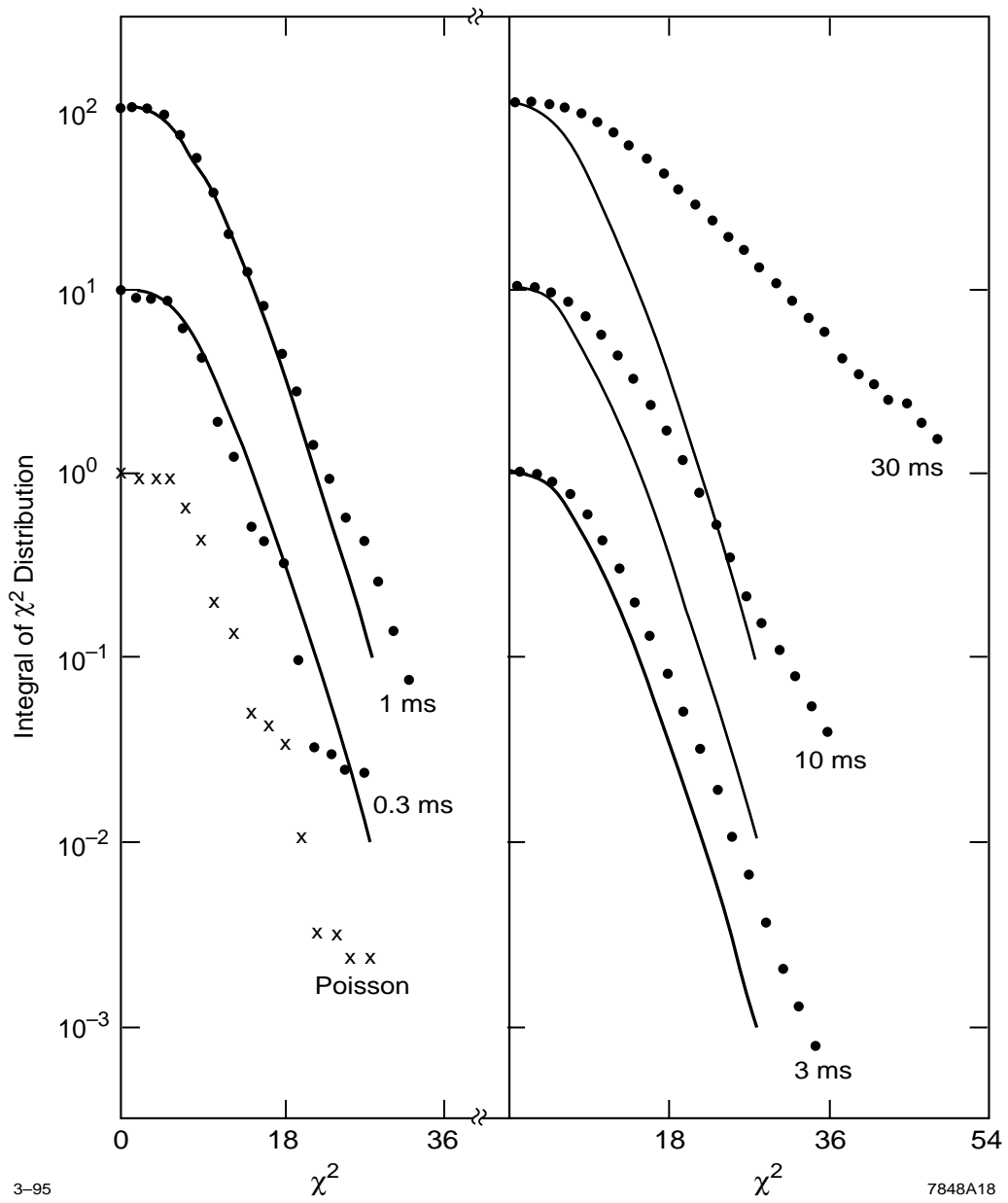
1-95

7848A12



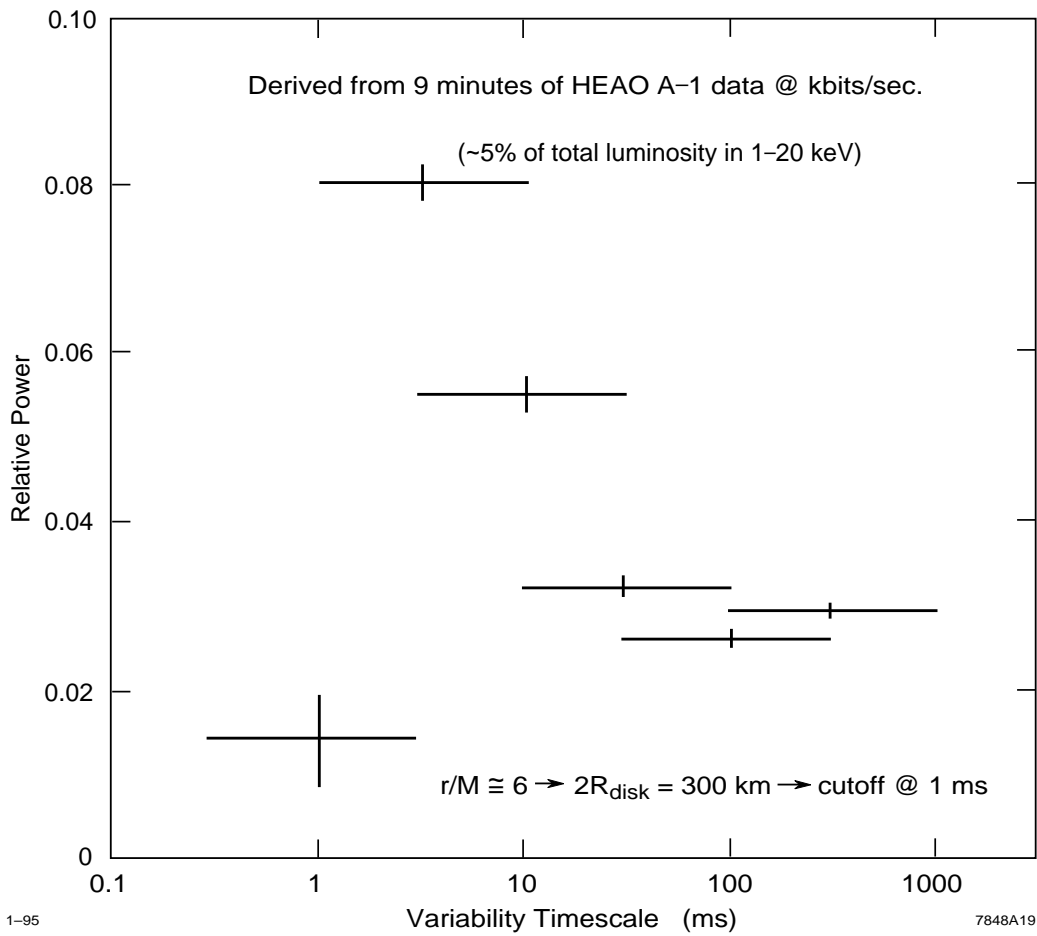
3-95
7848A13



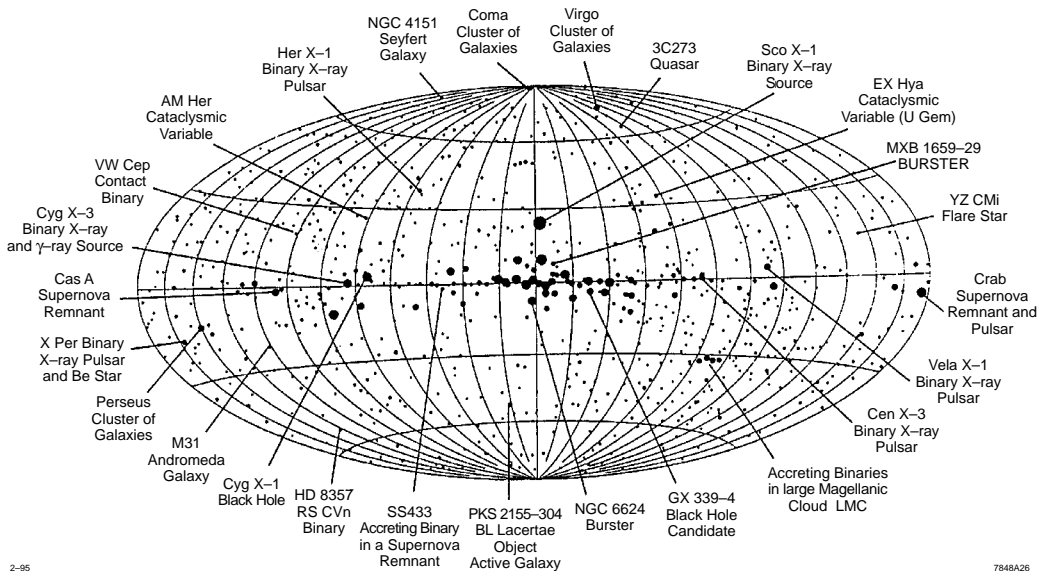


3-95

7848A18

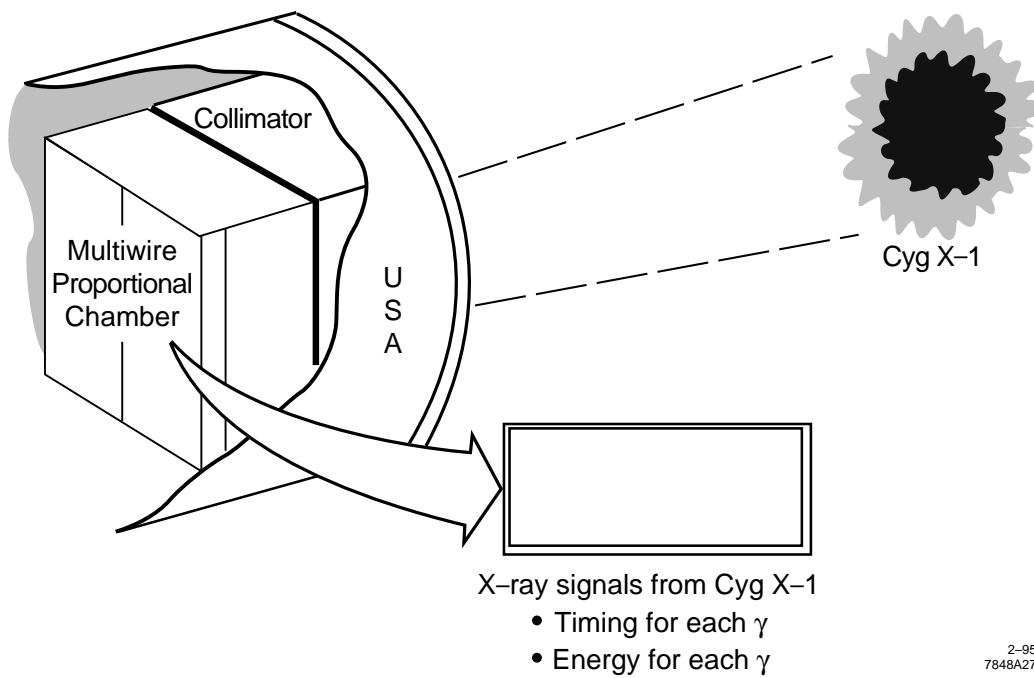


HEAO A-1 X-ray Sky Map

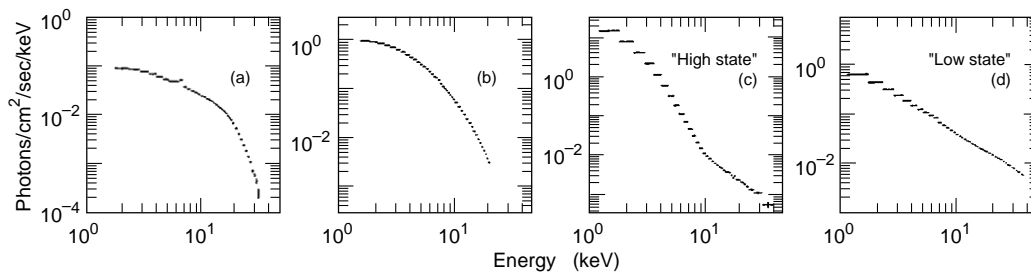


2-95

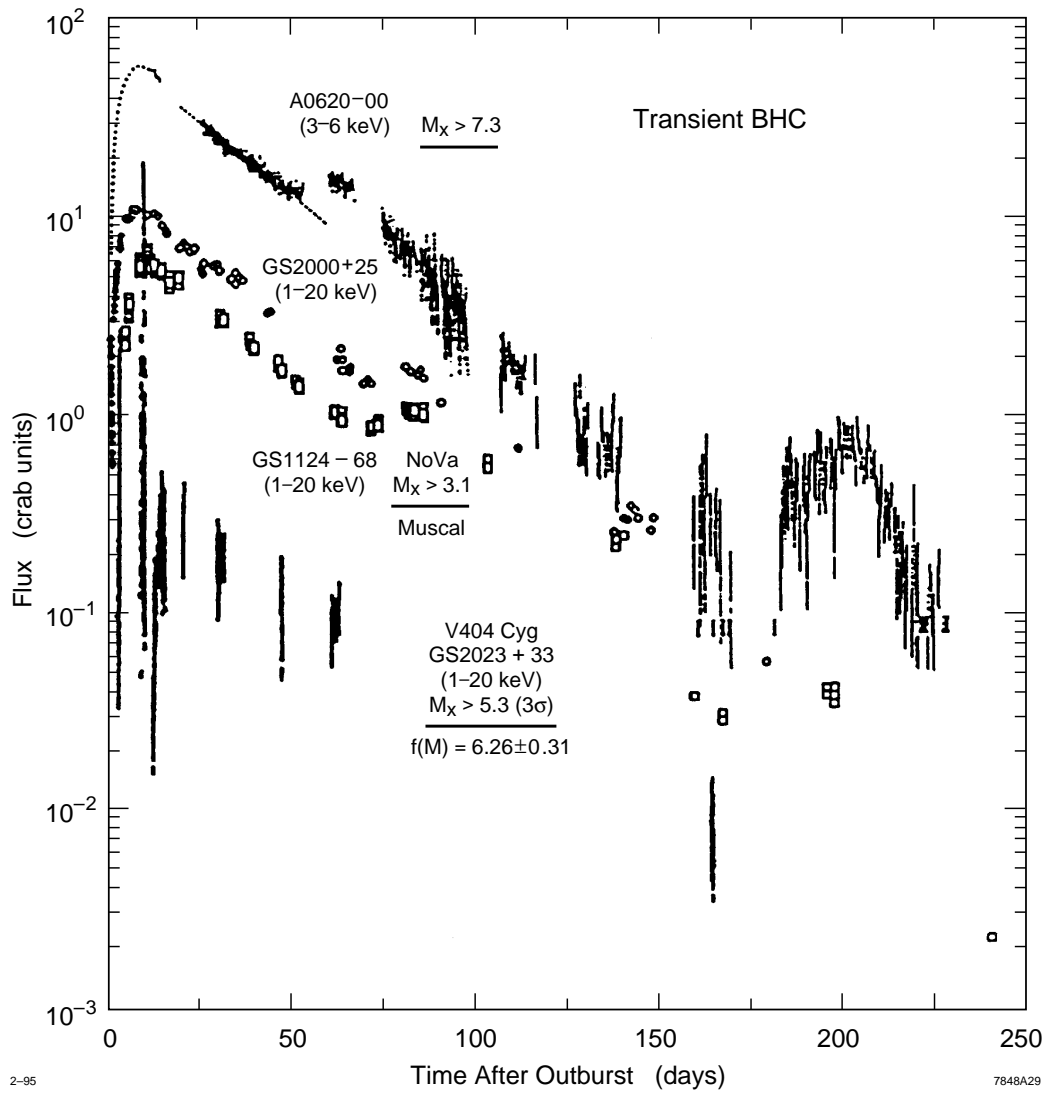
7848A26

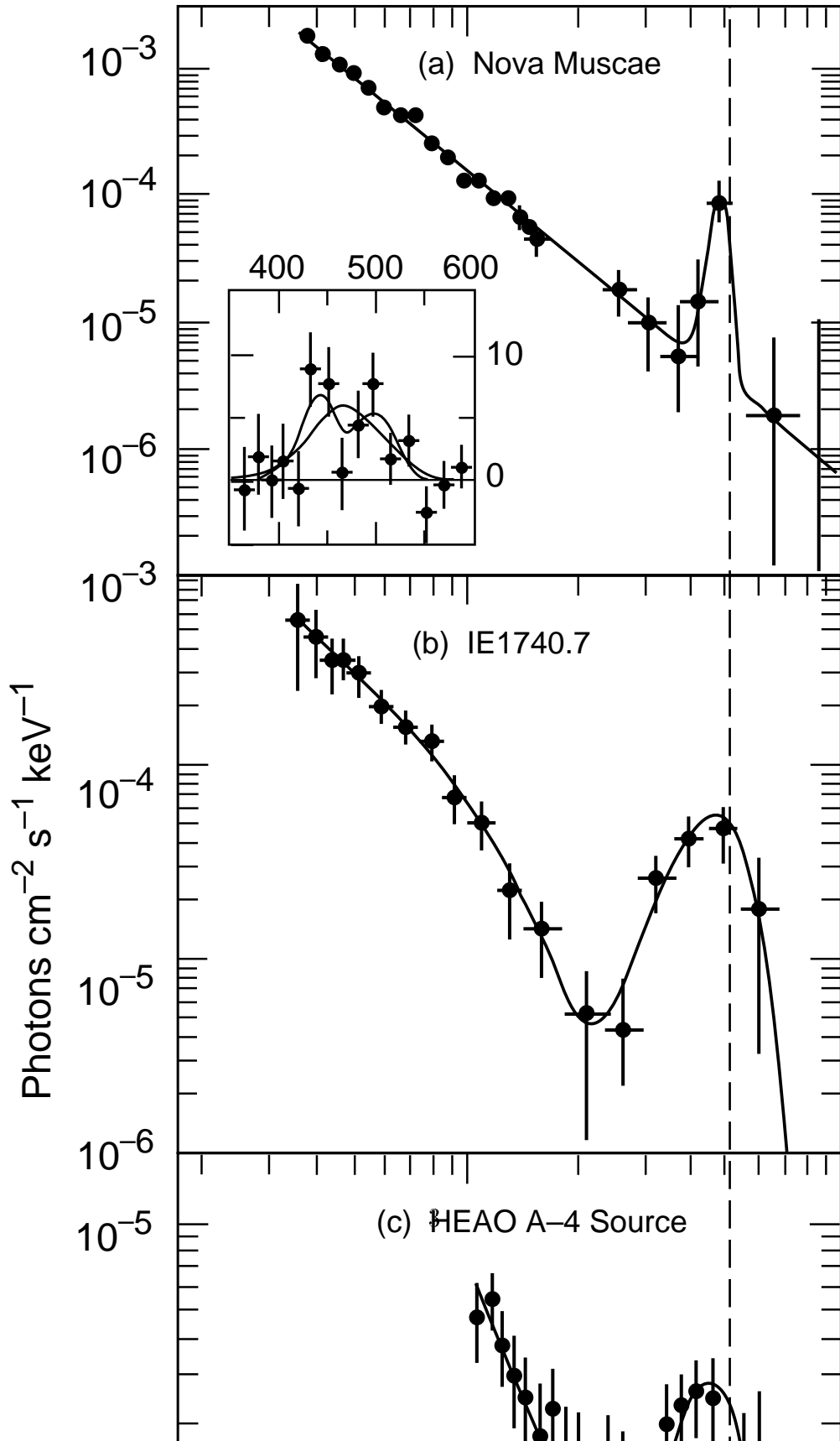


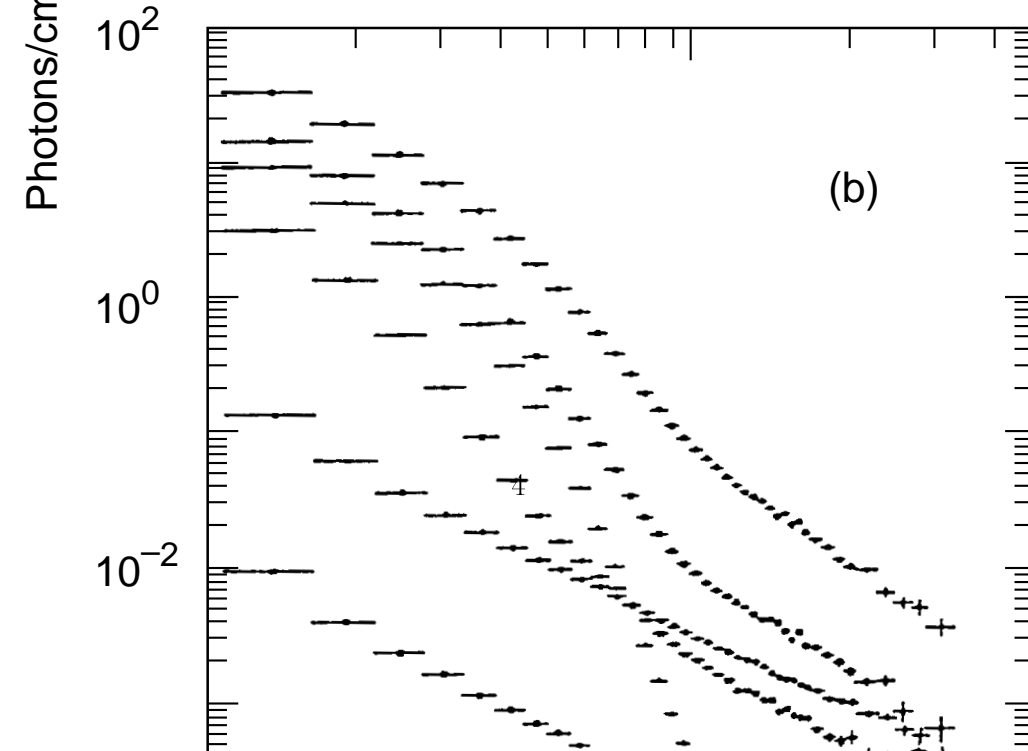
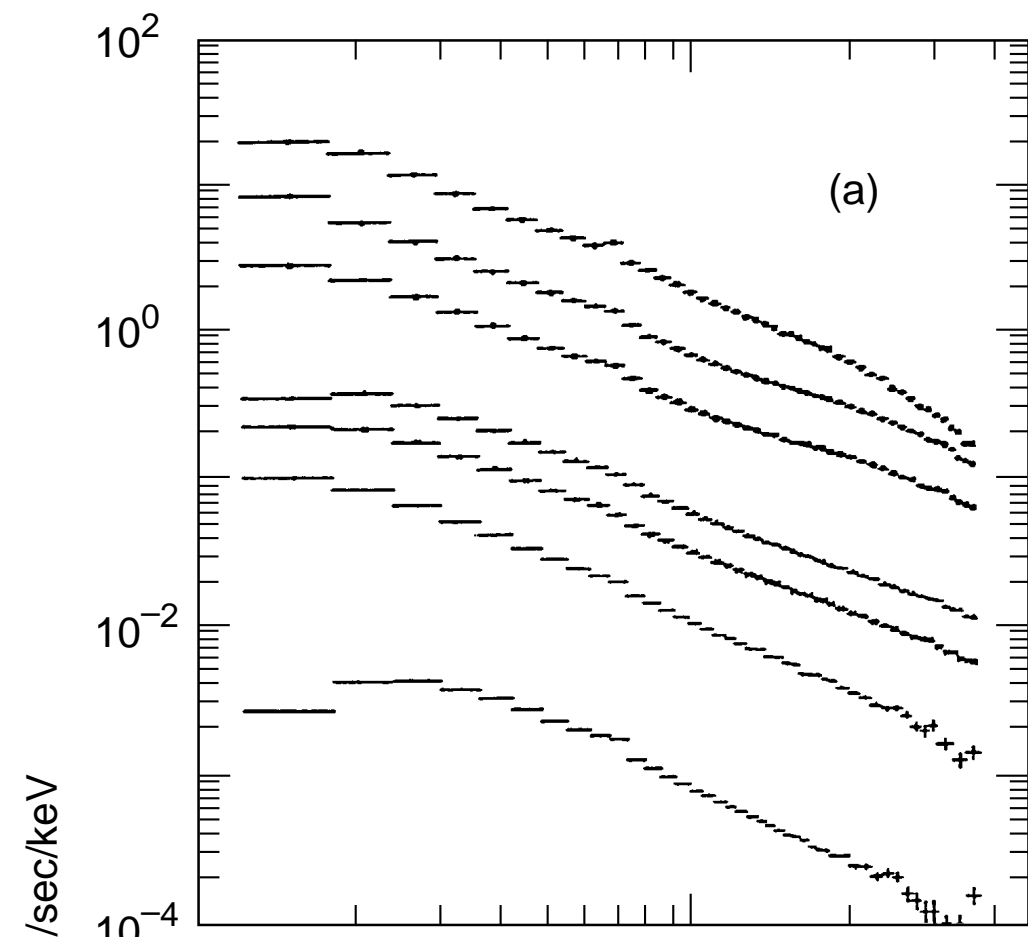
2-95
7848A27

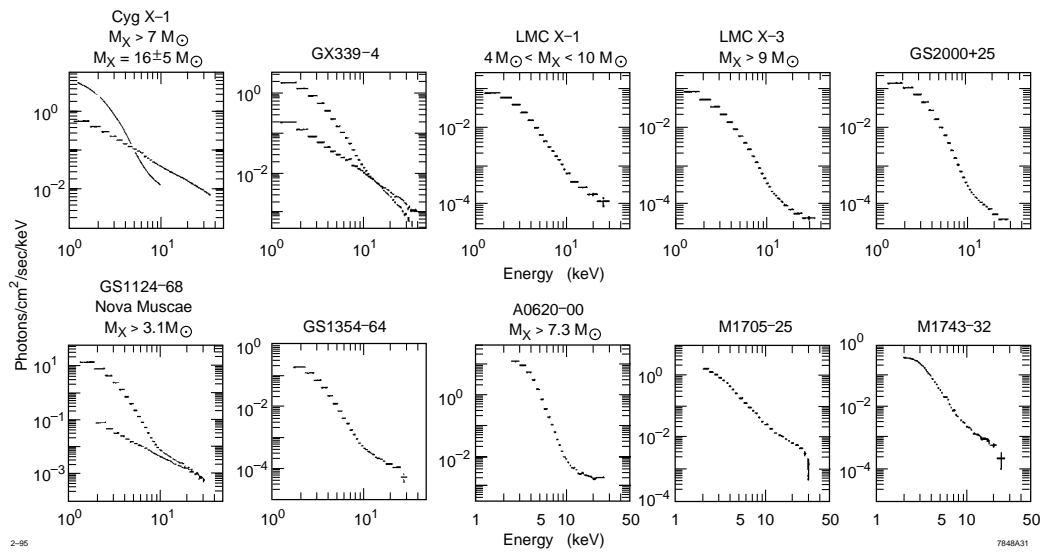


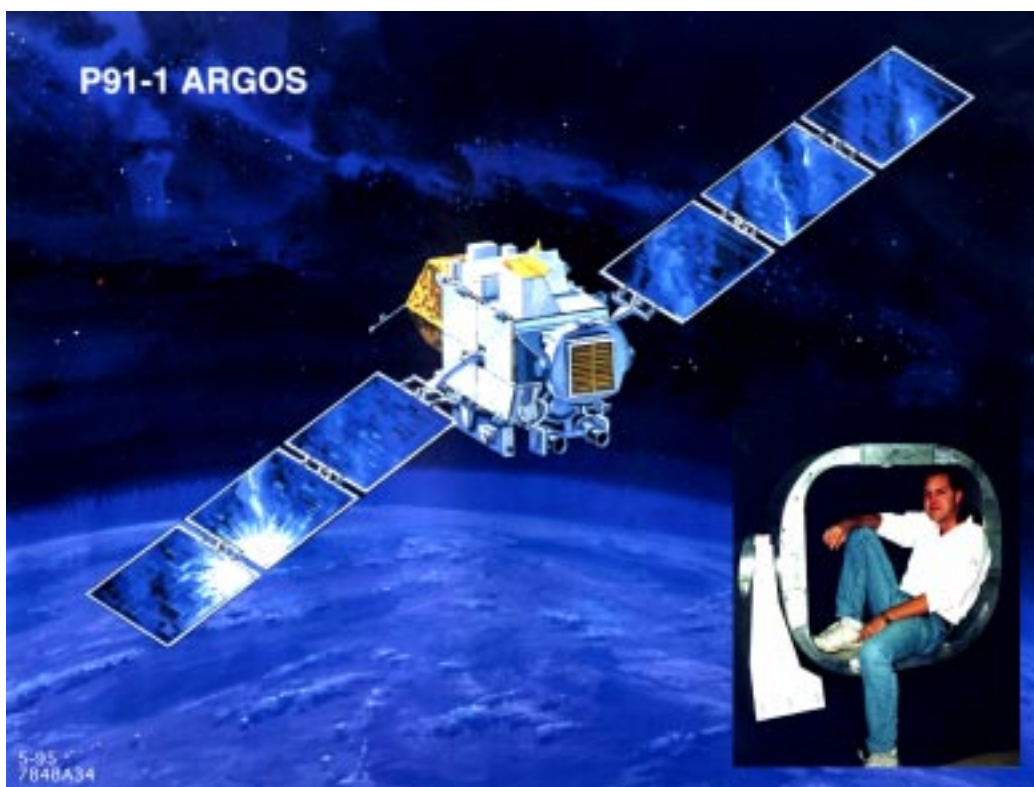
Energy	<ul style="list-style-type: none"> • Power law • Sharp cutoff • Cyclotron lines 	<ul style="list-style-type: none"> • X-ray bursts • Thermal brems. • Spectral shape 	<ul style="list-style-type: none"> • Ultra soft • Hard power law tail 	<ul style="list-style-type: none"> • Single power law
Timing	<ul style="list-style-type: none"> • Regular pulsations (pulsar) 	<ul style="list-style-type: none"> • Aperiodic variability • QPOs • Small amplitude at rapid time scales 	<ul style="list-style-type: none"> • Large time variability of hard power law tail 	<ul style="list-style-type: none"> • Large variability at all time scales <1sec • Considerable amplitude at ms time scales
Result	<ul style="list-style-type: none"> • Compact object is a neutron star, $B \approx 10^8$ T 	<ul style="list-style-type: none"> • Compact object is a neutron star, $B \approx 10^4$ T 	<ul style="list-style-type: none"> • Compact object is a Black hole candidate 	<ul style="list-style-type: none"> • Compact object is a Black hole candidate





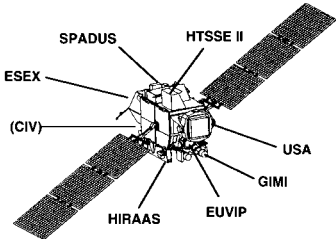
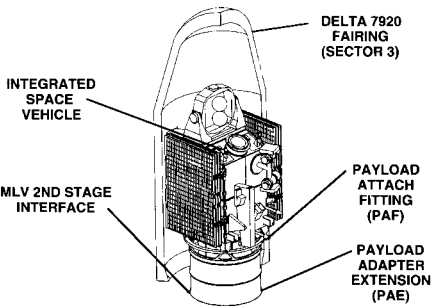


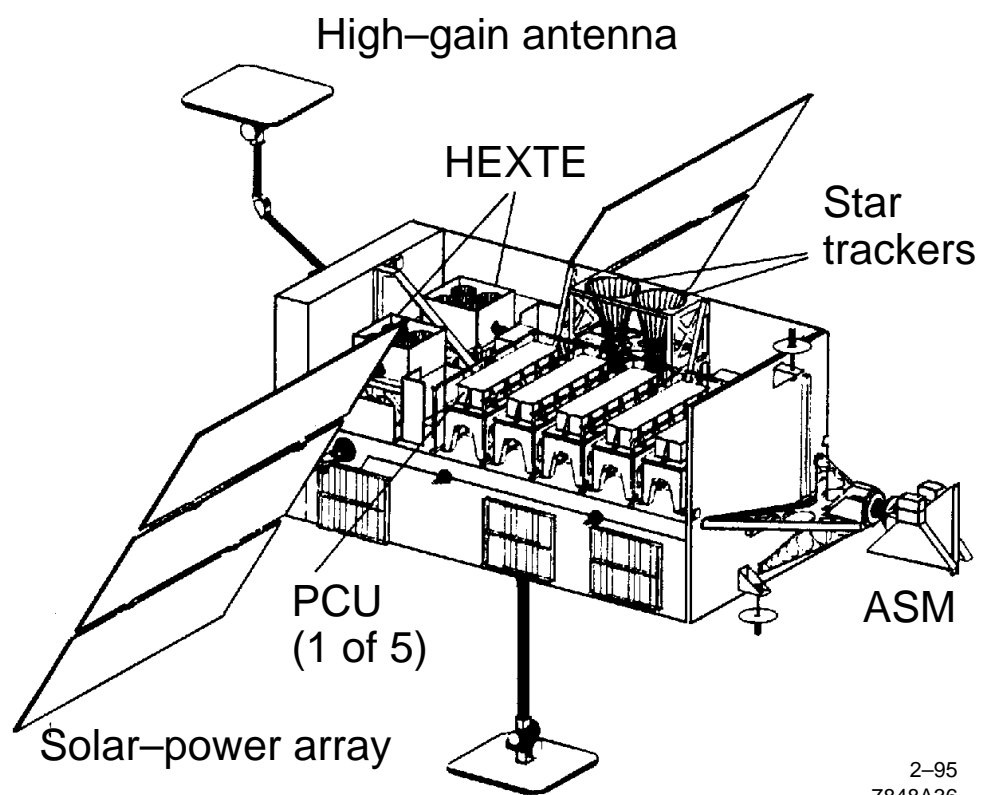




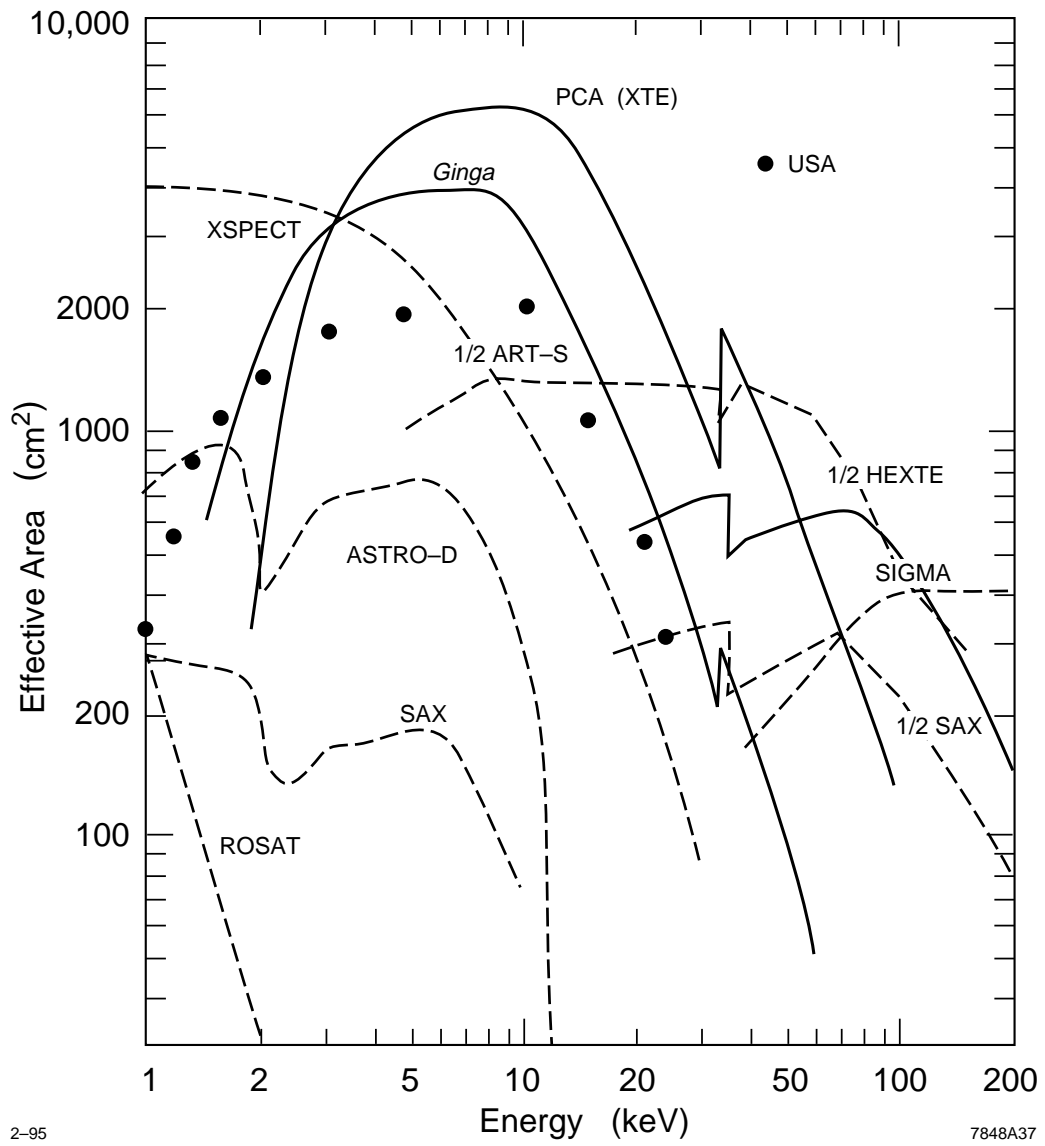
Program Overview

ARGOS

	<p style="text-align: center;">EXPERIMENTS</p> <table border="0"> <tr> <td>1. CIV</td> <td>AFPL</td> <td>Critical Ionization Velocity</td> </tr> <tr> <td>2. ESEX</td> <td>AFPL</td> <td>Arcjet Propulsion Engine</td> </tr> <tr> <td>3. EUVIP</td> <td>ARMY</td> <td>UV Imager</td> </tr> <tr> <td>4. GIMI</td> <td>NRL</td> <td>UV Camera</td> </tr> <tr> <td>5. HIRAAS</td> <td>NRL</td> <td>UV Spectroradiometer</td> </tr> <tr> <td>6. HTSSE II</td> <td>NRL</td> <td>High Temperature Superconductivity Space Experiment</td> </tr> <tr> <td>7. SPADUS</td> <td>ONR</td> <td>Space Dust Experiment</td> </tr> <tr> <td>8. USA</td> <td>NRL</td> <td>Unconv. Stellar (X-Ray)</td> </tr> </table>	1. CIV	AFPL	Critical Ionization Velocity	2. ESEX	AFPL	Arcjet Propulsion Engine	3. EUVIP	ARMY	UV Imager	4. GIMI	NRL	UV Camera	5. HIRAAS	NRL	UV Spectroradiometer	6. HTSSE II	NRL	High Temperature Superconductivity Space Experiment	7. SPADUS	ONR	Space Dust Experiment	8. USA	NRL	Unconv. Stellar (X-Ray)															
1. CIV	AFPL	Critical Ionization Velocity																																						
2. ESEX	AFPL	Arcjet Propulsion Engine																																						
3. EUVIP	ARMY	UV Imager																																						
4. GIMI	NRL	UV Camera																																						
5. HIRAAS	NRL	UV Spectroradiometer																																						
6. HTSSE II	NRL	High Temperature Superconductivity Space Experiment																																						
7. SPADUS	ONR	Space Dust Experiment																																						
8. USA	NRL	Unconv. Stellar (X-Ray)																																						
<p style="text-align: center;">SPACE VEHICLE SYSTEM</p> <table border="0"> <tr> <td>• Mass</td> <td>- Capability</td> <td>6000 lbs</td> </tr> <tr> <td>• Power</td> <td>- Average</td> <td>1000 W</td> </tr> <tr> <td>• Orbit</td> <td>- Altitude</td> <td>450 n.mi.</td> </tr> <tr> <td></td> <td>- Inclination</td> <td>98.7°</td> </tr> <tr> <td>• Launch Vehicle</td> <td>- MLV Class</td> <td>Delta II</td> </tr> <tr> <td>• Downlink Rate</td> <td>- Carrier I</td> <td>4 K or 128 Kbps</td> </tr> <tr> <td></td> <td>- Carrier II</td> <td>1, 4, or 5 Mbps</td> </tr> <tr> <td>• Uplink</td> <td></td> <td>2000 bps</td> </tr> <tr> <td>• Data storage</td> <td></td> <td>2.4 Gbits</td> </tr> <tr> <td>• Mission Life</td> <td></td> <td>3 years</td> </tr> <tr> <td>• Reliability</td> <td></td> <td>0.9 for 1 year</td> </tr> <tr> <td>• Altitude Pointing</td> <td>- Control</td> <td>0.3°</td> </tr> <tr> <td></td> <td>- Knowledge</td> <td>0.1°</td> </tr> </table>	• Mass	- Capability	6000 lbs	• Power	- Average	1000 W	• Orbit	- Altitude	450 n.mi.		- Inclination	98.7°	• Launch Vehicle	- MLV Class	Delta II	• Downlink Rate	- Carrier I	4 K or 128 Kbps		- Carrier II	1, 4, or 5 Mbps	• Uplink		2000 bps	• Data storage		2.4 Gbits	• Mission Life		3 years	• Reliability		0.9 for 1 year	• Altitude Pointing	- Control	0.3°		- Knowledge	0.1°	
• Mass	- Capability	6000 lbs																																						
• Power	- Average	1000 W																																						
• Orbit	- Altitude	450 n.mi.																																						
	- Inclination	98.7°																																						
• Launch Vehicle	- MLV Class	Delta II																																						
• Downlink Rate	- Carrier I	4 K or 128 Kbps																																						
	- Carrier II	1, 4, or 5 Mbps																																						
• Uplink		2000 bps																																						
• Data storage		2.4 Gbits																																						
• Mission Life		3 years																																						
• Reliability		0.9 for 1 year																																						
• Altitude Pointing	- Control	0.3°																																						
	- Knowledge	0.1°																																						

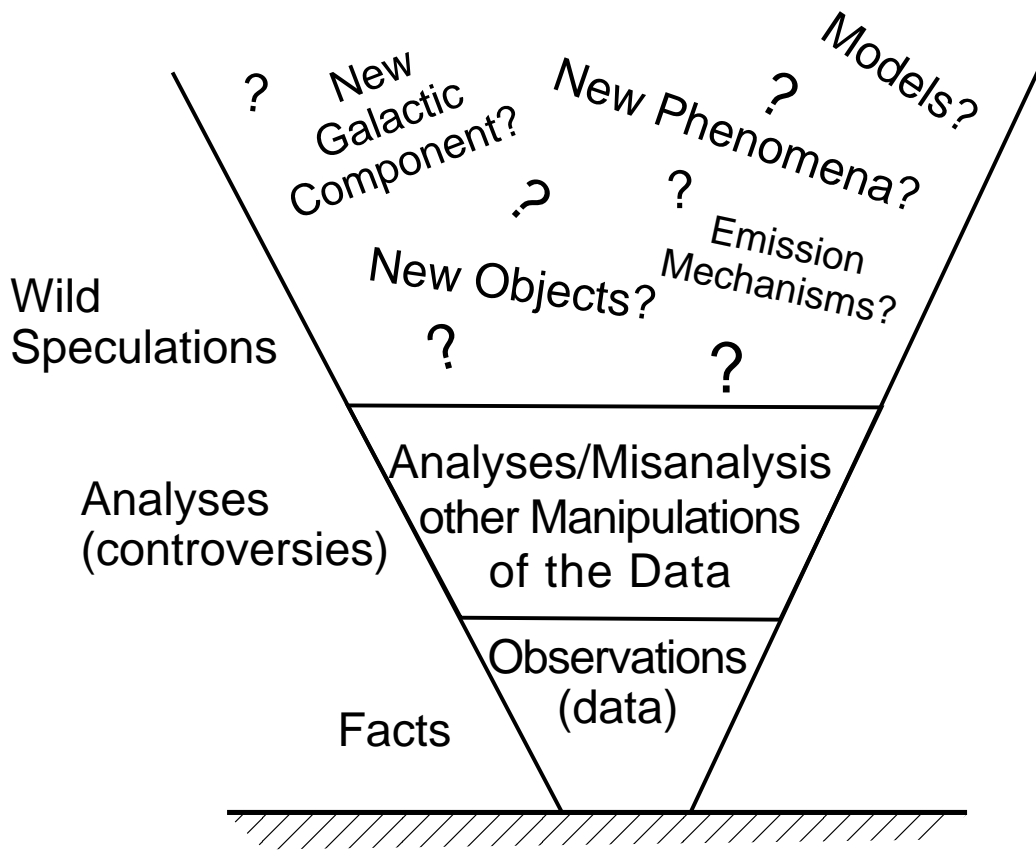


2-95
7848A36



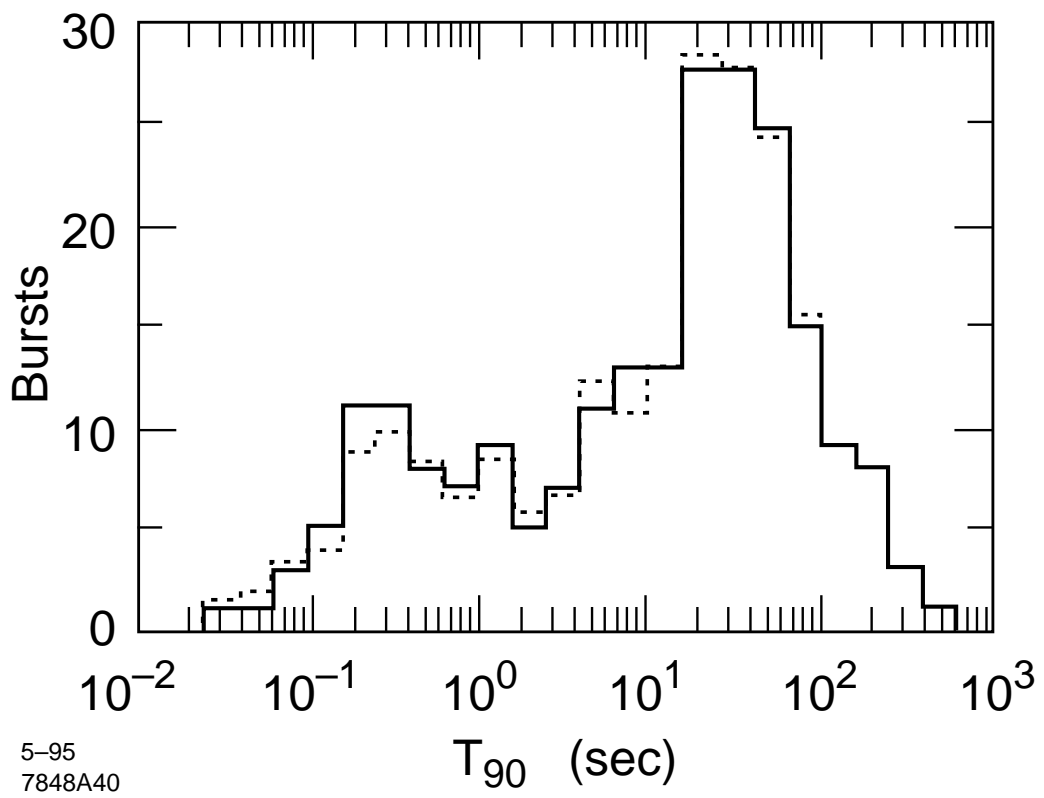
2-95

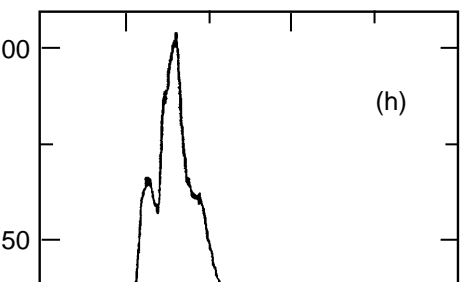
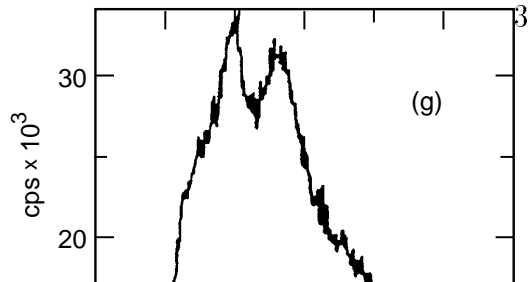
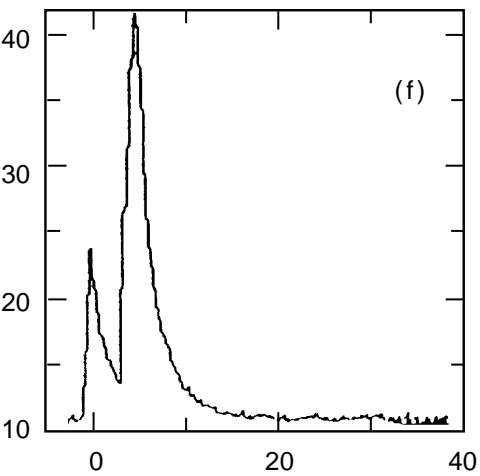
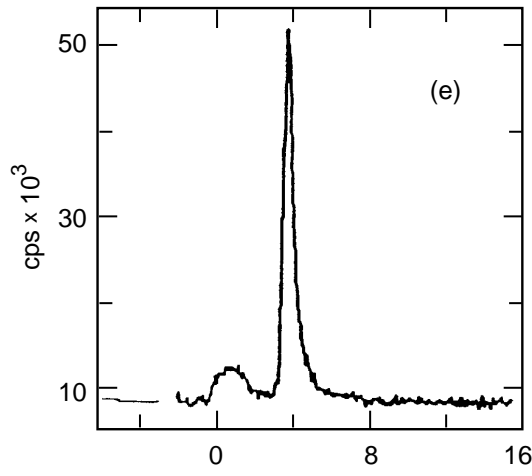
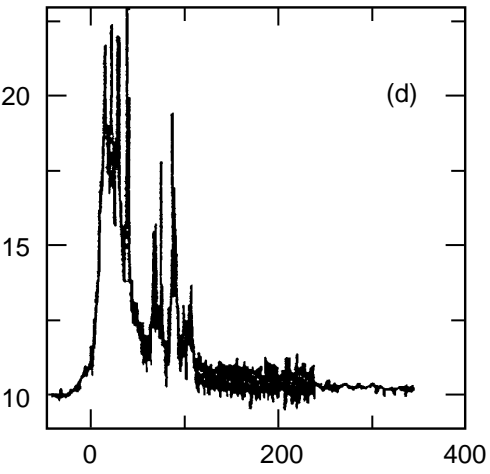
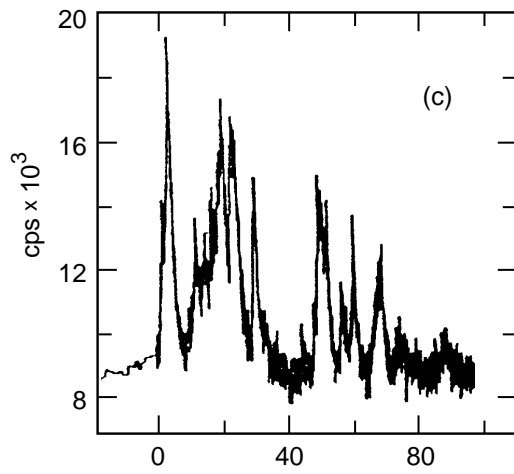
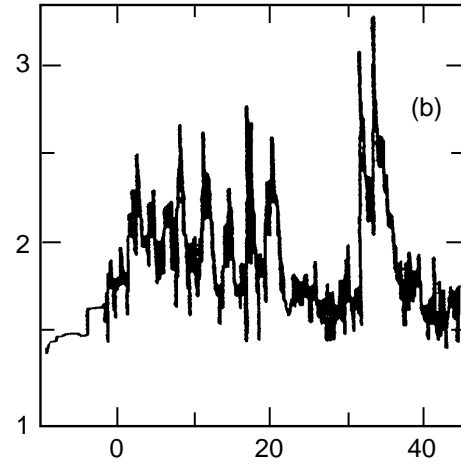
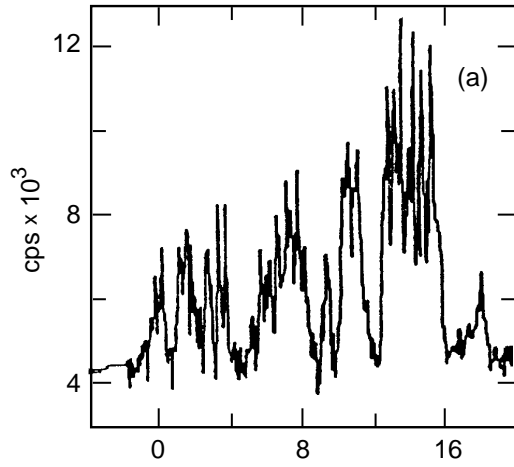
7848A37

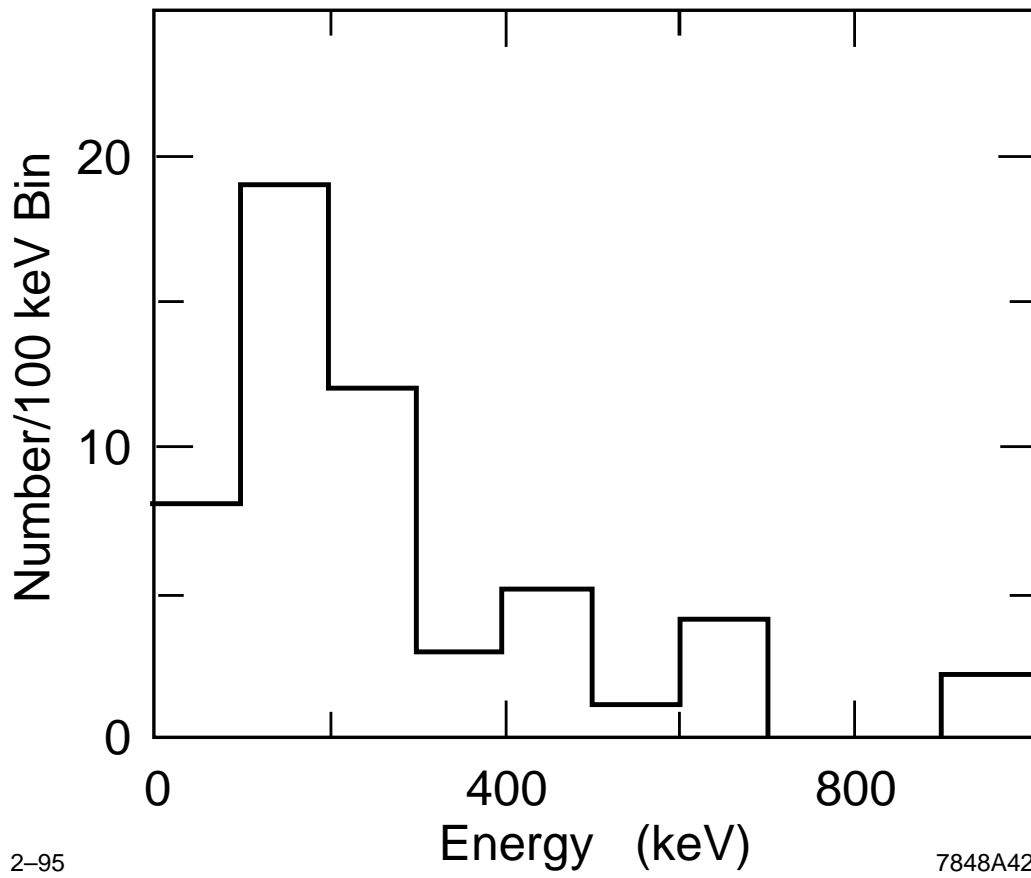


2-95
7848A38

Gamma Ray Bursts

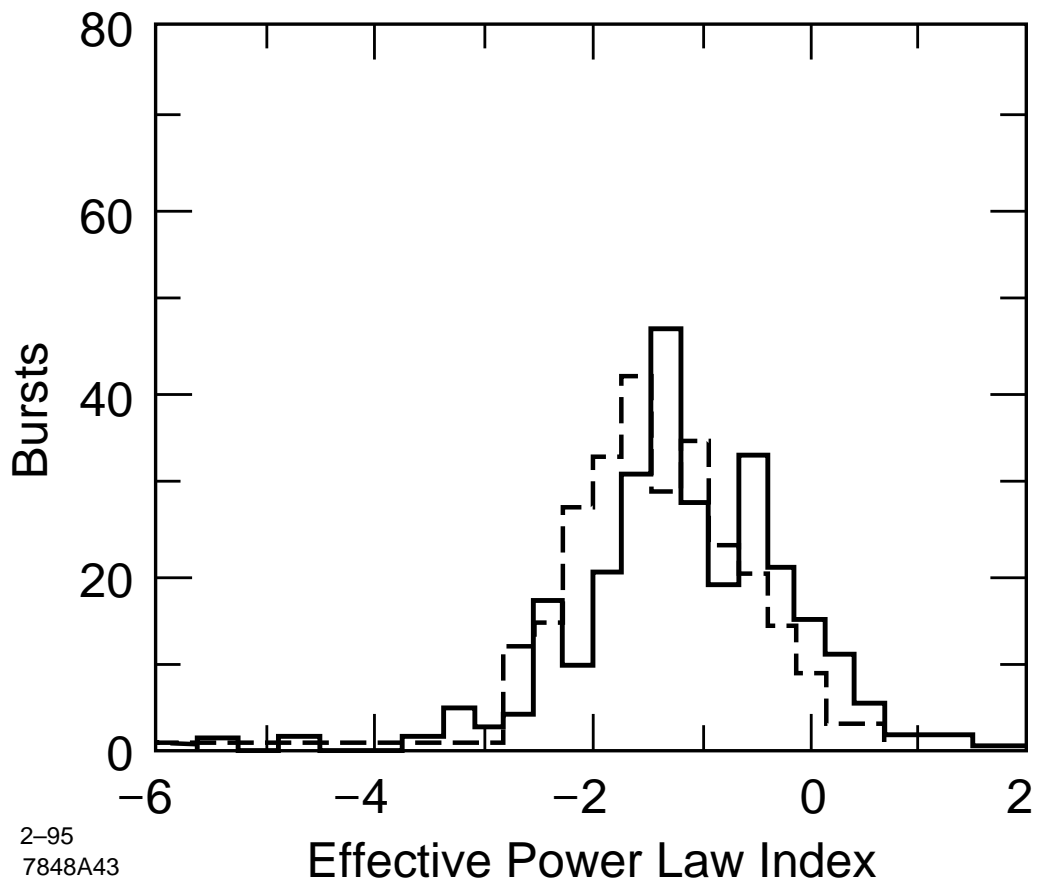


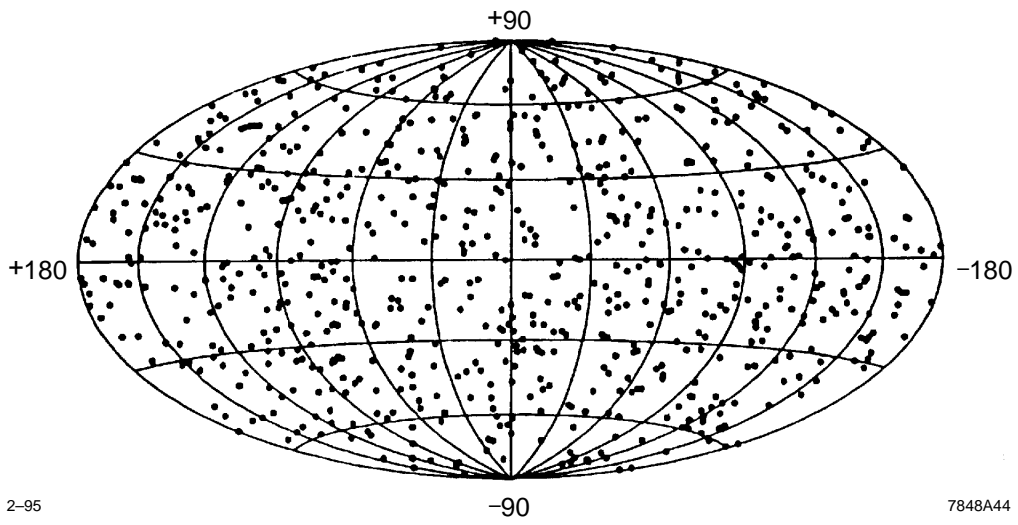


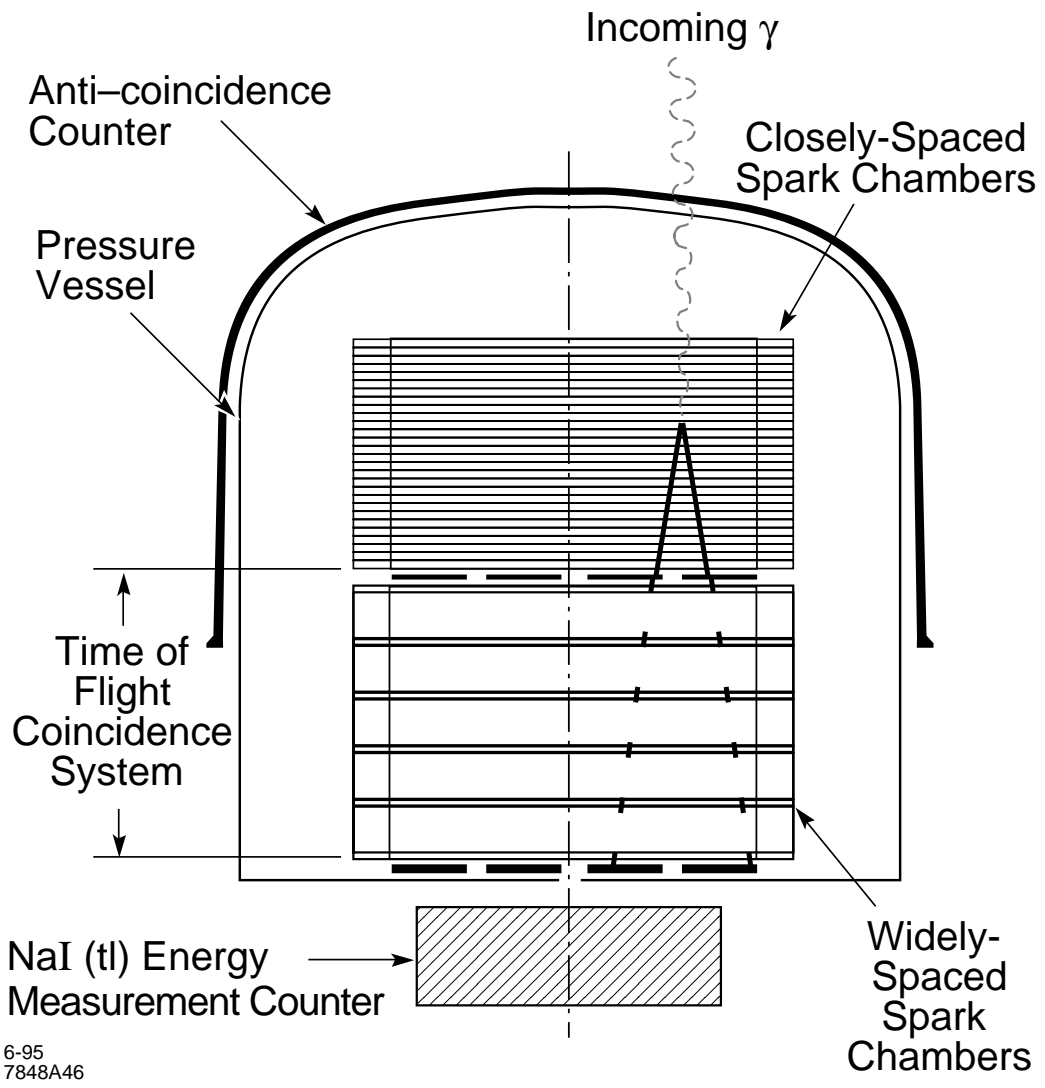


2-95

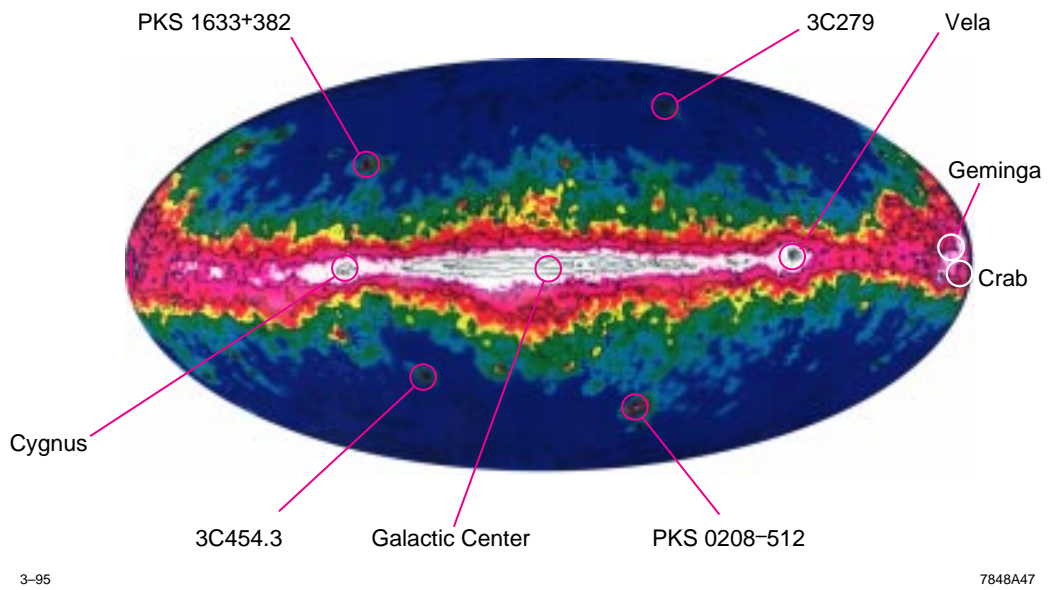
7848A42

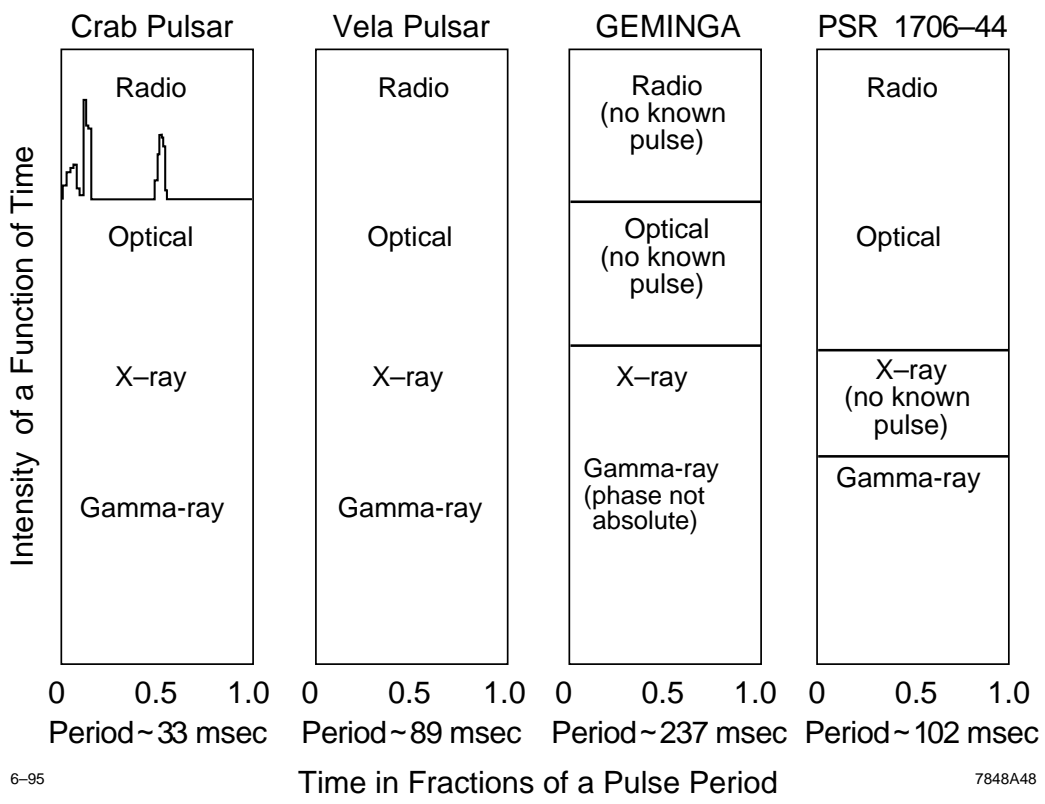




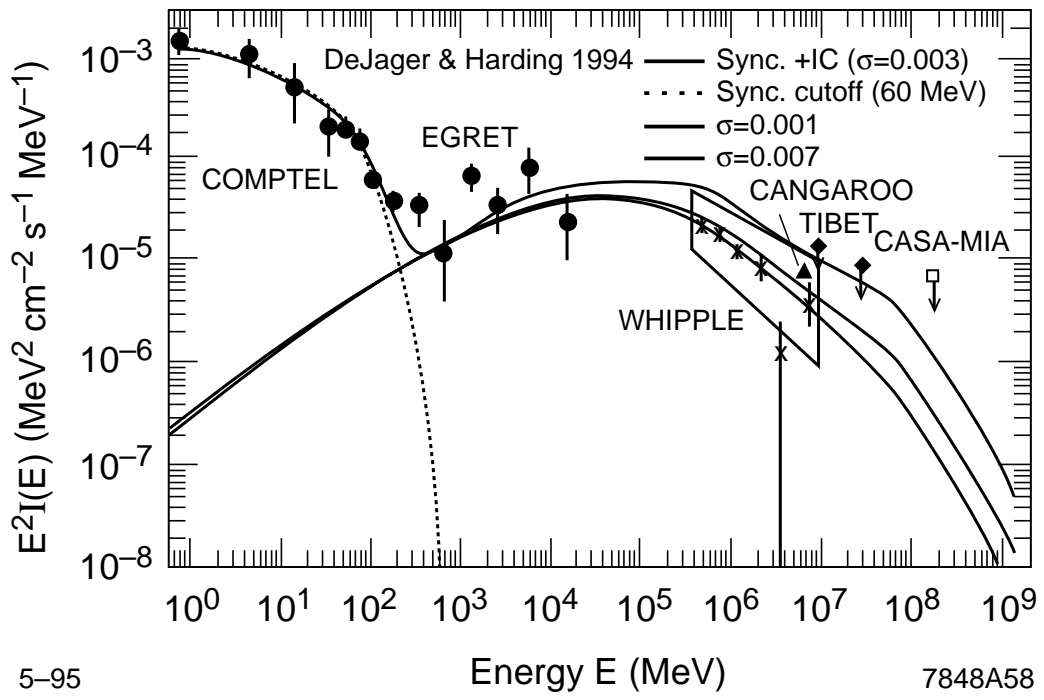


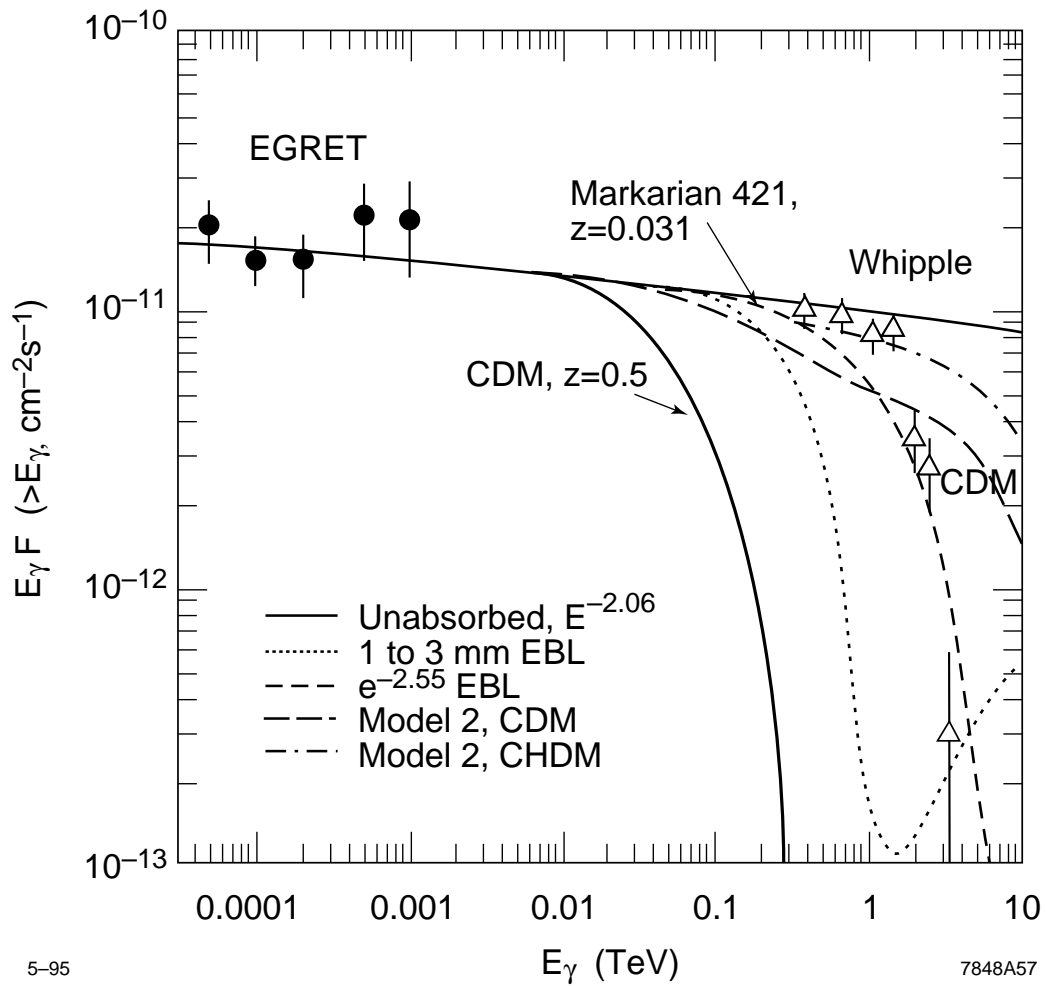
6-95
7848A46



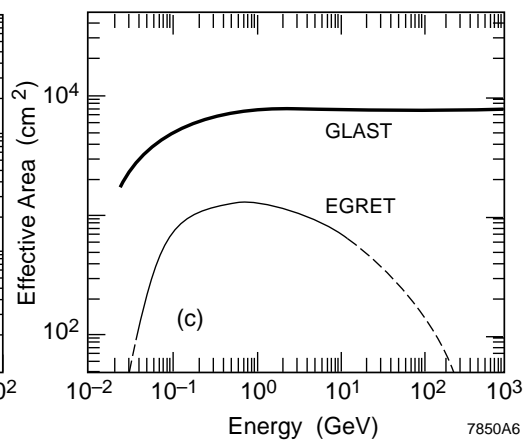
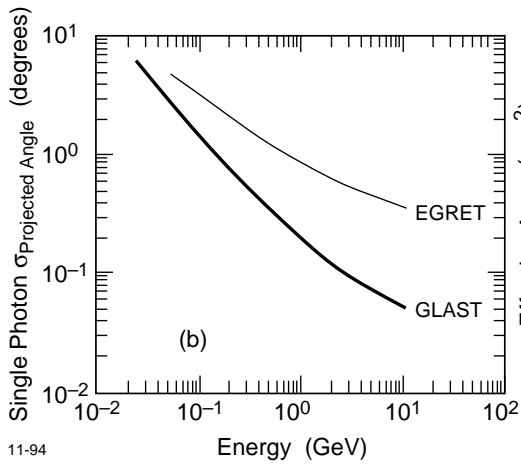
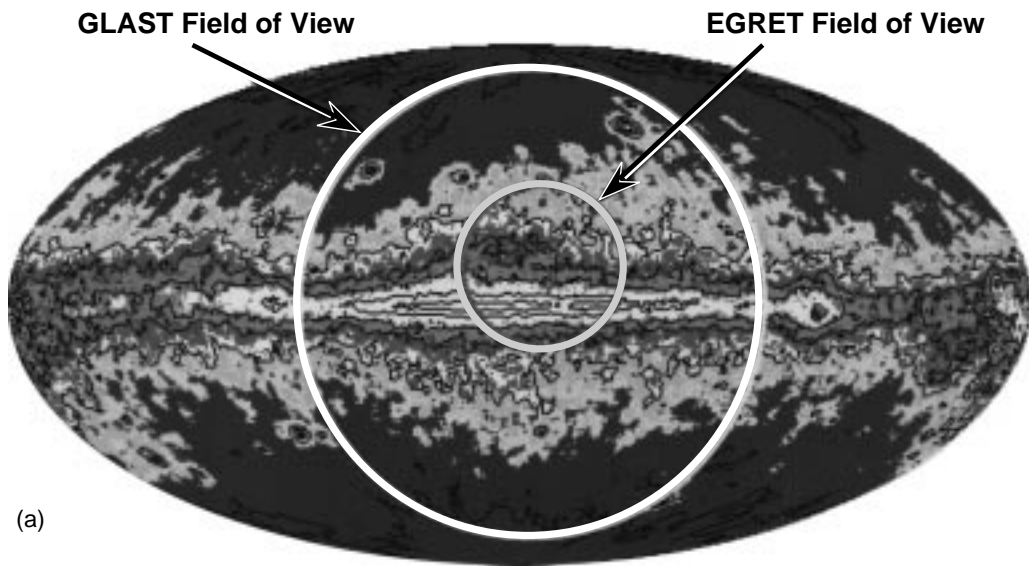


CRAB NEBULA



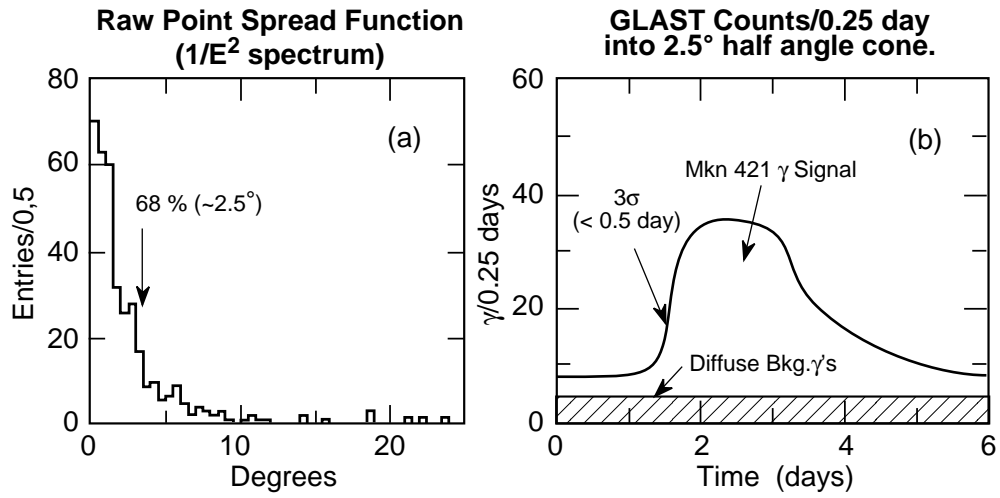


EGRET All-Sky Map

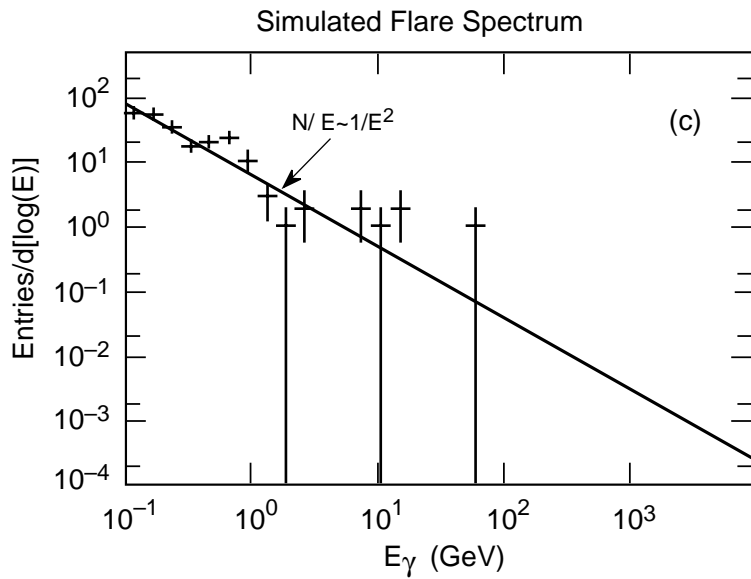


11-94

7850A6



The energy and acceptance corrected Mkn 421 Flare Spectrum





7848A53

2-95

